1

Thermodynamics of Homogeneous and Heterogeneous Semiconductor Systems

1.1 Introduction

Elemental and compound semiconductors represent a vast family of materials of strategic interest for a variety of mature and advanced applications in micro- and opto-electronics, solid state lighting (SSL), solid state physical and chemical sensors, high efficiency solar cells and nanodevices. The materials themselves have always been technology enablers and their role today is even more significant in view of the increasing demand for sustainable development applications and high temperature, high pressure technologies.

The semiconductors family includes elemental solids such as silicon, the material of choice for the microelectronic and photovoltaic industry, binary alloys such as the Si-Ge alloys used for their elevated carrier mobilities, and compound semiconductors, of which SiC is used for high power, high frequency devices and phosphides, arsenides and nitrides for the most advanced optoelectronic applications.

Their preparation under defined limits of stoichiometry (in the case of compounds) and purity requires a deep knowledge of the chemistry and physics of liquid-, solid-, vapour- and plasma-growth and post-growth processes.

Semiconductors, like other inorganic and organic solids, may be stable in different structural configurations, depending on the composition, temperature, hydrostatic pressure and strain. Their chemical, physical and mechanical properties under different environmental conditions (temperature, pressure, strain) depend on their elemental composition, stoichiometry, impurity contamination, and also on their point- and extended-defects content. In fact, although solids are a typical class of materials characterized by microscopic order, most of their electronic and optoelectronic properties depend on or are influenced by impurities and point and extended defects.

Physical Chemistry of Semiconductor Materials and Processes, First Edition. Sergio Pizzini.

Knowledge of their macroscopic features, such as their structural, thermodynamic, chemical, electrical and mechanical properties over a broad range of temperatures and pressures, is critical for their practical use. These properties, when not already available, should be experimentally or computationally determined.

This objective, addressed at metals, metal alloys and non-metallic solids, has been in the last few decades the traditional goal of physical metallurgy and physical chemistry. It is also the subject of several excellent textbooks and monographs [1–4], where emphasis is mainly given to structure–property relationships, solution- and defect-theories and nonstoichiometry of non-metallic solids [5], devoting, until very recently [6], only limited attention to elemental and compound semiconductors.

The aim of this chapter, and of the entire book, is to fill this gap and present in the most concise and critical manner possible the application of thermodynamics and physical chemistry to elemental and compound semiconductors, assuming knowledge of the fundamental laws of thermodynamics [7] and the basic principles of solid state and semiconductor physics [8, 9].

The intent is also to show that physical chemistry applied to semiconductors has been, and still is, of unique value for the practical and theoretical understanding of their environmental compliance and for the optimization of their growth and post-growth processes, all having a strong impact on the final properties of the material.

As impurities have a significant role in the optical and electronic properties of semiconductors, their thermodynamic behaviour will be considered in terms of their solubility and distribution among neighbouring phases as well as in terms of formation of complex species with other impurities and point defects.

For elemental semiconductors the main interest will be devoted to Group IV and VI elements (carbon, germanium, silicon, selenium and tellurium), the first of which being characterized by a number of stable phases, some of these of extreme scientific and technological interest, as is the case for diamond and graphene. For compound semiconductors we will consider the II–VI and the III–V compounds, such as the arsenides, phosphides, selenides, sulfides, tellurides and nitrides, all of which are of crucial interest for optoelectronic applications, SSL and radiation detection.

The most up to date physical and structural data of the different systems will be used: the reader interested in thermodynamic databases and phase diagram computation is referred to the Scientific Group Thermodata Europe (SGTE) Solution database, NSM Archive, www.ioffe.rssi.ru/SVA/NSM/Semicond/ and to Gibbs [10].

1.2 Basic Principles

A semiconductor is a *thermodynamic system* for which one has to define the equilibrium state and the nature of the transformations which occur when it is subjected to external thermal, mechanical, chemical, magnetic or electromagnetic forces during its preparation and further processing.

This system may consist of a homogeneous elemental or multicomponent *phase* or a heterogeneous mixture of several phases, depending on the temperature, pressure and composition.

A phase is conventionally defined as a portion of matter, having the property of being chemically and physically homogeneous at the microscopic level and of being confined within a surface which embeds it entirely.

The surface itself may be an external surface if it separates a phase from vacuum or from a gaseous environment. It is an internal surface, or an interface, when it separates a phase from another identical or different phase. According to Gibbs, the surface itself may be considered a phase of reduced (2D) dimensionality.

When one is concerned with microscopic or nanoscopic phases, such as nanodots, nanowires and nanotubes, the surface area to volume ratio, A_s/V increases considerably, as does the ratio R of the number of atoms at the surface to those in the bulk (see Table 1.1), with reduction in size of the crystallite phase. This has a significant impact on the physical and chemical properties of the phase itself and of its surface, enhancing in particular its chemical reactivity, but also other properties of relevant importance in semiconductor physics, such as the distribution and electrical activity of dopant impurities.

A phase may be gaseous, liquid or solid. In extreme conditions it could be stable in a plasma configuration, consisting of a mixture of electrons and ionized atoms/molecules. A phase is *condensed* when its aggregation state is that of a liquid or a solid material.

The thermodynamic state of a system is defined by specifying the minimum set of measurable properties needed for all the remaining properties to be fully determined. Properties which do not depend on mass (e.g. P, T) are called intensive. Those depending on mass (i.e. on composition) are called extensive.

A critical thermodynamic state of a system is its equilibrium state. It represents the condition where the system sits in a state of minimum energy and there are no spontaneous changes in any of its properties.

For a system consisting of a single, homogeneous multicomponent phase it is possible to define its thermodynamic state using thermodynamic functions (e.g. the internal energy U, the Helmholtz free energy F, the Gibbs free energy G, the entropy S and the chemical potential μ), whose values depend on macroscopic parameters, such as the hydrostatic pressure P, the absolute temperature T and the composition, this last given conventionally in terms of the atomic fraction of the components $x_i = \frac{n_i}{\sum_i n_i}$, n_i being the number of atoms of i-type.

Table 1.1 *Cell size dependence of the surface to volume ratio (A_s/V) and of the ratio R of atoms sitting at the surface vs those sitting in the volume, for a cubic crystal having an atomic density of 10^{21} cm^{-3}*

Cell edge length (nm)	Volume (nm^3)	Surface area (nm^2)	A_s/V (nm^{-1})	Atoms in the volume (N_V)	Atoms at the surface (N_s)	$R = N_s/N_v$
10^7	10^{21}	$6 \cdot 10^{14}$	$6 \cdot 10^{-7}$	10^{21}	$6 \cdot 10^{14}$	$6 \cdot 10^{-7}$
10^5	10^{15}	$6 \cdot 10^{10}$	$6 \cdot 10^{-5}$	10^{15}	$6 \cdot 10^{10}$	$6 \cdot 10^{-5}$
10^4	10^{12}	$6 \cdot 10^{8}$	$6 \cdot 10^{-4}$	10^{12}	$6 \cdot 10^{8}$	$6 \cdot 10^{-4}$
10^3	10^{9}	$6 \cdot 10^{6}$	$6 \cdot 10^{-3}$	10^{9}	$6 \cdot 10^{6}$	$6 \cdot 10^{-3}$
10^2	10^{6}	$6 \cdot 10^{4}$	$6 \cdot 10^{-2}$	10^{6}	$6 \cdot 10^{4}$	$6 \cdot 10^{-2}$

For Ge and Si the actual values of atomic densities are $4.42 \cdot 10^{22}$ and $5 \cdot 10^{22}$ (cm^{-3}).

A system is said to be in *mechanical equilibrium* when there are no unbalanced mechanical forces within the system and between the system and its surrounding. The system is also said to be in mechanical equilibrium when the pressure P throughout the system and between the system and the environment is the same. This condition is typical of the liquid state but not of the solid state unless internal mechanical stresses are fully relaxed.

Two systems are said to be in mechanical equilibrium with each other when their pressures are the same.

A system is said to be in chemical equilibrium when there are no chemical reactions going on within the system or they are fully balanced, such that there is no transfer of matter from one part of the system to another due to a composition gradient. Two systems are said to be in chemical equilibrium with each other when the chemical potentials of their components are the same. A definition of the chemical potential will be given below.

When the temperature T of the system is uniform and not changing inside the system, the system is said to be in thermal equilibrium. Two systems are said to be in thermal equilibrium with each other when their temperatures are the same. By convention, the temperature is expressed in degrees Kelvin.

Mechanical equilibrium conditions in a solid phase may be modified by an imbalance of mechanical forces arising from the presence of thermal or composition gradients and of lattice misfits. This imbalance is the driving force for the migration of point defects and for the formation of extended defects during crystallization processes from a liquid phase or a vapour phase and during heteroepitaxial depositions, as will be shown in Chapter 4.

We call *transformation* any change of the structural, physical and chemical properties of a system and, therefore, of its thermodynamic state, induced by the work w carried out on it by external mechanical, thermal, chemical, magnetic or electromagnetic forces, that is as the result of interaction of the system with the ambient.

To deal properly with the properties of a transformation it is necessary to know whether it is uniquely driven by mechanical forces, or by thermal, chemical, magnetic or electromagnetic ones.

The definition of a *thermally insulated system,* originally associated to a system impervious to any exchange of heat, should be extended to the case of systems impervious to exchanges of any kind of energy of non-mechanical nature with an external system (its environment), which behaves as the source or the sink of non-mechanical energy.

In the rest of this chapter heat is identified with the electromagnetic energy emitted by a specific radiation source (the flame of a combustion process, the hot filament of a light bulb, the surface of a star, a light emitting diode (LED) or a laser), which emits a broad- or line-like spectrum of radiations, depending on the physics of the emission process. Thermal sources behave as black bodies and the property of their spectrum is described by Planck's radiation law

$$E_\lambda = \frac{8\pi hc}{\lambda^5(\mathrm{e}^{(hc/\lambda kT)} - 1)} \tag{1.1}$$

where E_λ is the emitted energy per unit volume, h is the Planck constant (6.626×10^{-34} J s), λ is the wavelength and c is the speed of light (3×10^8 m s^{-1}).

The black body radiation spectra for different black body temperatures are displayed in Figure 1.1.

As conventional hot filament light bulbs operate with a maximum colour temperature around 3500 K, their emission occurs almost entirely in the infrared, with a

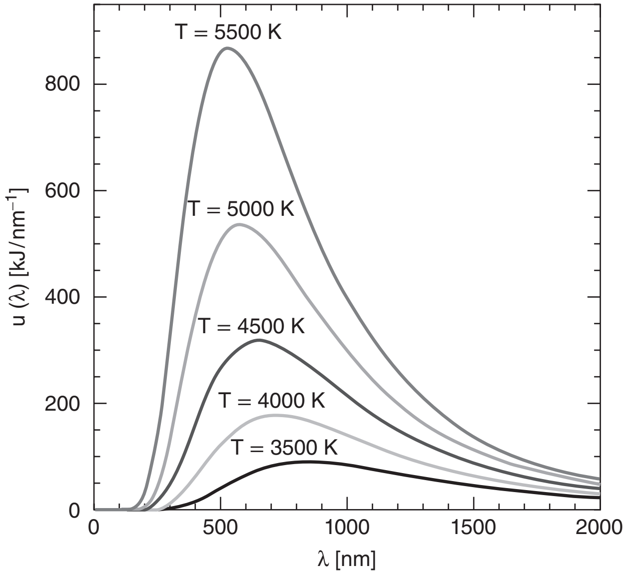

Figure 1.1 *Black body radiation curves. earthguide.ucsd.edu*

fraction not larger than 5% in the visible. This condition grants huge advantages to semiconductor-based SSL devices, whose monochromatic light emission depends on the energy gap E_g of the semiconductor used as the active substrate for quantum device applications which will be discussed later in this section.

By definition, a transformation which occurs without any input or output of heat is defined as *adiabatic.*

In this context, the work carried out by the system or supplied to the system is directly related to the variation in its internal energy U

$$\Delta U = \pm w \tag{1.2}$$

An *isothermal transformation,* however, occurs when the temperature of the system remains constant during the transformation.

Important examples of isothermal transformations are the changes of phase associated with solidification, melting, vaporization and sublimation or phase transitions of systems crystallizing in phases of different structure, as we will see later in this chapter.

In this last case, the system consists of two phases in thermodynamic equilibrium at the transformation temperature, any heat exchange from/with an external source/sink merely serves to modify the mass ratio of the two phases.

For a generic process involving a system that adsorbs heat from an external source and delivers work, the following equation holds for the variation of the internal energy U of the system

$$\Delta U = -w + q \tag{1.3}$$

where q is the energy absorbed as heat, w is the supplied work and $\Delta U = U_2 - U_1$ is the difference in the internal energy of the system.

Heat can be converted to mechanical work using a transfer fluid (liquid, gas or vapour) and operating a thermodynamic cycle (e.g. a Carnot cycle), whose maximum efficiency η is given by the second law of thermodynamics

$$\eta = \frac{W_{\text{out}}}{W_{\text{in}}} = \frac{T_s - T_a}{T_s} \tag{1.4}$$

where W_{out} and W_{in} are the output and input power, respectively, T_s is the temperature of the source and T_a is the temperature of a sink which dissipates the excess heat not converted to work.

As semiconductor-based devices play a crucial role in harvesting light and transforming it into electrical energy or emitting light as a result of a supply of electrical work, it is interesting to examine here these processes from the viewpoint of thermodynamics.

The electromagnetic energy of a radiation can be directly transformed into energy/work without making use of a transfer fluid using, for example, a semiconductor-based single- or multiple-junction device, where light is converted into electrical work qV, where q is the charge and V is the tension.[1]

Conversely, the electrical work qV supplied by polarizing an n–p junction fabricated on a direct gap semiconductor can be converted into the energy of a beam of monochromatic light. In fact, upon excitation, a fraction $\varepsilon = \frac{\hbar\nu}{kT}\eta_{\text{EQE}}$ of the generated free electrons and holes, where η_{EQE} is the quantum efficiency of the process, relaxes by radiative recombination and generates a beam of photons with energy $\hbar\nu = E_g$, where E_g is the energy gap of the semiconductor. In principle, this process could occur with a theoretical 100% efficiency, as it is submitted only to the restrictions of the first principle of thermodynamics [11]. The second law of thermodynamics provides, instead, an upper limit to the theoretical efficiency of a direct transformation of the light adsorbed by a semiconducting material into electrical work qV, occurring through the recombination of the generated free electrons and holes in an external circuit.

In this case, if the radiation is that of a black body at a temperature T, as is the case of the light emitted by the sun, the efficiency of a solar cell is again ruled by the temperature of the source T_s and that of the substrate T_a, which behaves as a selective light absorber for light photons with energy $\hbar\nu \geq E_g$ and dissipates the light not converted into energy as heat.

This upper theoretical limit cannot be reached by a single junction solar cell because only the photons of the incident light beam having an energy $\hbar\nu \geq E_g$ are absorbed and excite electrons from the valence to the conduction band.

According to Shockley and Queisser [12], the variables on which the efficiency of a single junction semiconductor-based light converter depends are: the temperature of the sun T_s

$$kT_s = qV_s \tag{1.5}$$

the temperature of the solar cell T_c

$$kT_c = qV_c \tag{1.6}$$

---

[1] It is not the author's intention to deal here with the physics of solar cells or of solid state light emitters, but only to discuss the behaviour of these devices with respect to the second law of thermodynamics.

and the energy gap of the absorber

$$E_{\mathrm{g}} = \hbar\nu_{\mathrm{g}} = qV_{\mathrm{g}} \tag{1.7}$$

so that the efficiency of the device involves only the two ratios

$$x_{\mathrm{g}} = \frac{E_{\mathrm{g}}}{kT_{\mathrm{s}}} \tag{1.8}$$

$$\text{and } x_{\mathrm{c}} = \frac{T_{\mathrm{c}}}{T_{\mathrm{s}}} \tag{1.9}$$

but depends also on the probability t_{s} that a photon of energy $\hbar\nu \geq E_{\mathrm{g}}$ would produce an electron–hole pair and on a geometrical factor ζ related to the angle of incidence of the light on the surface of the device.

The ultimate efficiency is given by the equation

$$\eta(x_{\mathrm{g}}, x_{\mathrm{a}}, t_{\mathrm{s}}, \xi) = \frac{qV}{W_{\mathrm{in}}} \tag{1.10}$$

where the product qV is the maximum electrical power output of the device and W_{in} is the power (in watts) of the incident radiation. If the light source emits, instead, a beam of monochromatic light of energy $\hbar\nu'$ and the absorber has an energy gap $E_{\mathrm{g}} = \hbar\nu'$, the system obeys only the first law and the maximum theoretical conversion efficiency should be 100%, as the electrical work qV corresponds to the variation of the internal energy of the system.

Other important kinds of transformation involve chemical forces, which drive matter fluxes among neighbouring phases of different structure and chemical composition. These transformations may by reversible or irreversible, and the latter ones are the concern of the thermodynamics of irreversible processes [13]. Most of the modern growth processes, such as physical vapour deposition (PVD), the chemical vapour deposition (CVD), atomic layer deposition (ALD) and metal-organic chemical vapour deposition (MO-CVD), which will be discussed in Chapter 4, belong to this kind of chemical processes. The systems involved in these processes are *open* systems.

1.3 Phases and Their Properties

1.3.1 Structural Order of a Phase

The properties of a phase are determined by its short- and long-range order and by its macroscopic and microscopic composition. While only short-range order is present in liquid phases, short- and long-range order is present in crystalline phases. In liquid and solid phases the short-range order can be investigated by extended X-ray absorption fine structure (EXAFS) spectroscopy [14–19].

Long-range order is investigated by diffraction experiments using X-rays, electrons or neutrons of adequate energy $h\nu$ or wavelength λ, while high resolution transmission electron microscopy (HRTEM) directly reveals short- and long-range order with sub-nanometric resolution.

Today, knowledge of local composition is an additional, crucial requirement in mesoscopic and nanoscopic applications of semiconductors. Depending on the detection range and on the chemical sensitivity required, X-ray fluorescence (XRF), infrared spectroscopy (IRS), Scanning Ion mass spectroscopy (SIMS, both time of flight (TOF)-SIMS and dynamic SIMS), Raman spectroscopy, energy dispersive X-ray spectroscopy (EDS), field-emission Auger electron spectroscopy (FE-AES), electron energy loss spectroscopy (EELS) and atom probe tomography (APT) may be used [20–24], with local resolutions ranging from a few micrometres for Fourier transform infrared (FTIR) to sub-nanometres for APT and a detection sensitivity down to 100 ppt for dynamic SIMS.

To get information simultaneously on local structure and composition, APT is particularly suited, as it allows both atomic range structural resolution and excellent chemical selectivity for the study of local order [25]. Figure 1.2 shows an interesting example of the application of APT to Ge-Sn alloys which will be discussed in Section 1.7.

A phase may consist of a single crystal or a polycrystalline aggregate. The crystalline materials found in nature, with several exceptions, consist mainly of polycrystalline aggregates, where the single crystallite size may vary from a few micrometres to several centimetres. The size- and orientation-distribution of the crystallites in a natural polycrystalline matrix is generally disordered. The interfaces between crystallites are called grain boundaries (GBs).

Synthetic crystals can be grown as single-crystalline or polycrystalline ingots, or as thick or thin polycrystalline or amorphous films, as will be shown in Chapter 4. Synthetic polycrystalline ingots can present a disordered or an ordered microstructure, depending on the growth process adopted.

GBs in natural and synthetic polycrystalline semiconductor materials (see Figure 1.3) are characterized by conditions of local disorder and electrical activity, associated with the

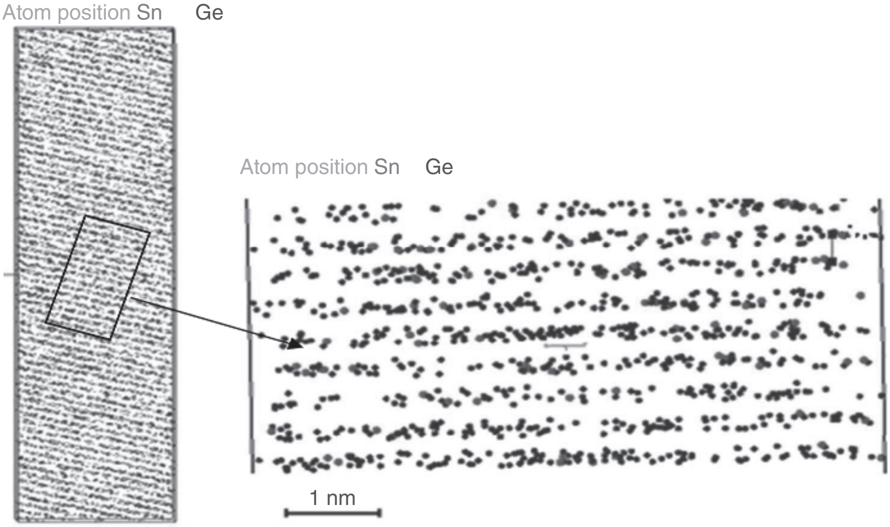

Figure 1.2 *Atom probe tomography of a Ge-Sn alloy sample: lattice planes lie in the <111> direction. Distance between the <111> planes for this sample is 0.377 nm. Kumar* et al.*, 2012, [24]. Reproduced with permission from John Wiley & Sons, Ltd*

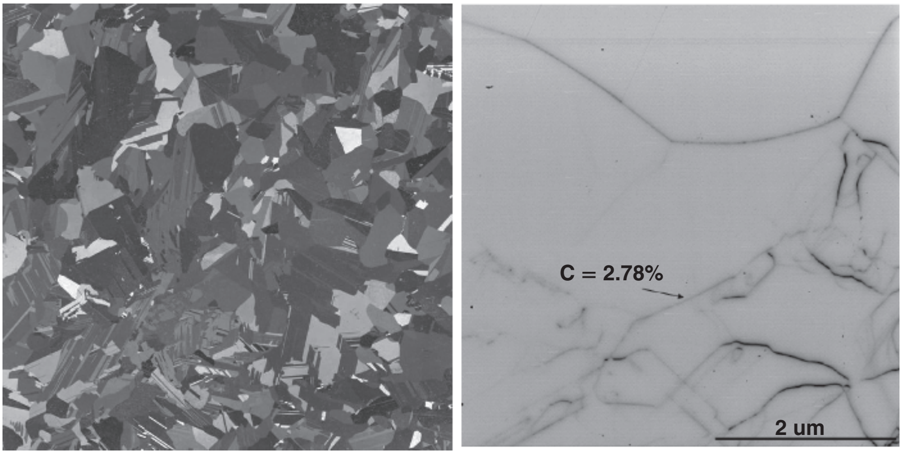

(a) (b)

Figure 1.3 *(a) Scanning electron microscopy (SEM) micrography of a multicrystalline silicon sample. (b) Light beam induced current (LBIC) image of the electrical activity of GBs associated with recombination of minority carriers minority carriers recombination*

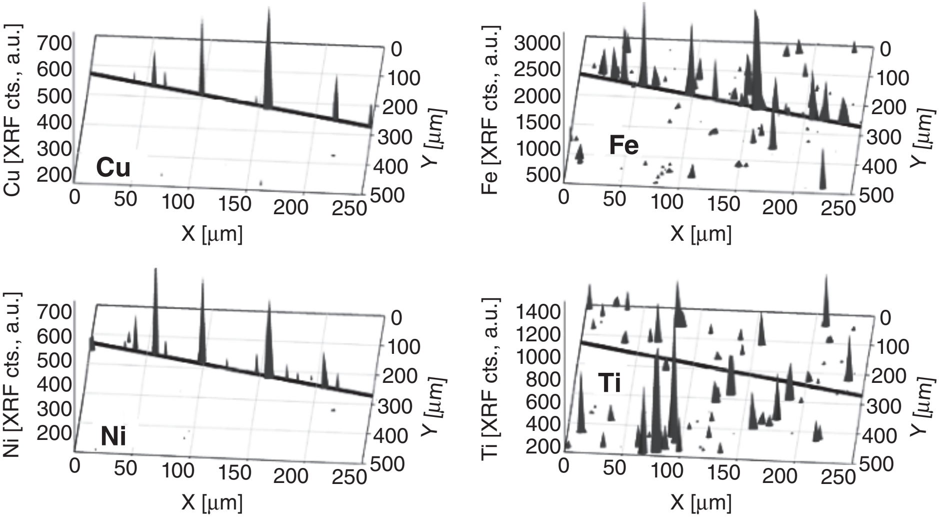

Figure 1.4 *Impurity segregation patterns in multicrystalline silicon, localized by synchrotron X-ray measurements. Buonassisi* et al.*, 2006, [28] Reproduced with permission from John Wiley & Sons, Ltd*

presence of dislocations, distorted or broken (dangling) bonds and impurities segregated on them as individual species, precipitates or microprecipitates. SIMS, APT [26], X-ray absorption microspectroscopy (μ-XAS) [27] and X-rays microfluorescence (Figure 1.4) [28–31] are the main tools for direct impurity localization on GBs in semiconductors.

One can see in Figure 1.4 that Ni and Cu impurities segregate in correspondence to a GB (the solid line in the figure), Fe segregates both at the GB and in the bulk and Ti segregates elsewhere rather than at the GB. This is already an indication that segregation of impurities at a GB is dominated by selective interactions depending on the chemical nature of the impurity.This will be discussed further in Chapters 2 and 3.

A phase may consist of a single or multiple components. Homogeneous multicomponent solid phases may be stable as a *solution* or consist of stoichiometric or non-stoichiometric compounds. In both cases, the chemical composition of a phase in thermodynamic equilibrium should be microscopically, or at least mesoscopically, homogeneous. Solid solutions of semiconductors are conventionally called *alloys,* as in the case of metallic alloys.

The *solvent* and the *solutes,* respectively, are the components which are present in larger and smaller amount, respectively, in a homogeneous solution. Solutions are discussed in terms of ideality or non-ideality of their thermodynamic behaviour.

Ideal solution behaviour, which will be discussed in Section 1.6 and occurs very rarely in semiconductor alloys, is accomplished when the components do not interact chemically with each other and distribute randomly in the condensed phase, giving rise to a compositional disorder. Deviations from the ideal behaviour are also discussed in Section 1.6 in the frame of the most recent applications of the regular solution approach [32] and of the generalized quasichemical approximations (QCAs) [33, 34].

The solution is of the substitutional-type when the solute atoms replace the solvent atoms in their stable lattice positions, as is the case for the solution of Ge, Al, B, Ga, P in Si.

The solution is of the interstitial-type when the solutes enter in interstitial positions of the lattice. This is the case for transition metals (TMs), carbon and oxygen in Si and Ge.

Several impurities in elemental or compound semiconductors, however, may enter in both lattice and interstitial positions, behaving as substitutional and interstitial species. An additional possibility is present in compound semiconductors, where impurities may share occupancy in both sublattices.

Solutes which, added in trace amounts, as is the case of B, P, Sb, Ga, As in Si, modify the carrier concentration in the semiconductor are conventionally called dopants. The impurity/dopant content is generally reported in terms of atoms cm^{-3}, parts per million by weight (ppmw) or in parts per million atoms (ppma). As the concentration of dopants and impurities in semiconductors is directly correlated with the concentration of the corresponding shallow and deep levels, the best concentration notation is that expressed in atoms cm^{-3}.

Solutions of two different compounds, such as the solutions of alkali halides, alkali earth oxides or the III–V and II–VI compounds, could be considered pseudo-binary when the content of one of the components is invariant towards the composition changes of the other components.

A solution may be stable and homogeneous in a limited range of concentration or in a continuous range of compositions. A solution of different elemental or compound semiconductors is called a multicomponent alloy.

In the case of ionic solids forming a continuous series of substitutional solid solutions, Vegard [35] observed that often the effective lattice constants change linearly with the solute concentration, expressed in terms of atomic fraction, with a law which took his name

$$a^{o}{}_{\mathrm{A}_x\mathrm{B}_{(1-x)}} = xa^{o}{}_{\mathrm{A}} + (1-x)a^{o}{}_{\mathrm{B}} \tag{1.11}$$

(where $a^{o}{}_{\mathrm{A}_x\mathrm{B}_{(1-x)}}$ is the lattice constant of the solution for a certain value of x and $a^{o}{}_{\mathrm{A}}$ and $a^{o}{}_{\mathrm{B}}$ are the lattice constants of the pure components). In spite of many experimental and theoretical proofs which show that this empirical law is very rarely followed, ideal solid solution formation in semiconductors has often been correlated in the literature on their accomplishment with Vegard's law.

As will be discussed in detail in Chapter 2, solid solution formation may involve the additional presence of point defects [36–39].

This is the case for ionic and compound semiconductors, when aliovalent dopants are added to favour the ionic conductivity or to induce a p-type or n-type carrier excess, as occurs when AlN is doped with Mg_2N_3

$$\mathrm{MgN}_{1,5} \rightarrow \mathrm{Mg}_{\mathrm{Al}} + 1.5\ \mathrm{N}_{\mathrm{N}} + 0.5\ \mathrm{V}_{\mathrm{Al}} \tag{1.12}$$

where $\mathrm{Mg}_{\mathrm{Al}}$ is a Mg atom in an Al-lattice site, behaving as an acceptor, N_{N} is a nitrogen atom in a regular lattice position and V_{Al} is an aluminium vacancy.[2]

Amorphous solids (and glasses) exhibit the absence of long-range order and the presence of distorted and broken bonds: they might be conceived as metastable phases because they transform spontaneously in crystalline phases under suitable activation of the transformation.

1.4 Equations of State of Thermodynamic Systems

1.4.1 Thermodynamic Transformations and Functions of State

The properties of a thermodynamic system are described using equations of state that account for the dependence of a specific property of the system, such as its internal energy U, on the external variables and take the general form

$$f(P, V, \ldots T) = 0 \tag{1.13}$$

A well known equation of state is that of ideal gases, written as

$$PV = RT \tag{1.14}$$

where R is the gas constant

Any transformation of a thermodynamic system from a generic state 1 to a generic state 2 is quantitatively accounted for by the corresponding changes in the function of state X which better describes the thermodynamic state of that system in the state 1 and in the state 2.

A specific character of a function of state X is that its change ΔX_{1-2} when the system passes from a state 1 to a state 2 must be independent of the path followed passing from 1 to 2.

Figure 1.5 shows such a change of state in a PV diagram, where $X_1 = P_1V_1$ and $X_2 = P_2V_2$.

A is well known, the functions which have this property are the internal energy U, the enthalpy H, the entropy S, the Helmoltz free energy F and the Gibbs free energy G.

---

[2] The Kröger and Vink notation [40] for defects in solids will be used throughout this book.

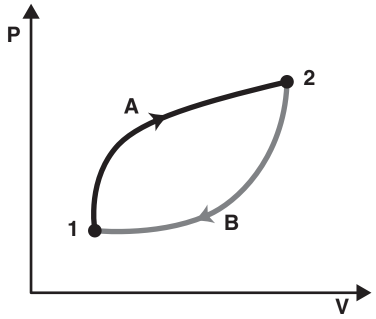

Figure 1.5 *Two possible paths for the transformation of the system from state 1 to state 2 and vice versa*

As it is experimentally impossible, although theoretically feasible, to define the absolute value of a function of state, it is common practice to define an arbitrary standard reference state, to which all changes associated with a transformation refer.

Thermodynamic transformations may be carried out reversibly or irreversibly. Reversible transformations are carried out along a continuous, formally infinite series of intermediate equilibrium states, each of them presenting a negligible energy difference from the neighbouring ones. Such types of transformations are invariant with respect to time and are fully deterministic. This condition allows one to bring a system from its initial state 1 to the final state 2, and to bring it back to the initial state 1 without hysteresis effects.

It should be noted that the transformations of real systems seldom follow full reversibility conditions, for various chemical, physical and structural reasons. The value of this procedure, however, rests in the fact that it allows calculation of the maximum work done by a transformation or the minimum work needed to induce the transformation.

1.4.2 Work Associated with a Transformation, Entropy and Free Energy

Every change in the thermodynamic state of a system is associated with an exchange of energy, and in particular of heat q and work w with the environment or with a neighbouring phase.

Like work, heat is not a function of state, because the amount of heat exchanged or supplied in any kind of transformation depends on the path followed in the transformation.

The infinitesimal change of internal energy $\mathrm{d}U$ associated with a reversible stage of a transformation is the sum of a mechanical work term and a heat term

$$\mathrm{d}U = \delta w + \delta q \tag{1.15}$$

where the partial derivative notation for the heat and work terms shows that the values of δq and δw in the transformation depend on the route followed along the transformation.

In a closed cycle $\oint \mathrm{d}U = 0$ and thus $\delta q = -\delta w$.

The work, here, is formally associated with a volumetric expansion or contraction of the system and is given by the integral

$$w = \int_1^2 p\mathrm{d}V \tag{1.16}$$

Thus, the total variation of internal energy of the system is given by the sum

$$\Delta U = \int_1^2 \mathrm{d}q \pm \int_1^2 p\mathrm{d}V = T\int_1^2 \frac{\mathrm{d}q}{T} \pm \int_1^2 p\mathrm{d}V \tag{1.17}$$

where T is the absolute temperature.

The value of the integral $\int_1^2 p\mathrm{d}V$, for an isothermal expansion/compression of an ideal gas

$$\int_1^2 p\mathrm{d}V = RT\int_1^2 \frac{\mathrm{d}V}{V} = RT\ln\frac{V_2}{V_1} \tag{1.18}$$

depends only on the values V_2 and V_1 of the final and initial states and represents the maximum work done by the system or, changing the sign, the minimum work needed to carry out the transformation.

Furthermore, the value of the integral $\int_1^2 \frac{\mathrm{d}q}{T}$ relative to a reversible transformation from state 1 to 2 at constant temperature T, is independent of the path followed, depending only on the states 1 and 2 and allows definition of a new function of state S

$$\int_1^2 \frac{\mathrm{d}q}{T} = \frac{q_2}{T} - \frac{q_1}{T} = S_2 - S_1 = \Delta S \tag{1.19}$$

which is the entropy.

According to Eq. (1.17)

$$\Delta U = T\Delta S + RT\ln\frac{V_2}{V_1} \tag{1.20}$$

It must be emphasized here that only the variation ΔU of the internal energy associated with a transformation is thermodynamically well defined and measurable. The complete definition of U for a specific system would require, in fact, an arbitrary definition of its state of zero energy. Once this reference state is fixed, any other state is univocally determined.

It is then useful to define another function of state, the Helmholtz free energy F, whose change $\Delta F = RT\ \ln\frac{V_2}{V_1}$ is a measure of the maximum (here mechanical) work done by the system in isothermal conditions.

We have, therefore, for a reversible transformation, that

$$\Delta F = \Delta U – T\Delta S \tag{1.21}$$

It should be mentioned that U, S and F are extensive properties of the system: it is, therefore, common practice to account for them in terms of unit of mass or mole.

Another thermodynamic function is G, the Gibbs free energy, whose variation is defined as the sum

$$\Delta G = \Delta U - T\Delta S + P\Delta V \tag{1.22}$$

where the $P\Delta V$ term is a measure of the work carried out on the system to pass from an initial volume Vo to the final volume V during a composition change or an isobaric and isothermal transformation. Typical examples of processes involving a volume change are chemical reactions, the sublimation of solids and a number of solid state phase transformations, as is the case of silicon dioxide (i.e. silica) (see Table 1.2)

Table 1.2 *Density and crystal structure of silica polymorphs*

Phase	Structure	Density (g cm^{-3})	Temperature (°C)	Pressure (MPa)
β-Cristobalite	Cubic	2.33	>1470	—
β-Tridymite	Hexagonal	2.28	>870	—
β-Quartz	Hexagonal	2.53	>570	—
α-Quartz	Rhombohedral	2.65	<570	—
Coesithe	Monoclinic	2.93	—	>2000
Stishovite	Tetragonal	4.30	—	>8000

The definition of G allows also the definition of enthalpy H, by means of the equation

$$\Delta H = \Delta U + P\Delta V \tag{1.23}$$

Because in semiconductor alloys the volume dependence on composition is often negligible, the Helmoltz free energy F is interchangeable with the Gibbs free energy [33].

The standard thermodynamic properties of inorganic and organic solids[3] are tabulated in the CRC Handbook of Chemistry and Physics [41]. An entry value of 0.00 for ΔH or ΔG for an element indicates the reference state of the element.

1.4.3 Chemical Potentials

The transformations discussed so far occur in the absence of matter exchanges. Of special relevance are, however, the transformations, or processes, which involve mass transfer within neighbouring phases of different structure and composition, and which occur in the vast majority of chemical and physical processes used in the technology of materials of current use.

To quantify the variation of the internal energy of a homogeneous phase associated with a defined amount of mass exchange, it is convenient to use a new function, called the chemical potential μ_i

$$\mu_i = \left(\frac{\mathrm{d}U}{\mathrm{d}n_i}\right)_{S,V,n_i} \tag{1.24}$$

which accounts for the variation of the internal energy of a phase consisting of a solution of j components, when only its i-content changes by an infinitesimal amount dn_i.

Therefore, the total change in the internal energy of a homogeneous phase associated with an infinitesimal composition change dn of all its components is given by:

$$\mathrm{d}U = T\mathrm{d}S - P\mathrm{d}V + \sum_i \mu_i \mathrm{d}n_i \tag{1.25}$$

Given the definition of the Gibbs free energy (see Eq. (1.22)), we have also

$$\mathrm{d}G = \sum_i \mu_i \mathrm{d}n_i \tag{1.26}$$

---

[3] The temperature dependence of thermodynamic functions may be found in the NIST-JANAF Thermochemical Tables, making reference to their standard conditions, corresponding to an absolute temperature of 298.15 K and a pressure of 1 atm or 101.3 kPa.

In a system consisting of only one component, Eq. (1.26) reads

$$\mu_i = \left(\frac{\mathrm{d}G}{\mathrm{d}n_i}\right)_{T,P} \tag{1.27}$$

and

$$G_i^o = \mu_{\grave{\mathrm{\imath}}} \tag{1.28}$$

where the chemical potential μ_i takes the value of the molar free energy $G^{\mathrm{o}}{}_i$ of the species i.

Let us now denote by $\left(\frac{\mathrm{d}G}{\mathrm{d}n_1}\right)_{\alpha\rightarrow\beta}$ the work needed to transfer an infinitesimal amount $\mathrm{d}n_i$ of the species i from the phase α to the phase β and by $\left(\frac{\mathrm{d}G}{\mathrm{d}n_1}\right)_{\beta\rightarrow\alpha}$ the work needed to transfer the same infinitesimal amount of mass $\mathrm{d}n_i$ from the phase β to the phase α, at the equilibrium coexistence temperature $T_{\alpha.\beta}$ in the absence of any change of the concentration of the other species in both α and β.

To maintain the system in full equilibrium conditions during and after the transformation ($\mathrm{d}G = 0$)

$$\left(\frac{\mathrm{d}G}{\mathrm{d}n_i}\right)_{\mathrm{a}\rightarrow\beta} = \left(\frac{\mathrm{d}G}{\mathrm{d}n_i}\right)_{\beta\rightarrow\alpha} \tag{1.29}$$

and

$$\mu_i^{\alpha} = \mu_i^{\beta} \tag{1.30}$$

The equilibrium between phases of different composition is, therefore, given by a set of equations (1.30) for each j component of the solution. The relationship between μ_i and the composition will be given in Section 1.5.

1.4.4 Free Energy and Entropy of Spontaneous Processes

Let us now consider a thermally isolated system consisting, as before, of an intimate mixture of two phases α and β of identical composition in mutual equilibrium.

It holds, therefore, in equilibrium conditions

$$T_{\alpha} = T_{\beta}; G_{\alpha} = G_{\beta} \tag{1.31}$$

and

$$S = S_{\alpha} + S_{\beta} \tag{1.32}$$

if the two phases maintain their original integrity during and after the mass transfer process.

Let us suppose, instead, that the two phases are at different temperatures

$$T_{\alpha} > T_{\beta} \tag{1.33}$$

In this case a heat flux[4] $\boldsymbol{\Phi}_q = \frac{\mathrm{d}q}{\mathrm{d}t}$ (where t is the time) would spontaneously flow from α to β until $T_{\alpha} = T_{\beta}$. Consequently, we will have a change of entropy of each of the two phases

---

[4] Heat fluxes may involve conduction, convection and radiation.

$\mathrm{d}S_\alpha = -\left(\frac{\mathrm{d}q}{T_\alpha}\right)$ and $\mathrm{d}S_\beta = \left(\frac{\mathrm{d}q}{T_\beta}\right)$ and a variation of entropy dS of the system

$$\mathrm{d}S = -\left(\frac{\mathrm{d}q}{T_\alpha}\right) + \left(\frac{\mathrm{d}q}{T_\beta}\right) = \mathrm{d}q\left(\frac{1}{T_\beta} - \frac{1}{T_\alpha}\right) > 0 \tag{1.34}$$

Therefore, $\mathrm{dS} > 0$ for a spontaneous process. We expect, similarly, that $\mathrm{d}F < 0$ and $\mathrm{d}G < 0$ for a spontaneous process.

1.4.5 Effect of Pressure on Phase Transformations, Polymorphs/Polytypes Formation and Their Thermodynamic Stability

Knowledge of the effects of an applied gas or hydrostatic pressure on the properties and the stability of a phase has important technological outcomes, as it may allow, as a not exclusive example, the synthesis of materials outside conventional temperature and pressure conditions, where their preparation would be challenging or impossible.

As an example, the equilibrium vapour pressure or the decomposition pressure of phosphide, arsenide and nitride alloys may be so high at their growth temperatures (even well below the melting point) as to induce partial or full decomposition of the material or/and the onset of non-stoichiometry. This would make their growth as bulk single crystal or single crystalline- or polycrystalline-thin films very challenging, unless the applied gas pressure is sufficiently high to prevent the decomposition.

Meanwhile, an understanding of the effects of a mechanical strain, arising from external or internal sources of stress, on the properties of a material, is important in order to optimize its growth or deposition processes and to accomplish for the presence of extended defects. A typical, but not exclusive example is the dislocation generation induced by lattice mismatch, occurring in the heteroepitaxial deposition processes which will be discussed in Chapter 4.

As a further example, the combined effect of temperature and applied pressure may induce a sequence of phase transformations in elemental or compound semiconductors. In this section we will deal with the effects of an externally applied hydrostatic pressure on the equilibrium transformation temperatures of liquid/solid systems and of solid/solid systems, leaving the analysis of the effects of internal mechanical stresses on defect generation to later chapters.

The effect of the applied pressure on the melting temperature T_f and the molar volume of a number of model systems, including Ge and Si, is reported in Table 1.3 [42, 43], while Table 1.4 reports the value of the critical pressure at which typical phase transformations of alkali halides and oxides occur.

Pressure-induced phase transformations in silicon and germanium were studied by Bundy [44], who showed a transition from semiconductor to metallic character in both cases, although the silicon transition was more sluggish. In the case of silicon this transition occurs at 10–13 GPa and is associated with a volume decrease of 22%. Diamond anvil cell and micro- and nano-indentation experiments showed the formation of at least 12 different silicon polymorphs following the application of increasing pressures [45]. Other examples can be found within compound semiconductors (see Section 1.7), as is the case of GaAs, which crystallizes in the cubic zinc blende structure at ambient pressures but undergoes a transition to at least two orthorombic structures, the first of which occurs at 12 ± 1.5 GPa at 300 K [46]. CdS, CdSe and ZnS, eventually, show unique behaviour

Table 1.3 *Effect of the applied hydrostatic pressure on the melting temperature of model systems*

Material	T_f(K)	$\Delta_f H$ (kJ mol^{-1})	ΔV_m(cm^3 mol^{-1})	ΔT_{calc} (0.9 GPa)	ΔT_{exp} (0.9 GPa)
H_2O	273.2	6.012	−1.6308	−7.5	−7.4
Sn	505	7.03 (white tin)	+0.4617	+3.4	3.28
Bi	544.7	11.3	−0.7147	−3.56	−3.10
Si [42]	1687	50.21	−6.767	−20.46	900 (10 GPa)
Ge	1211.4	34.7	−20.121	−78.048	—
Al [43]	933.47	10.71	+7.473	+58.62	1500 (10 GPa)

Adapated from Soma and Matsuo, 1982, [42] and from Hänström and Lazor, 2000, [43].

Table 1.4 *Critical phase transformation pressures for a number of model systems*

Material	Phase transformation	P_c (GPa)	$\Delta V_{m\alpha\to\beta}$(cm^3 mol^{-1})	$\Delta H_{\alpha\to\beta}$(kJ mol^{-1})
KCl	NaCl → CsCl	1.96	−4.11	8.03
KBr	NaCl → CsCl	1.80	−4.17	7.65
RbCl	NaCl → CsCl	0.57	−6.95	3.39
ZnO	Wurtzite → NaCl	8.86	−2.55	19.23
SiO_2	Quartz → coesite	1.88	−2.0	2.93
SiO_2	Coesite → stishovite	9.31	−6.6	52.27

in view of their wurtzite–zinc blende transformations which resemble quasi-equilibrium conditions.

An even more important case of polymorphism for its relevance to material applications is that exhibited by carbon and silicon carbide, which will be discussed in Section 1.7. The polymorphism of silicon carbide, with its more than 200 different polymorphs, falls into the category of polytypism, as each different polymorph can be regarded as built up by stacking layers of (nearly) identical structure and composition, and the difference lies only in their stacking sequence. Polytypism is, therefore, a special case of polymorphism where the two-dimensional translations within the layers are essentially preserved [47].

While the evaluation of the critical pressure at which a structural phase transformation occurs may be obtained by *ab initio* or molecular dynamics (MD) computations, the effect of the pressure on the phase transformation temperature $T_{\alpha\to\beta}$ of a generic material may be deduced by the Clausius–Clapeyron equation

$$\frac{dP}{dT} = \frac{\Delta H_{\alpha\to\beta}}{T_{\alpha\to\beta}\Delta V_{\alpha\to\beta}} \tag{1.35}$$

where $\Delta H_{\alpha-\beta}$ is the enthalpy of the $\alpha \to \beta$ transformation, $T_{\alpha-\beta}$ is the equilibrium transformation temperature and $\Delta V_{\alpha-\beta}$ is the volume change associated with the $\alpha \to \beta$ transformation.

Equation (1.35) could also be written

$$dT_{\alpha\to\beta} = \frac{T_{\alpha\to\beta}\Delta V_{\alpha\to\beta}}{\Delta H_{\alpha\to\beta}} dP \tag{1.36}$$

for the change in the transformation temperature as a function of pressure.

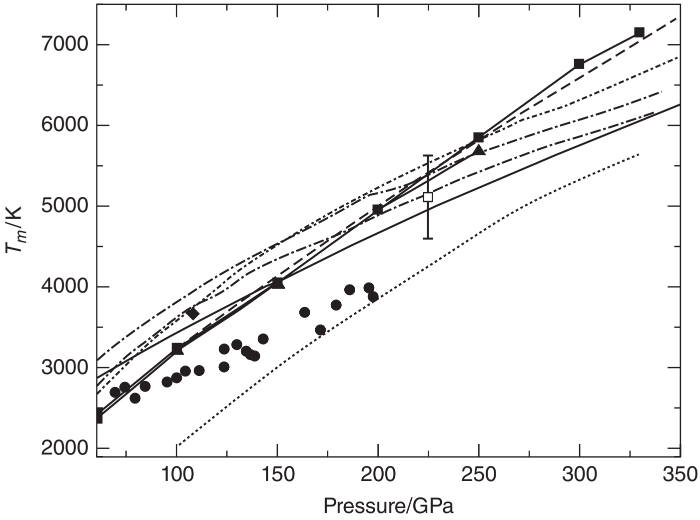

Figure 1.6 *Effect of the pressure on the melting point of iron. Luo* et al.*, 2011, [48]. Reproduced with permisssion from American Chemical Society*

If both the $\Delta H_{\alpha-\beta}$ and $\Delta V_{\alpha-\beta}$ terms are taken as independent of both temperature and pressure, a linear increase or decrease of the melting temperature is expected with increase in the applied pressure, depending on whether there is a volume contraction or expansion on melting, as shown in Table 1.3.

The melting temperature, therefore, increases with the applied pressure in the case of metals, see Figures 1.6 and 1.7, and decreases in semiconductors, see Figure 1.8 for the typical case of silicon, because, almost systematically, there is, on freezing, a volume contraction in metals and a volume expansion in elemental semiconductors [43, 48–50]. As the Clapeyron equation has been deduced for conditions very close to the equilibrium melting temperature $T^{o}{}_{\alpha-\beta}$, we might expect sensible deviations from the linearity at elevated pressures, as is, in fact, shown in Figures 1.6–1.8.

The validity of the Clapeyron equation may be, however, extended to a wider pressure and temperature range once the pressure and temperature dependence of the $\Delta H_{\alpha-\beta}$ and $\Delta V_{\alpha-\beta}$ terms are known or could be calculated.

A critical role is expected to be played by the $\Delta V_{\alpha-\beta}$ term in Eqs. (1.35) and (1.36), which is related to the effect of the applied pressure on the density of the two phases in equilibrium. Density should decrease in absolute value with increase in the applied pressure, that is with increase in the mechanical deformation. Figure 1.9 shows, as an example, the calculated strong decrease of the atomic volume of hexagonal close packed (HCP) solid iron with increase in pressure, which is associated with a decrease in the $\Delta V_{\alpha-\beta}$ term value from 0.16 cm^3 mol^{-1} at atmospheric pressure to 0.10 cm^3 mol^{-1} at 250 GPa [48].

The effect of volume changes on the melting temperature is phenomenologically taken into account by the Lindeman equation [51] in its integrated form [43]

$$T_{\mathrm{m}} = T^{\mathrm{o}}_{\mathrm{m}}\left(\frac{V_{T_{\mathrm{m}}}}{V^{\mathrm{o}}_{T_{\mathrm{m}}}}\right)^{\frac{2}{3}} \exp\left[\frac{2\gamma^{\mathrm{o}}}{q}\left(1-\frac{V_{T_{\mathrm{m}}}}{V^{\mathrm{o}}_{T_{\mathrm{m}}}}\right)^{q}\right] \tag{1.37}$$

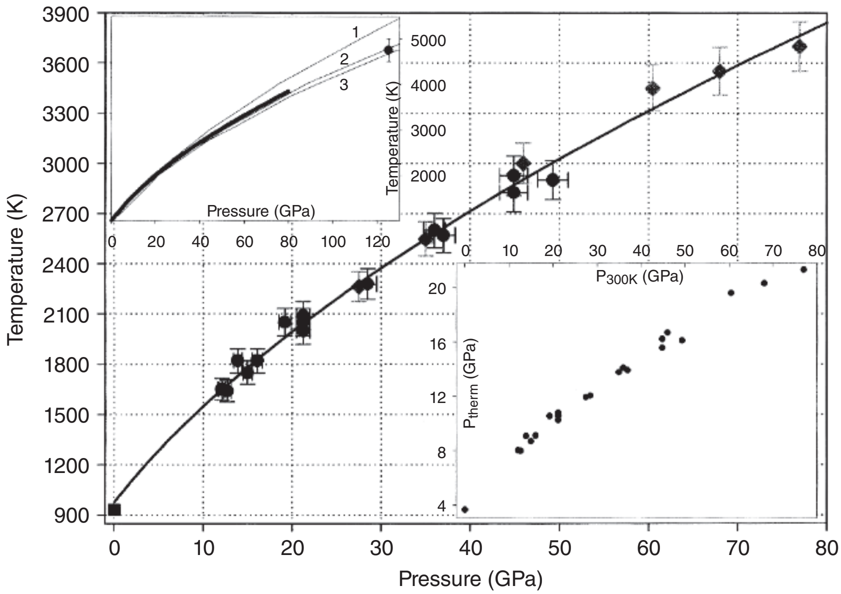

Figure 1.7 *Experimental and calculated melting temperatures of aluminium under high pressure. Hänström & Lazor, 2000, [43]. Reproduced with permisssion from Elsevier*

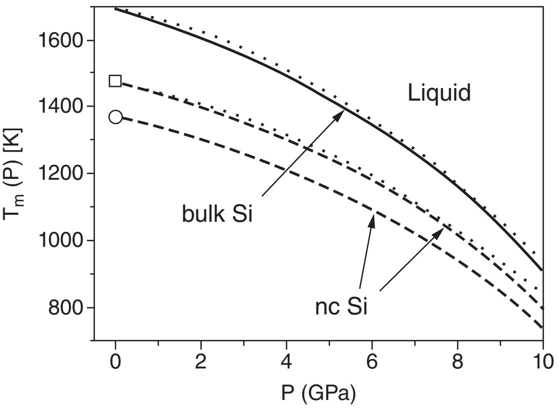

Figure 1.8 *Effect of the pressure on the melting point of silicon (the effect of crystallite size is also shown). Yang* et al.*, 2003, [49]. Reproduced with permisssion from Institute of Physics and Q. Jiang*

where $\gamma = \gamma^{\mathrm{o}}\left(\frac{V_{T_{\mathrm{m}}}}{V^{\mathrm{o}}_{T_{\mathrm{m}}}}\right)^{q}$, $V^{\mathrm{o}}_{T_{\mathrm{m}}}$ is the molar volume at the onset of linearity deviations, $V_{T_{\mathrm{m}}}$ is the molar volume at the experimental melting temperature, $T^{\mathrm{o}}_{\mathrm{m}}$ is the melting temperature in correspondence to $V^{\mathrm{o}}_{T_{\mathrm{m}}}$ and q is the volume dependence for γ, often taken equal to 1.

The Lindeman equation has been successfully applied to fit the experimental points of Figure 1.7 for the case of Al, where $V^{\mathrm{o}}_{T_{\mathrm{m}}}$ is the experimental molar volume of Al at 100 kPa,

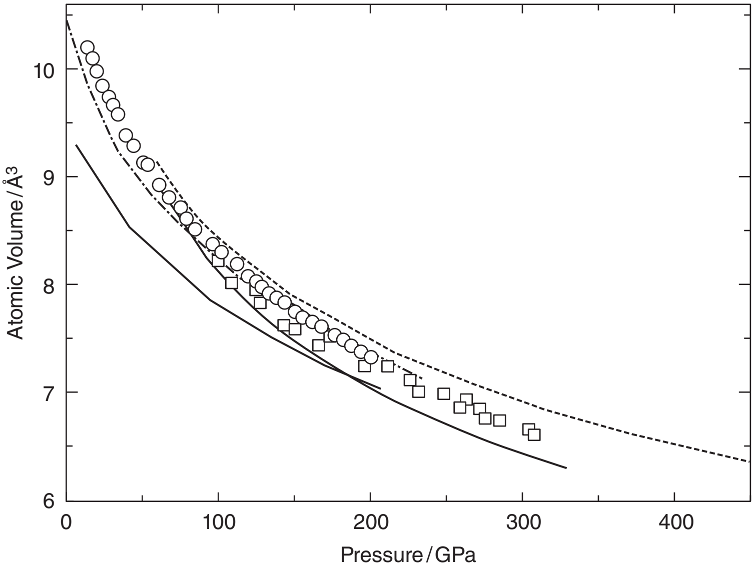

Figure 1.9 *Atomic volume of iron as a function of the applied pressure. Luo* et al.*, 2011, [48]. Reproduced with permisssion from American Chemical Society*

V_{T_m} is the experimental molar volume of Al at the melting temperature under pressure, T_m^o is the melting temperature of Al at 933 K and 100 kPa and q is taken equal to 1 [43].

Alternatively, when the data concerning the pressure dependence of the melting temperature of a material are known experimentally they could be satisfactorily fitted, as was done for the case of Al, see again Figure 1.7, using the empirical Simon's melting equation:

$$T_\mathrm{m} = T_\mathrm{m}^\mathrm{o}\left(\frac{P}{A} + 1\right)B \tag{1.38}$$

where T_m^o is the experimental value of the melting temperature of Al at 100 kPa and A and B are fitting parameters, treating aluminium as an harmonic Debye solid.

It is important to remark here that, different from the past, there is a growing research interest today concerning the behaviour of metals and semiconductors under elevated pressures. Independently of the advances in the understanding of their basic physico-chemical behaviour, knowledge of the effect of the hydrostatic pressure on the melting temperature is important for the optimization of growth and further thermal processes of high temperature melting or highly corrosive semiconductor materials. In several cases a decrease in the melting temperature might permit the use of cheaper crucibles or reduce corrosion effects which are more detrimental as the operational temperatures increase, as well as reducing energy costs. This would be the case for silicon, for which the growth of single crystalline or multicrystalline ingots could be carried out at about 1000 K at 10 GPa instead of at 1685 K at ambient pressure. Diamond is a limiting case, as will be seen in Section 1.7.6, where temperatures of several thousand degrees K and pressures of 1000 GPa might be obtained by shock waves [52].

The growing interest in pressure effects on the melting temperatures of metals and semiconductors is demonstrated by a number of recent theoretical studies [42, 49, 53–56] dedicated to the melting behaviour of face centred cubic (FCC) metals, semiconductors and semiconductor alloys under pressure.

All these studies are based on the application of a variant of the Lindeman's melting law [51] which postulates that the melting process in FCC solids occurs when the root-mean-square displacement, $\langle u^2 \rangle^{1/2}$ of the lattice vibrations reaches a critical fraction x_{m} of the nearest-neighbour distance and that this critical fraction is assumed to be the same for all crystalline solids. It was, however, shown that in various cubic metals and alkali halides this fraction was actually not constant. A better account with the experimental data is obtained [54] by assuming as the critical fraction x_{m} for melting the ratio of twice the root-mean-square displacement $\langle u^2 \rangle^{1/2}$, at the melting temperature, T_{m}, to the nearest-neighbour distance, $R_1 = (2^{1/2}\, a)/2$, given by

$$x_{\mathrm{m}} = \frac{\langle u^2 \rangle^{1/2}}{R_1} \tag{1.39}$$

Considering, further, the pressure dependence of the mean square displacement, $\langle u^2 \rangle$ and of the nearest-neighbour distance, R_1, and assuming as before x_{m} as the melting criterion, it is possible to estimate the pressure effect on the melting temperature T_{m} when both the following relations are simultaneously satisfied

$$x_{\mathrm{m}} = \frac{\langle u^2 \rangle^{1/2}_{T_{\mathrm{m}},P}}{R_1(P)} \tag{1.40}$$

$$R_1(P) = \left[\frac{\Omega\,(P)}{\Omega^{\mathrm{o}}}\right] R_1(\Omega^{\mathrm{o}}) \tag{1.41}$$

where Ω^{o} and $\Omega(\mathrm{P})$ are the crystal volumes under atmospheric pressure and under a pressure P, respectively, and $R_1(\Omega^{\mathrm{o}})$ is the nearest-neighbour distance at atmospheric pressure.

The comparison between the experimental and calculated values is reported in Figure 1.10, which shows that the calculated values deviate slightly from the experimental ones, still exhibiting a linear dependence on the applied pressure.

Among issues not considered here, those concerning the pressure-induced widening of the solid solubility domains of impurities in silicon and germanium has relevant technological consequences and will be discussed in Section 1.7.5.

1.4.6 Electrochemical Equilibria and Electrochemical Potentials of Charged Species

It is a common practice in physical chemistry and solid state physics [7, 9] to discuss the equilibrium properties of charged species, such as ions, charged point defects or electrons, between phases of equal or different chemical compositions, like two differently doped semiconductors or two solutions of electrolytes, using the electrochemical potential η_i formally defined as

$$\eta_i^{\alpha} = \mu_i^{\alpha} + ze\varphi_{\alpha} \tag{1.42}$$

where μ_i is the chemical potential of the i species, ze is its charge and φ is the internal potential of the phase.

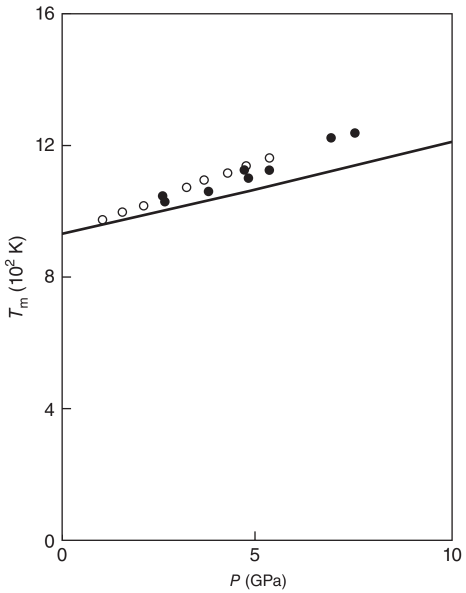

Figure 1.10 *Calculated dependence of the melting point of Al as a function of the pressure (solid line): ○ and ● are experimental points. Kagaya* et al.*, [54]. Reproduced with permisssion from Chapman and Hall)*

The condition of equilibrium of a charged species $i^{\pm z}$ between two phases α and β requires that

$$\eta_i^{\alpha} = \eta_i^{\beta} \tag{1.43}$$

$$\text{and that } (\varphi_{\alpha} - \varphi_{\beta}) = 0 \tag{1.44}$$

when the composition of the two neighbouring phases is equal, that is $\mu_i^{\alpha} = \mu_i^{\beta}$.

The equilibrium condition for a charged species i present in two neighbouring phases α and β of different chemical compositions still requires that

$$\eta_i^{\alpha} = \eta_i^{\beta} \tag{1.43}$$

but that a potential drop $\Delta\varphi$ occurs at the α/β interface

$$\Delta\varphi = (\varphi_{\beta} - \varphi_{\alpha}) = \frac{\mu_i^{\alpha} - \mu_i^{\beta}}{zF} \tag{1.45}$$

It is very important to note here that the electrochemical potentials refer to defined charged species (point defects and electrons in metals and semiconductors, ions in electrolytes) while the internal potential is a property of the phase. It should be additionally noted that a difference $\Delta\varphi = (\varphi_{\beta} - \varphi_{\alpha})$ in the internal potential of two phases is physically defined and directly measurable only if the two phases have identical chemical composition.

This means that a system where a difference of internal potentials exists should be properly connected to two electrodes of equal chemical composition to make the difference $\Delta\varphi = (\varphi_{\beta} - \varphi_{\alpha})$ directly measurable.

We will discuss in the Appendix a direct application of these concepts when dealing with the equilibrium conditions occurring in a galvanic chain used to measure the Gibbs free energy of formation of compound semiconductors.

1.5 Equilibrium Conditions of Multicomponent Systems Which Do Not React Chemically

For multicomponent systems, the dependence of every thermodynamic function of state or of every extensive property (as an example the volume and the density) on the composition is normally expressed in terms of the atomic/molar fraction $x_1 = \frac{n_i}{\sum_i n_i}$, where n_i is the number of atoms/moles of the component ***i***.

For heterogeneous mixtures of two phases, each consisting of an elemental component A or B, and each assumed fully insoluble in the other,[5] the Gibbs free energy, like any other extensive property of the system, is given by the sum

$$G = x_{\mathrm{A}} G^{\mathrm{o}}_{\mathrm{A}} + x_{\mathrm{B}} G^{\mathrm{o}}_{\mathrm{B}} = x G^{\mathrm{o}}_{\mathrm{A}} + (1 - x) G^{\mathrm{o}}_{\mathrm{B}} \tag{1.46}$$

where $G^{\mathrm{o}}_{\mathrm{A}}$ and $G^{\mathrm{o}}_{\mathrm{B}}$ are the molar free energies of the components A and B, at the temperature of the experiment.

The dotted curve in Figure 1.11 fits the linear dependence of the Gibbs free energy of the heterogeneous mixture of A and B on composition, according to Eq. (1.46).

In the same figure the hypothetical[6] dependence of G on the composition x is reported for the case of a system exhibiting complete mutual solubility of the components A and B. Depending on the temperature, the solution will be either liquid or solid. We define as the free energy of mixing $\Delta G_{\mathrm{mix}}\ (T, P, x)$ the free energy excess associated with the formation of a solution from the pure elements, whose value is supposed to depend on the composition, temperature and pressure.

The dependence of $\Delta G_{\mathrm{mix}}\ (T, P, x)$ on the composition at constant temperature and pressure might be formally deduced, starting from the definition of the chemical potential given by the Eq. (1.27), written for a system of n components.

$$\mu_i = \left(\frac{\mathrm{d}G}{\mathrm{d}n_i}\right)_{T,P,n_1 \ldots n_j} \tag{1.27}$$

Therefore, the molar free energy G_{soln} of a solution is given by the sum

$$\sum_1^i x_i \mu_i = G_{\mathrm{soln}} \tag{1.47}$$

where the sum is extended to all the components of the solution.

For a binary system we can write for the molar free energy of the solution

$$G_{\mathrm{soln}} = x_{\mathrm{A}} \mu_{\mathrm{A}} + x_{\mathrm{B}} \mu_{\mathrm{B}} \tag{1.48}$$

---

[5] Full insolubility is not an equilibrium condition, as a limited solubility of A in B and B in A, respectively, increases the thermodynamic stability of the phase due to an entropic mixing contribution to the free energy. Instead of pure A and B, we should therefore use as components A saturated in B and B saturated in A, respectively.

[6] The actual shape of the free energy curve depends on the properties of the solution.

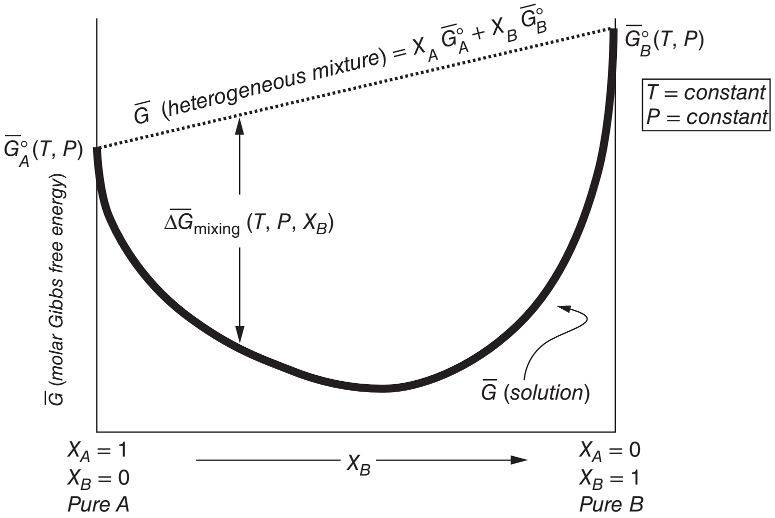

Figure 1.11 *Composition dependence of the Gibbs free energy G of a heterogeneous mixture of the components A and B (dotted curve) and of a solution of A and B (solid curve). Courtesy of W. Craig Carter, MIT*

and derive a relationship between G_{soln} and the chemical potentials, for any value of x between $x_A = 1$ and $x_B = 1$, by writing first

$$dG_{\text{soln}} = \mu_A dx_A + \mu_B dx_B = (\mu_B - \mu_A)dx_B \tag{1.49}$$

where

$$x_A + x_B = 1; x_B = 1 - x_A; dx_A = -dx_B \tag{1.50}$$

It is then possible to write

$$\frac{dG_{\text{soln}}}{dx_B} = \mu_B - \mu_A \tag{1.51}$$

and

$$\mu_B = \mu_A + \frac{dG_{\text{soln}}}{dx_B} \tag{1.52}$$

Therefore, from Eq. (1.48)

$$G_{\text{soln}} = (1 - x_B)\mu_A + x_B\left[\mu_A + \left(\frac{dG}{dx_B}\right)\right] = \mu_A + x_B\left(\frac{dG}{dx_B}\right) \tag{1.53}$$

and

$$\mu_A = G_{\text{soln}} - x_B\left(\frac{dG_{\text{soln}}}{dx_B}\right) \tag{1.54}$$

$$\mu_B = \mu_A + \frac{dG_{\text{soln}}}{dx_B} = G_{\text{soln}} - x_B\left(\frac{dG_{\text{soln}}}{dx_B}\right) + \frac{dG_{\text{soln}}}{dx_B} = G_{\text{soln}} + (1 - x_B)\left(\frac{dG_{\text{soln}}}{dx_B}\right) \tag{1.55}$$

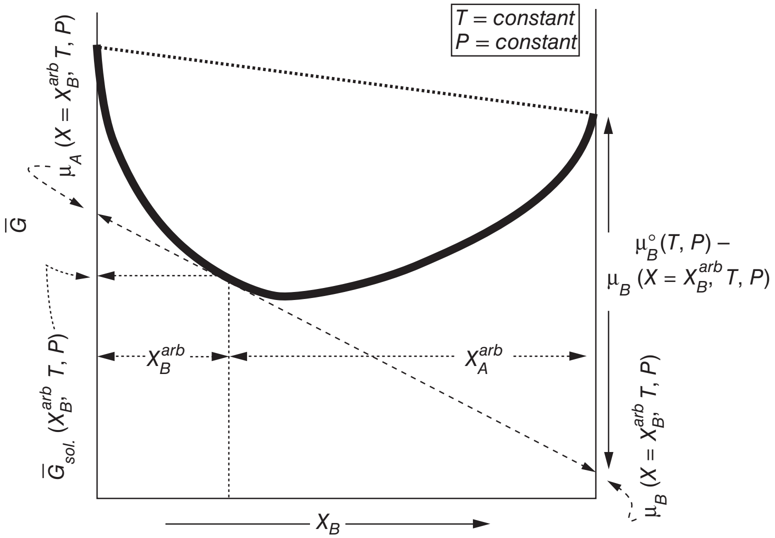

Figure 1.12 *Geometrical determination of the values of the chemical potentials of the components of a binary solution using the common tangent procedure (dotted line in the figure). The composition dependence of the Gibbs energy, as shown by the solid line, is arbitrary. Courtesy of W. Craig Carter, MIT*

where $\frac{dG_{\mathrm{soln}}}{dx_{\mathrm{B}}} = \frac{G_{\mathrm{soln}}-\mu_{\mathrm{A}}}{x_{\mathrm{B}}}$ is the equation of the tangent to the curve $G_{\mathrm{soln}}(x)$ for any arbitrary value of the composition x_{B} between $x_{\mathrm{B}} = 0$ and $x_{\mathrm{B}} = 1$ and the terms $(1 - x_{\mathrm{B}})\left(\frac{dG_{\mathrm{soln}}}{dx_{\mathrm{B}}}\right)$ and $x_{\mathrm{B}}\left(\frac{dG_{\mathrm{soln}}}{dx_{\mathrm{B}}}\right)$ are the values of the intercepts of the tangent to the curve $G_{\mathrm{soln}}(x)$ for a defined value of composition x_{B}, as is shown in Figure 1.12.

The equilibrium composition of two coexisting phases, both solids or one liquid and the other solid, may be easily found by imposing the condition (1.30) for each component of the system.

In the case of a binary $\mathrm{A}_x\mathrm{B}_{1-x}$ system, the equilibrium condition among a liquid and solid phase should be written

$$\mu_{\mathrm{A}}{}^{1}(x_{\mathrm{A}}{}^{1}) = \mu_{\mathrm{A}}{}^{\mathrm{s}}(x_{\mathrm{A}}{}^{\mathrm{s}}) \tag{1.56}$$

$$\mu_{\mathrm{B}}{}^{1}(x_{\mathrm{A}}{}^{1}) = \mu_{\mathrm{B}}{}^{\mathrm{s}}(x_{\mathrm{A}}{}^{\mathrm{s}}) \tag{1.57}$$

To determine the equilibrium composition of the solid and liquid phases at a given temperature (and pressure) it is necessary to solve Eqs. (1.56) and (1.57) simultaneously on the basis of the available information on the dependence of the chemical potentials on the composition, as deduced from measurements or by solution models, as will be shown in the next section. Alternatively, it is possible to use the geometrical procedure illustrated in Figure 1.12 called the common tangent procedure, when the composition dependence of the Gibbs free energy G^1 and G^{s} of the liquid and solid phases, respectively, is experimentally available or can be suitably modelled.

One can see that the equilibrium condition of the system of Figure 1.13 implies the coexistence of a liquid phase of composition $x^1{}_{\mathrm{B}}$ and a solid phase of composition $x^{\mathrm{s}}{}_{\mathrm{B}}$. A liquid phase of composition x^1 would be thermodynamically metastable because there will be a

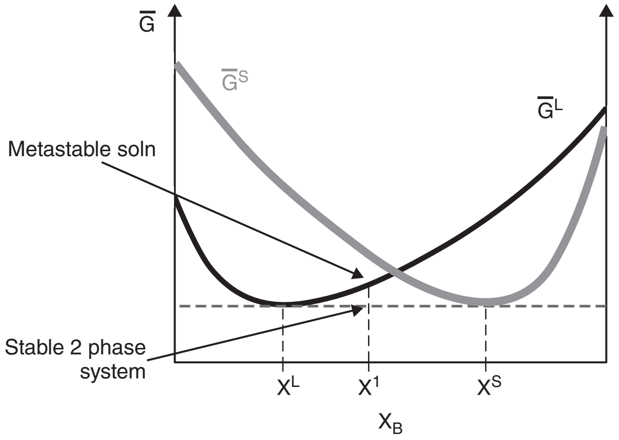

Figure 1.13 *Graphical representation of the coexistence equilibrium conditions of a solid and liquid phase: the black curve pertains to the liquid phase and the blue one to the solid phase. Adapted from http//ocw.mit.edu licensed under the Creative Commons Attribution 3.0 Unported license*

decrease in free energy ΔG_{x1} if this metastable solution spontaneously decomposes into two phases.

To proceed further it is necessary to find some quantitative relationship between the chemical potentials and the composition of a phase or other measurable variables proportional to the concentration of the components.

This is immediate for the case of the equilibrium between a condensed and a vapour phase, under the assumption that the vapour phase behaves as an ideal gas. This assumption could be applied to a dilute vapour phase provided each i component of the condensed phase sublimes without chemical changes arising from incongruent sublimation, pyrolysis, chemical reactions or polymerization, a condition violated in many practical circumstances, as for example during crystal growth processes of semiconductors from metal-organic precursors [57], but ignored in the following analysis.

Under these conditions it is possible to find a direct relationship between the Gibbs free energy, the chemical potential and the pressure p of the vapour phase using the equation

$$\left(\frac{\mathrm{d}G}{\mathrm{d}p}\right) = V = \frac{RT}{p} \tag{1.58}$$

which at constant temperature can be written as

$$\mathrm{d}G = RT\frac{\mathrm{d}p}{p} \tag{1.59}$$

After integration

$$\Delta G = \int_{p^o}^{p} \mathrm{d}G = RT\int_{p^o}^{p} \frac{\mathrm{d}p}{p} = RT\ln\frac{p}{p^o} \tag{1.60}$$

$$\Delta G = \mu - \mu^o = RT\ln\frac{p}{p^o};\ \mu = \mu^o + RT\ln\frac{p}{p^o} \tag{1.61}$$

where p^o is an arbitrary reference pressure.

The equilibrium conditions between a condensed (liquid or solid) phase s and its vapour phase v may be then deduced applying to each component i of the system the equilibrium condition (1.30)

$$\mu_i^{\alpha} = \mu_i^{\beta} \tag{1.30}$$

and writing

$$\mu_i^{\mathrm{s}} = \mu_i^{\mathrm{v}} = \mu_i^{\mathrm{o,v}} + RT\ln\frac{p_i}{p_i^{\mathrm{o}}} \tag{1.62}$$

where p_i is the partial pressure of the component i for an arbitrary value of the composition of the condensed phase, p_i^{o} is the partial pressure of the pure component i and $\mu_i^{\mathrm{o,v}}$ is the chemical potential of the pure component i in the vapour phase.

It is then possible to define a new function, λ, the absolute activity

$$\lambda = \mathrm{e}^{\mu/RT} \tag{1.63}$$

which allows one to redefine the equilibrium conditions with the following equation

$$\lambda_i^{\mathrm{s}} = \lambda_i^{\mathrm{v}} \tag{1.64}$$

After substitution of $\mu_i^{\mathrm{v}} = \mu_i^{\mathrm{ov}} + RT \ln \frac{p}{p^{\mathrm{o}}}$ in λ, we obtain

$$\lambda_i^{\mathrm{v}} = \lambda_i^{\mathrm{ov}} \left(\frac{p}{p^{\mathrm{o}}}\right) \tag{1.65}$$

and

$$\frac{\lambda_i^{\mathrm{v}}}{\lambda_i^{\mathrm{ov}}} = \frac{p}{p^{\mathrm{o}}} \tag{1.66}$$

If we define the *chemical activity* a_i of the component i in solution as the ratio $\frac{\lambda_i{}^{\mathrm{s}}}{\lambda_i^{\mathrm{os}}}$

$$a_i = \frac{\lambda_i^{\mathrm{s}}}{\lambda_i^{\mathrm{os}}} = \frac{p}{p^{\mathrm{o}}} \tag{1.67}$$

It is possible, according to Eqs. (1.61) and (1.62), to express the chemical potential of the component i in the condensed phase(s) as a function of its activity, which is a measurable, composition dependent, property of the system

$$\mu_i^{\mathrm{s}} = \mu_i^{\mathrm{v}} = \mu_i^{\mathrm{o,s}} + RT\ln a_i = \mu_i^{\mathrm{o,v}} + RT\ln\frac{p_i}{p_i^{\mathrm{o}}} \tag{1.68}$$

where $\mu_i^{\mathrm{o,s}}$ is the chemical potential of a condensed phase consisting of the pure component i for which the equilibrium partial pressure is p_i^{o}.

It would, therefore, be sufficient to know from experimental measurements or from theoretical analysis the composition dependence of the vapour pressures of the components of a solution to get the values of their chemical potentials and activities in the condensed phase and to draw the corresponding Gibbs free energy curves as a function of the composition.

Because the partial pressure p_i of a solute i in a solution is proportional to its concentration x_i (with the linear Raoult's or Henry's law holding strictly for ideal or ideally diluted liquid solutions), we might also write

$$p_i = \gamma(x)x_i p_i^{\mathrm{o}} \tag{1.69}$$

thus finding a direct relationship between the chemical potential and the concentration x_i of the i-solute

$$\mu_i = \mu_i^{\mathrm{o}} + RT\ln\gamma(x)x_i \tag{1.70}$$

where $\gamma(x)$ is a composition dependent activity coefficient. Ideal solutions are those for which $\gamma(x) = 1$ for each component of the solution.

We can apply the same procedure for the equilibrium conditions relative to the ith component between two generic condensed phases α and β, which may be written

$$\mu_i^{\mathrm{o},\alpha} + RT\ln\gamma_i^{\alpha}(x)x_i^{\alpha} = \mu_i^{\mathrm{o},\beta} + RT\ln\gamma_i^{\beta}(x)x_i^{\beta} \tag{1.71}$$

1.6 Thermodynamic Modelling of Binary Phase Diagrams

1.6.1 Introductory Remarks

The availability of phase diagrams is not only the prerequisite for carrying out materials research in the field of crystal growth, solid state reactions, phase transformations and dry corrosion processes, but phase diagrams are also by themselves a thermodynamics-based powerful tool for material design and optimization processes.

While a very large number of binary and some ternary systems, these last often limited to narrow composition regions, have been experimentally investigated, the experimental approach is almost impossible for most ternary and multicomponent systems.

The real challenge has been to develop phenomenological models, using as an example the Calphad route, to calculate phase diagrams of interest for technological developments [58]. Concerning binary and pseudo-binary systems, these have not only been the subject of experimental studies but also, and for about a century, the subject of thermodynamic modelling studies based on various solution theories, with the aim of finding formal, but predictive, correlations between the energetics of the bonding interactions in solution and the phase diagram topology.

The first, successful, approach was carried out in the framework of the ideal or regular solutions approximations [59, 60], which would require only the preliminary availability of the thermodynamic functions of the pure components, their structural and electronic properties and the energetics of their mutual interactions in solution.

This approach was demonstrated to be useful in a significant number of cases, especially (but not always, as will be shown in the next section) for liquid solutions, but rarely in the case of solid semiconductor systems, for which the assumption of a rigid lattice and the absence of elastic constraints often leads to conclusions which are contradicted by experience [61].

When elastic constraints were first accounted for, severe approximations were used for the calculation of the elastic energy contributions and the interplay between elastic and chemical ordering energies was often underestimated, making it impossible to reconcile, for example, order–disorder transitions with thermodynamic data [61]. To overcome these difficulties, a *first principle statistical mechanics* approach has been applied to study the phase diagrams of a number of tetrahedral, FCC pseudo-binary semiconductors [34], such as the arsenides, phosphides and tellurides.

The QCA has been instead used [33] to compute the partition functions of several binary alloys and then the chemical potentials of the species involved. Once the chemical potentials are known, all the thermodynamic functions are easily obtained. With the QCA, the system under study is considered equivalent to a grand ensemble of statistically independent, few-atom clusters, in equilibrium with the solution, which behaves as a reservoir. In FCC lattices the typical configuration of the clusters is the tetrahedral one.

The QCA is based on the quasi-chemical model, originally applied to metal solutions and to ionic salts, where only pair-like interactions are assumed to be relevant for the properties of a solution and pairs are distributed randomly [60].

It is not the aim of this section to go deeply into the formal aspects of these theories, considering the vast literature available on the subject and the vast number of applications [32, 59, 60, 62–64], but rather to discuss the physico-chemical background of these thermodynamical models and to report the results of their application to semiconductor alloys of technological interest. The intelligent manipulation of conditions of total or incomplete miscibility, order–disorder transitions, the stress effect on phase stabilities, plays a particularly important role in the application and modelling of crystal growth, doping and refining processes, as will be seen in Chapter 4 and also in the next section.

1.6.2 Thermodynamic Modelling of Complete and Incomplete Miscibility

The equilibrium distribution of components among coexisting phases as a function of the temperature and composition and the topological aspects of the phase diagrams, commonly reported in temperature–composition (T, x) coordinates, are the expected output of these modelling studies.

It should be noted here that in a vast number of semiconductor systems decomposition may occur if the pressure of the environment is not taken into proper account. In these cases the phase diagrams are reported in T, x, P diagrams or in their T, x projections.

The equilibrium distribution of a component i among two coexisting phases, of which one is liquid and the other is solid, could be, however, given also in terms of its *distribution* or *segregation coefficient* $k_i(x, T)$, defined as the ratio $k = \frac{x_i^{\mathrm{s}}}{x_i^{\mathrm{l}}}$ where x_i^{s} is the equilibrium atomic fraction of i in the solid phase and x_i^{l} is the equilibrium atomic fraction of i in the liquid phase.

Segregation coefficients may be experimentally determined using appropriate analytical techniques, but the need for knowledge about equilibrium segregation of impurities in semiconductors is essential, as will be seen in Chapter 4, because it allows a proper handling of semiconductor doping and semiconductor refining processes.

It is important, therefore, to show the relationships occurring between the segregation coefficient and the thermodynamic properties of the biphasic system where the repartition of a solution component occurs, in order to understand the physico-chemical grounds.

Using Eq. (1.71) it is possible to write the following general equation for the segregation coefficient

$$\ln k = \ln\frac{x_i^{\mathrm{s}}}{x_i^{\mathrm{l}}} = -\frac{\mu_i^{\mathrm{o,s}} - \mu_i^{\mathrm{o,l}}}{RT} - \ln\frac{\gamma_i^{\mathrm{s}}}{\gamma_i^{\mathrm{l}}} = -\frac{\Delta G_i^{\mathrm{o,f}}}{RT} - \ln\frac{\gamma_i^{\mathrm{s}}}{\gamma_i^{\mathrm{i}}} = \frac{\Delta S_i^{\mathrm{o,f}}}{R} - \frac{\Delta H^{\mathrm{o.f}}}{RT} - ln\frac{\gamma_i^{\mathrm{s}}}{\gamma_i^{\mathrm{l}}} \tag{1.72}$$

which formulates the case of the equilibrium distribution of a generic solute i among two coexisting solid and liquid phases as a function of the chemical potentials of the pure solute i and the activity coefficients of i in the solid and liquid state, over the whole range of temperatures where the two phases coexist. The ratio $\frac{\gamma_i^{\mathrm{s}}}{\gamma_i^{\mathrm{l}}}$ is a solution mixing term, whose value depends on the specific interaction of i with the solvent in the liquid and solid phases, as will be seen later in this section, and, thus, on the temperature and the composition of the solution.

The difference $\mu_i^{\mathrm{o,s}} - \mu_i^{\mathrm{o,l}}$, in turn, is the Gibbs free energy of transformation (i.e. the Gibbs free energy of melting $\Delta G_i^{\mathrm{o,f}} = \Delta H_i^{\mathrm{o,f}} - T\Delta S_i^{\mathrm{o,f}}$ of the pure component i at the melting temperature T_i^{f}, which takes positive or negative values depending on whether $T < T_i^{\mathrm{f}}, T > T_i^{\mathrm{f}}$.

The segregation coefficient is 1, and $x_i^{\mathrm{s}} = x_i^{\mathrm{l}}$ when the following relationship holds for the activity coefficients and the Gibbs free energy of melting, in the case of a solid/liquid equilibrium

$$\ln\frac{\gamma_i^{\mathrm{s}}}{\gamma_i^{\mathrm{l}}} = -\frac{\Delta G_i^{\mathrm{o,f}}}{RT} = \frac{\Delta S_i^{\mathrm{o,f}}}{R} - \frac{\Delta H_i^{\mathrm{o,f}}}{RT} \tag{1.73}$$

We will see in Section 1.7.8 a particular case of this conditions which is presented by the nanocrystalline Si-Ge alloys, for which $k \sim 1$ from pure Ge to pure Si. The physical sense of this condition is that for $\Delta G_i^{\mathrm{o,f}} \to 0$ and $\frac{\gamma_i^{\mathrm{s}}}{\gamma_i^{\mathrm{l}}} = 1$, a distinction between the solid and liquid phase is thermodynamically impossible.

The segregation coefficient is also unitary for the segregation of i at the melting point T_i^{f} of i, because in this condition the free energy of fusion $\Delta G_i^{\mathrm{o,f}} = 0$ and $\mu_{\mathrm{A}}^{\mathrm{o,s}} = \mu_{\mathrm{A}}^{\mathrm{o,l}}$

For the equilibrium of i among a couple of ideal solutions, for which, by definition, $\gamma_{\mathrm{i}}(\mathrm{s}) = 1$ and $\gamma_i(\mathrm{l}) = 1$, the segregation coefficient is instead given by the equation

$$\ln k_i = \ln\frac{x_i^{\mathrm{s}}}{x_i^{\mathrm{l}}} = -\frac{\Delta G_i^{\mathrm{f}}}{RT} \tag{1.74}$$

where $\Delta G_i^{\mathrm{o,f}}$ is again the Gibbs free energy of fusion of the pure component i.

Except for these particular cases, the equilibrium distribution of a generic component i among two condensed phases or a condensed phase and a gaseous or vapour phase, given by Eq. (1.72), depends on the specific thermodynamic properties of the coexisting solutions, which should be experimentally available or theoretically determined.

A systematically practised solution to arrive at the theoretical evaluation of a phase diagram is modelling the temperature, composition and pressure dependence of the Gibbs free energy $G(T, P, x)$ functions of the coexisting liquid and solid solutions and of the potentially stable intermediate compounds. In the case of binary or pseudo-binary solutions, this corresponds to the evaluation of the features of the hypersurfaces $G(T, p, x)$, or, in isobaric conditions, those of the surfaces $G(T, x)$ or of their isothermal sections $G(x)$, associated with the solid and liquid phases of the system under consideration, assuming, at a first approximation, that both the liquid and the solid phases are in internal mechanical equilibrium.

Let us first consider the simplest case of two elemental components A and B with very close physical, chemical and structural properties, that is very close values of the lattice constants, atomic radii and electronic properties in both the solid and liquid state. Such features hypothetically grant conditions of mutual solubility in all proportions in the liquid and solid state and, furthermore, of *ideal behaviour* of both the liquid and solid solutions. In this case, the thermodynamic activities of the components coincide with their atomic fractions, that is $a_i = x_i$.

The molar Gibbs free energy of both the liquid and solid solution is, therefore, given by the equation

$$G_{\mathrm{soln}} = x_{\mathrm{A}}\mu_A + x_{\mathrm{B}}\mu_{\mathrm{B}} = x_{\mathrm{A}}\mu_{\mathrm{A}}^{\mathrm{o}} + x_{\mathrm{B}}\mu_B^o + RT(x_{\mathrm{A}}\ln x_{\mathrm{A}} + x_{\mathrm{B}}\ln x_{\mathrm{B}}) \tag{1.75}$$

and the excess Gibbs free energy of mixing $\Delta G_{\mathrm{mix}} = \Delta H_{\mathrm{mix}} - T\Delta S_{\mathrm{mix}}$ is given by

$$\Delta G_{\mathrm{mix}} = G_{\mathrm{soln}} - (x_{\mathrm{A}}\mu_{\mathrm{A}}^{\mathrm{o}} + x_{\mathrm{B}}\mu_{\mathrm{B}}^{\mathrm{o}}) = RT\ [x_{\mathrm{A}}\ln x_{\mathrm{A}} + x_{\mathrm{B}}\ln x_{\mathrm{B}}] \tag{1.76}$$

Therefore, the Gibbs free energy of mixing has only a purely configurational entropy character and $\Delta H_{\mathrm{mix}} = 0$

The assumption about a purely configurational entropy character of the Gibbs free energy of mixing can be easily demonstrated, starting from the use of the Boltzmann equation

$$S = k\ln W \tag{1.77}$$

where k is the Boltzmann constant and W is the total number of possible random configurations of a system consisting of N_{A} atoms of A and N_{B} atoms of B

$$W = \frac{(N_{\mathrm{A}} + N_{\mathrm{B}})!}{N_{\mathrm{A}}!N_{\mathrm{B}}!} = \frac{N!}{N_{\mathrm{A}}!N_{\mathrm{B}}!} \tag{1.78}$$

and $N_{\mathrm{A}} + N_{\mathrm{B}} = N$. Then one can see, using the Stirling approximation, that a pure configurational entropy term is given by the following equation

$$\Delta S = Nk(x_{\mathrm{A}}\ln x_{\mathrm{A}} + x_{\mathrm{B}}\ln x_{\mathrm{B}}) = R(x_{\mathrm{A}}\ln x_{\mathrm{A}} + x_{\mathrm{B}}\ln x_{\mathrm{B}}) \tag{1.79}$$

For solutions displaying significant deviations from ideality, the activities $a = \gamma x$ should be used instead of the concentrations in Eq. (1.76), and the excess Gibbs free energy of mixing is then given by

$$\Delta G_{\mathrm{mix}} = -RT(x_{\mathrm{A}}\ln\gamma_{\mathrm{A}}x_{\mathrm{A}} + x_{\mathrm{B}}\ln\gamma_{\mathrm{B}}x_{\mathrm{B}}) \tag{1.80}$$

In this case is possible to preliminarily apply the so-called regular model, originally proposed by van Laar [65, 66], Hildebrand [67], Fowler and Guggenheim [68] and Guggenheim [69], where the excess Gibbs free energy of a regular solution is ruled by pair-like interactions between neighbour atoms in solution and is given by the following general equation

$$\Delta G_{\mathrm{mix}}(x, T) = x_{\mathrm{A}}x_{\mathrm{B}}\Omega - TS_{\mathrm{conf}} - x_{\mathrm{A}}x_{\mathrm{B}}\eta T \tag{1.81}$$

where $\Omega = ZN\left[H_{\mathrm{AB}} - \left(\frac{H_{\mathrm{AA}}+H_{\mathrm{BB}}}{2}\right)\right]$ is an interaction coefficient, taken as the difference between the pair-binding enthalpy of unlike species in solution and the average of the binding enthalpies of like pairs and ZN is the product of the coordination number Z and the total number N of atoms. Here the term $x_{\mathrm{A}}x_{\mathrm{B}}\ \Omega$ is the enthalpy of mixing ΔH_{mix}, now different from zero and $x_{\mathrm{A}}x_{\mathrm{B}}\ \eta$ is a non-configurational entropy term.

The model indirectly assumes the absence of internal elastic energy contribution to the enthalpy of mixing, arising from different atomic volumes or lattice mismatch of the components, as well as a random distribution of components atoms in a rigid lattice.

The excess Gibbs free energy of mixing, with respect to that of an ideal solution, is given by the equation

$$\Delta G^{*}_{\text{mix}}(x,T) = x_\text{A}x_\text{B}\varOmega - x_\text{A}x_\text{B}\eta = x_\text{A}x_\text{B}(\varOmega - \eta T) \tag{1.82}$$

The composition dependence of the solution enthalpy term $\Delta H_\text{mix} = x_\text{A}x_\text{B}\ \varOmega$ of Eqs. (1.81) and (1.82) may be understood by noting first that the enthalpy of solution H_soln is given by the following sum

$$H_\text{soln} = P_\text{AA}H_\text{AA} + P_\text{BB}H_\text{BB} + P_\text{AB}H_\text{AB} \tag{1.83}$$

where P_XX is the number of XX pairs in solution and H_XX is their binding energy. The evaluation of the P_XX terms is straightforward for systems where each X atom has the same number Z of neighbours, as would be the case for Si and Ge, where $Z = 4$.

In the case of a solution of A and B species, with a total number N_A of atoms A and N_B of atoms B

$$N_\text{A} = \frac{P_\text{AB}}{Z} + 2\frac{P_\text{AA}}{Z} \tag{1.84}$$

$$N_\text{B} = \frac{P_\text{AB}}{Z} + 2\frac{P_\text{BB}}{Z} \tag{1.85}$$

$$P_\text{AA} = \left(N_\text{A} - \frac{P_\text{AB}}{Z}\right)\frac{Z}{2} \tag{1.86}$$

$$P_\text{BB} = \left(N_\text{B} - \frac{P_\text{AB}}{Z}\right)\frac{Z}{2} \tag{1.87}$$

$$\begin{aligned} H_\text{soln} &= H_\text{AA}\left(N_\text{A} - \frac{P_\text{AB}}{Z}\right)\frac{Z}{2} + H_\text{BB}\left(N_\text{B} - \frac{P_\text{AB}}{Z}\right)\frac{Z}{2} + H_\text{AB}P_\text{AB} \\ &= \frac{ZN_\text{A}H_\text{AA}}{2} - H_\text{AA}\frac{P_\text{AB}}{2} + \frac{ZH_\text{BB}H_\text{BB}}{2} - \frac{H_\text{BB}P_\text{AB}}{2} + H_\text{AB}P_\text{AB} \\ &= \frac{Z}{2}N_\text{A}H_\text{AA} + \frac{Z}{2}N_\text{B}H_\text{BB} + P_\text{AB}\left(H_\text{AB} - \frac{1}{2}\left(H_\text{AA} + H_\text{BB}\right)\right) \end{aligned} \tag{1.88}$$

$$\Delta H_\text{mix} = H - \frac{Z}{2}N_\text{A}H_\text{AA}\frac{Z}{2}N_\text{B}H_\text{BB} = H - H^\text{o}_\text{A} - H^\text{o}_\text{B} = P_\text{AB}\left(H_\text{AB} - \frac{1}{2}\left(H_\text{AA} + H_\text{BB}\right)\right) \tag{1.89}$$

As the total number of pairs is $\frac{1}{2}\ ZN$, the number of AB pairs $P_\text{AB} = \frac{N_\text{A}}{N}\frac{N_\text{B}}{N}ZN = x_\text{A}x_\text{B}ZN$ and

$$\Delta H_\text{mix} = x_\text{A}x_\text{B}ZN\left(H_\text{AB} - \frac{H_\text{AA} + H_\text{BB}}{2}\right) = x_\text{A}x_\text{B}\varOmega \tag{1.90}$$

To account for the non-configurational entropy term, the vibrational and electronic contributions should be known or calculated with a quantum mechanical approach [70]. It is common practice, however, when accounting for the properties of a regular solution, to neglect the non-configurational entropy term and consider for the Gibbs free energy of the solution and the excess Gibbs free energy of mixing the sole enthalpic term

$$G_\text{soln}(x,T) = x_\text{A}x_\text{B}\varOmega - TS_\text{conf} \tag{1.91}$$

$$\Delta G_\text{mix} = \Delta H_\text{mix} = x_\text{A}x_\text{B}\varOmega \tag{1.92}$$

Table 1.5 *Domains for invariant transformations in binary systems*

Liquid	$\Omega > 0$	$\Omega < 0$	$\Omega > 0$	$\Omega < 0$	$\Omega = 0$	$\Omega = 0$	$\Omega > 0$	$\Omega < 0$
Solid	$\Omega > 0$	$\Omega < 0$	$\Omega < 0$	$\Omega > 0$	$\Omega > 0$	$\Omega < 0$	$\Omega = 0$	$\Omega = 0$

Sarma *et al.*, 2003, [32]. Reproduced with permission from Springer Science and Business Media.

It should be noted that the interaction coefficient Ω is assumed here to be temperature independent, but it will be shown in the next section that the modelling of compound semiconductor alloys often requires the use of temperature-dependent interaction coefficients.

It will also be shown that a mixing enthalpy term with a quadratic composition dependence might be foreseen in the case of II–VI compound semiconductor alloys (see Section 1.7.10) where misfit lattice strain dominates the interaction, although within the limit of validity of Hooke's law.

As only the solid solution or only the liquid solution or both might be regular, and for both positive and negative Ω values, the modelling of systems with Ω values different from zero requires a solution for all the eight domains shown in Table 1.5 [32].

The shape of the free energy curves depends strongly on the absolute value of the $x_A x_B\ \Omega$ term. Positive values of this term will balance the configurational entropy contribution (see Eq. (1.91)) at low temperatures, with the onset of miscibility gaps in the temperature range of solid solutions. For very large positive values of Ω^{α} the formation of an ordered α' phase might be foreseen. Negative values of the $x_A x_B\ \Omega$ term, corresponding to large bonding energy of unlike atoms, add to the entropy term, thus increasing the stability of the solid solution.

If the thermodynamics of a regular solution are dominated only by the enthalpic term $\Delta H_m = x_A x_B \Omega$ (i.e. the non-configurational entropy terms are negligible), it is easy to get the values of the activity coefficients of the components in solution and thus to evaluate the chemical potentials from the experimental or calculated values of ΔH_{mix}.

In fact, from Eq. (1.80)

$$\frac{\delta \Delta G_{mix}}{\delta x_B} = RT \ln \gamma_B \tag{1.93}$$

and Eq. (1.92) using the Gibbs-Duhem relationship [7] we obtain

$$\frac{\partial \Delta G_{mix}}{\partial x_B} = \frac{\partial \Delta H_{mix}}{\partial x_B} = (1 - x_B)^2 \Omega \tag{1.94}$$

from which the equations for the activity coefficients can be obtained

$$\ln \gamma_B = \frac{(1 - x_B)^2\ \Omega}{RT} \tag{1.95}$$

and

$$\ln \gamma_A = \frac{x_B^2\ \Omega}{RT} \tag{1.96}$$

and the chemical potentials

$$\mu_A(x, T) = \mu_A^o + x_B^2 \Omega + RT \ln x_A \tag{1.97}$$

$$\mu_B(x, T) = \mu_B^o + (1 - x_B)^2 \Omega + RT \ln x_B \tag{1.98}$$

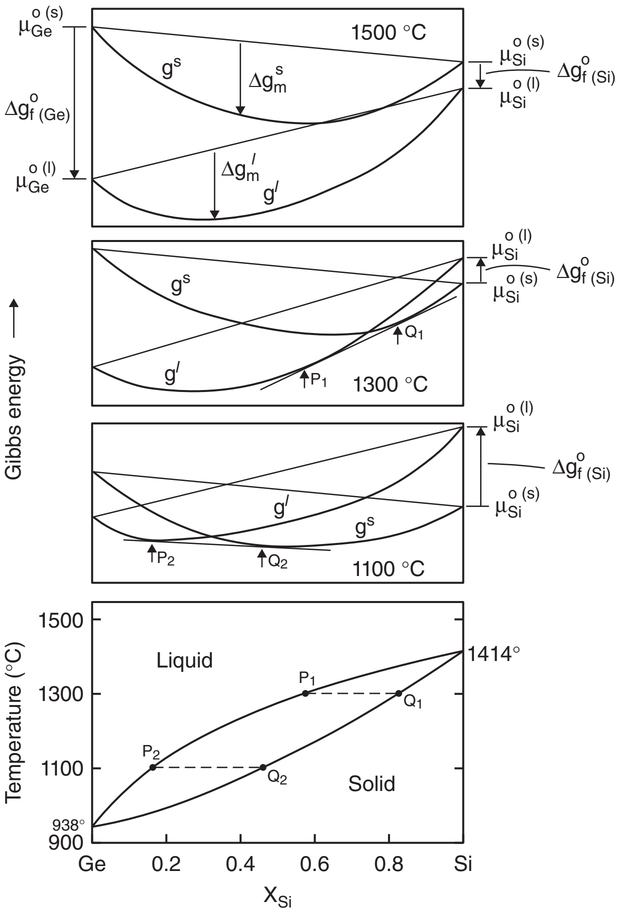

Figure 1.14 *Modelling of the isomorphous phase diagram of the Ge-Si system. Pelton, 2001, [71]. Reproduced with permisssion from John Wiley & Sons*

Conversely, these equations may be used to calculate the interaction coefficient Ω from the experimental values of the activities or the chemical potentials, determined by suitable thermochemical or electromotive force (EMF) measurements on electrochemical cells (see Appendix).

A classical example of the application of thermodynamic modelling to a semiconductor system is that reported in Figure 1.14 for the Ge-Si alloys, which was proposed by Pelton [71] under the assumption that both the solid and liquid solutions are ideal ($\Omega^s = \Omega^l = 0$).

The $G(x)$ isotherms, calculated according to Eq. (1.48), are displayed in a ΔG versus x graph, where the difference between the Gibbs free energy of the pure component Ge and Si in the liquid and solid state, at any temperature between the melting temperatures of Ge and Si, is given by their Gibbs free energy of fusion ${}^{e}\Delta G_{\mathrm{f}}^{\mathrm{oGe}} = \mu^{\mathrm{o}}\mathrm{Ge(l)} - \mu^{\mathrm{o}}\mathrm{Ge(s)}$ and $\Delta G_f^{oSi}\Delta G_{\mathrm{f}}^{\mathrm{oSi}} = \mu^{\mathrm{o}}\mathrm{Si(l)} - \mu^{\mathrm{o}}\mathrm{Si(s)}$, respectively.

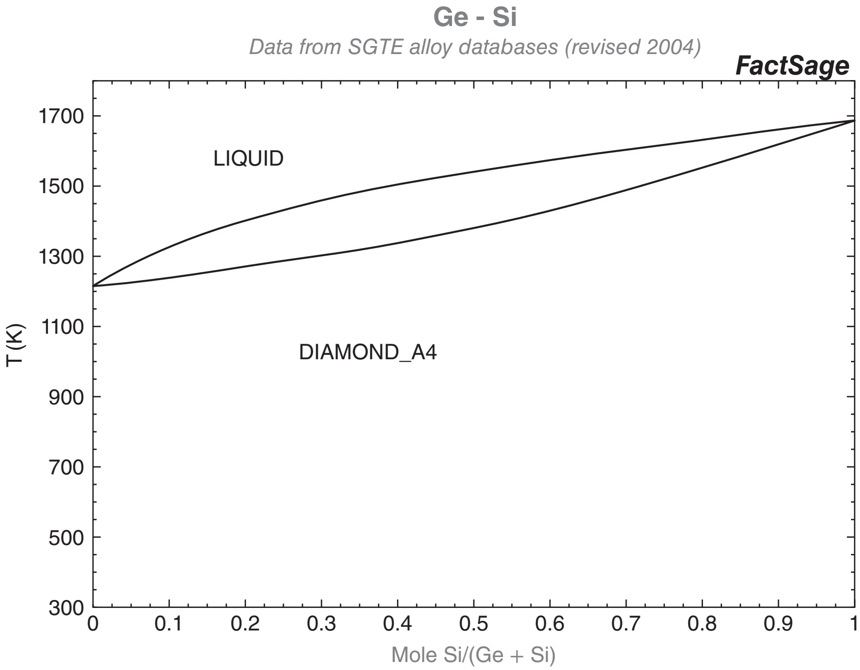

Figure 1.15 *Experimental phase diagram of the binary Ge-Si system. Scientific Group Thermodata Europe (SGTE). Reproduced with permission from SGTE*

As the free energy of fusion of the pure components Ge or Si[7] can be written

$$\Delta G_{\mathrm{f}}^{\mathrm{o}} = \Delta H_{\mathrm{f}}^{\mathrm{o}} - T\Delta S_{\mathrm{f}}^{\mathrm{o}} \tag{1.99}$$

so far the enthalpy and the entropy of fusion remain independent of the temperature (which is the actual case, considering the relatively narrow difference between the melting temperature of Ge and Si), the Gibbs energy of fusion is linearly dependent on the temperature and takes negative values for $T > T_{\mathrm{f}}$ and positive values for $T > T_{\mathrm{f}}$, as indicated by the vertical arrows in Figure 1.14.

Then, from the $G(x)$ isotherms at 1100 and 1300 °C, the equilibrium composition of the coexisting phases at these temperatures can be obtained, given by the intercepts of the common tangents at the points P_1 and Q_1 and P_2 and Q_2. Using this procedure for a sufficient number of temperatures, the isomorphous, lens-shaped, phase diagram at the bottom of Figure 1.14 may be obtained, which compares well with the experimental one displayed in Figure 1.15.

Using the regular solution model, van Laar [65, 66] demonstrated that many of the observed types of simple phase diagrams could be obtained by a systematic variation of the Ω values (Ω^{β} and Ω^{α} for liquid and solid phases, respectively, in the positive domain ($\Omega > 0$) with $\Omega^{\beta} \leq \Omega^{\alpha}$.

---

[7] See Ref. [72] for the actual values of free energy of fusion.

By varying Ω^{α} from zero to very large positive values (keeping the liquid solution as ideal with $\Omega^{\beta} = 0$), it was possible to obtain lens-shaped isomorphous, simple eutectic, peritectic and isomorphous with congruent maximum or minimum diagrams.

A few examples of the procedure which should be used are displayed in Figures 1.16–1.18 [73].

Figure 1.16a refers to the case of two pure components A and B crystallizing with different structures, α and β. For this system it is supposed that the liquid solution is ideal and that two different regular solid solutions, one with the structure of the α phase and the other with the structure of the β phase, are thermodynamically stable, both with Ω values <0, over the entire range of composition.

The relative Gibbs energy curves are calculated for a number of temperatures, ranging from values above the melting temperatures of both components down to low temperature.

Using for the evaluation of the phase equilibria the common tangent procedure (dotted curves in the three panels), the shape of a eutectic-type of phase diagram may be obtained, with a wide miscibility gap.

The case of Figure 1.16b is that of a system of two components A and B crystallizing with the same α structure. For this system it is supposed that the liquid solution is again ideal and that the solid solution of A and B is regular, with Ω values $\gg 0$. Consequently, the Gibbs energy curves present two nodes and a positive maximum due to the interplay of the configurational entropy contribution $T\Delta S = RT(x_A \ln x_A + x_B \ln x_B)$, which decreases with decrease in temperature, and the mixing enthalpy $\Delta H_{mix} = x_A x_B \Omega$ term. Also in this case a eutectic type of diagram could be obtained using the same geometrical procedure adopted in Figure 1.16a. It is supposed that the A-rich α_1 phase and the B-rich α_2 phase have close structural relationships with the phase α.

The origin of a solubility gap, with the consequent two phase decomposition processes of the homogeneous solid solution is instead illustrated in Figure 1.17 for the case of an isomorphous system with a congruent minimum. Here, slightly positive $x_A x_B \Omega^s$ terms dominate the shape of the Gibbs energy curves at very low temperatures, when the configuration entropy term contribution $T\Delta S = RT(x_A \ln x_A + x_B \ln x_B)$ begins to be small or negligible.

Some key features of the phase decomposition processes will be discussed in Section 1.6.4 for their crucial role in the epitaxial growth from the vapour phase of several compound semiconductors at temperatures or compositions close to or within the miscibility gap.

The formation of a low-temperature, ordered phase is eventually shown in Figure 1.18, which occurs in the case of a system where the thermodynamics of the solid solution are ruled by negative values of Ω^s, and a phase with a composition centred at $x_A = 0.5$ becomes stable at low temperature.

To complete the analysis, Figure 1.19 shows the variety of phase diagrams that can be obtained by progressive changes of the interaction coefficients of the solid Ω^S and of the liquid solution Ω^1 from negative to positive values.

These results confirm the ability of the regular solution model in forecasting the structure of the most common phase diagrams as a sole function of the interaction parameters Ω for the liquid and solid solutions. It is also shown that minute changes, around $10\,\mathrm{kJ\,mol^{-1}}$ of the interaction parameter Ω, have a significant impact on the mutual solubility relationships.

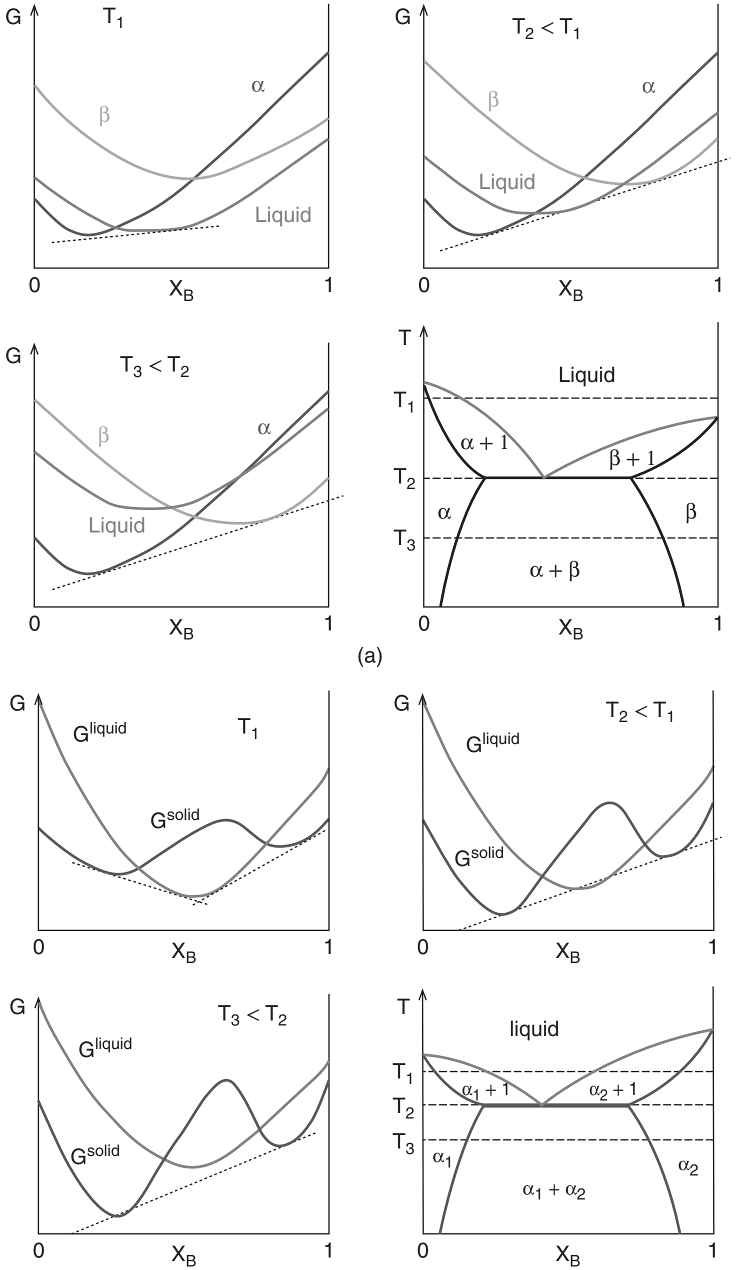

(a)

(b)

Figure 1.16 *Modelling of (a) a eutectic type of phase diagram for the case of a solution of pure components having different structures and regular solution interaction coefficients* $\Omega^{s} < 0, \Omega^{l} = 0$*; (b) a eutectic type of phase diagram for the case of a solution of pure components having equal structures and regular solution interaction coefficients* $\Omega^{s} \gg 0, \Omega^{l} = 0$. *Courtesy of L. Zhigilei*

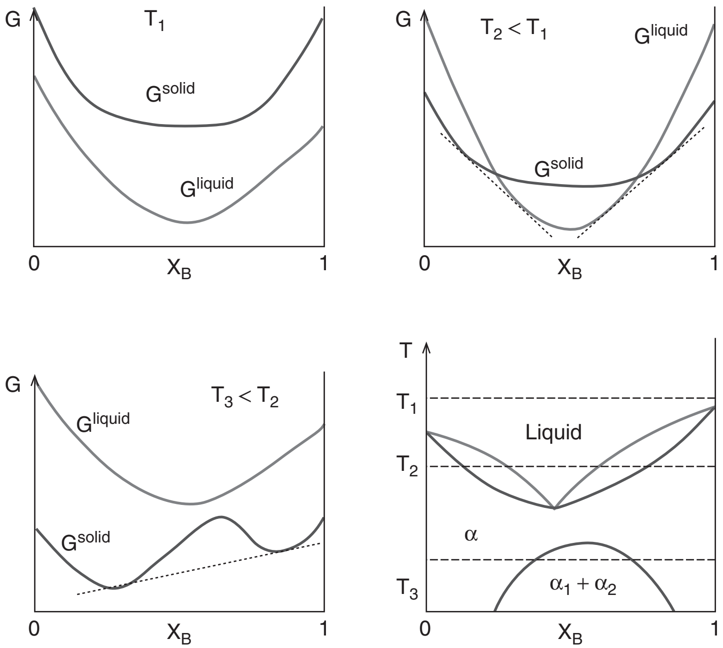

Figure 1.17 *Modelling of an isomorphous diagram with congruent minimum $\Omega^s > 0, \Omega^l = 0$. Courtesy of L. Zhigilei*

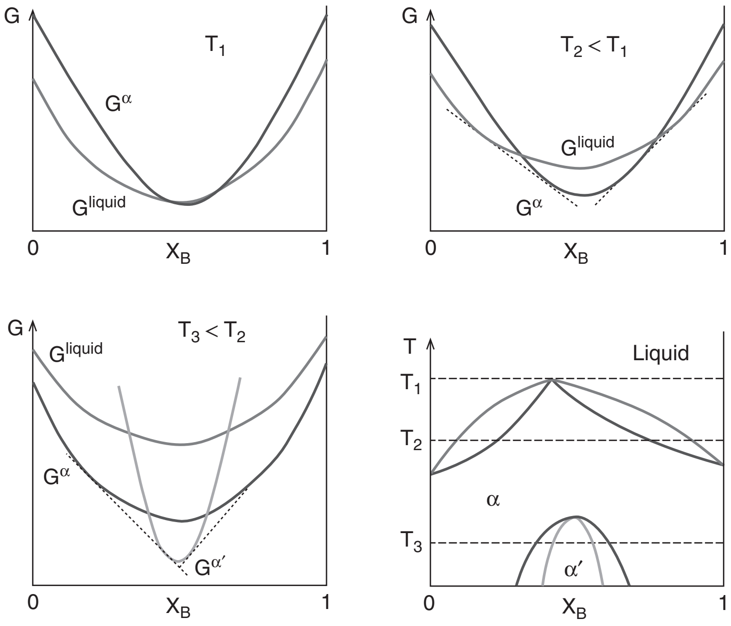

Figure 1.18 *Modelling of the phase diagram of an isomorphous system with congruent maximum in the presence of a low temperature ordered, α′ phase region. $\Omega^s < 0, \Omega^l = 0$. Courtesy of L. Zhigilei*

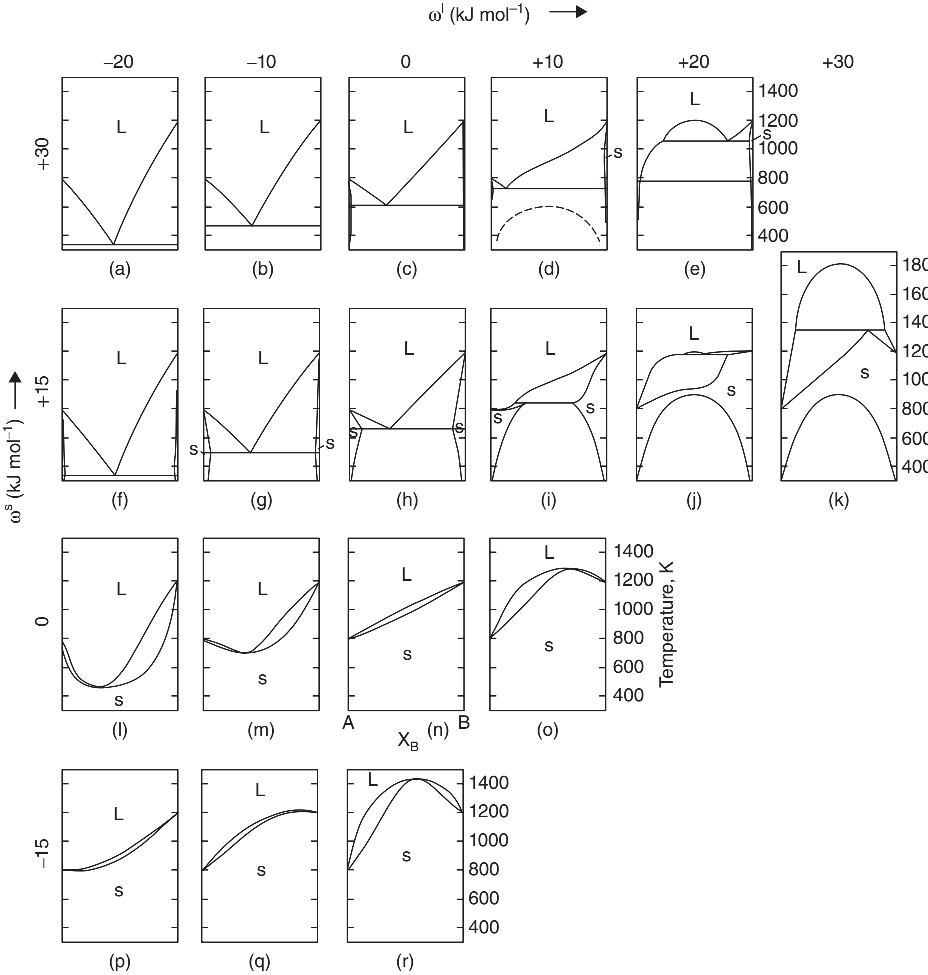

Figure 1.19 *Influence of the interaction parameters Ω^s and Ω^l on the morphology of phase diagrams. Pelton, 2001, [71]. Reproduced with permission from John Wiley & Sons*

In the last 30 years, among others, Pelton [71], Pelton and Thompson [74], Oonk [75], DeHoff [76] and Chang and Chen [77] demonstrated the occurrence of several other types of simple binary phase diagrams for different combinations of regular solution parameters, while Sarma *et al.* [32] extended the analysis to most of the possible alternatives.

These last authors confirmed, as an example, that isomorphous-type of phase diagrams ruled by negative Ω^s values display an ordered region at low temperatures, as experimentally demonstrated in the case of the copper-gold system which will be dealt with in the next section. They showed also that the isomorphous diagrams with a congruent minimum, ruled by positive values of Ω^s, display, instead, a miscibility gap [32].

The predictive ability of the regular solution approximation fails, however, in a large number of cases of binary and pseudo-binary semiconductor systems, where structural misfits and consequent misfit strains play a crucial role in the solution thermodynamics.

The regular solution scheme leaves open a number of conceptual challenges, especially in the case of disordered phases of compound semiconductors of general composition A_nB_m, as it assumes the presence of a fixed coherent AB lattice and the absence of lattice mismatch and ignores the existence of thermodynamically stable atomic arrangements different from neighbour pairs. The assumption of a rigid lattice precludes consideration of the effects of elastic energy contribution, with the consequence of excluding the contemporary condition of phase separation (the opening of a solubility gap) and ordering, as the first condition calls for Ω values >0 and the second for Ω values <0 [61].

We will show in Section 1.7 how the QCA, an advanced version of the regular solution model, and other models, allowing an interplay between chemical and elastic factors, permits computation of the thermodynamic properties of several binary alloys with satisfactory precision.

1.6.3 Thermodynamic Modelling of Intermediate Compound Formation

An important family of binary systems shows the presence of an intermediate compound, as is the case in the diagram of Figure 1.20. It is apparent that this diagram may be empirically discussed as the superposition of two eutectic-type phase diagrams, one having as the components pure Mg and the intermediate compound Mg_2Si, and the other one the compound Mg_2Si and pure Si.

1.6.4 Retrograde Solubility, Retrograde Melting and Spinodal Decomposition

At temperatures above the eutectic temperature, see Figure 1.16a,b, the solubility of the solute is expected to decrease with increasing temperature after having reached its

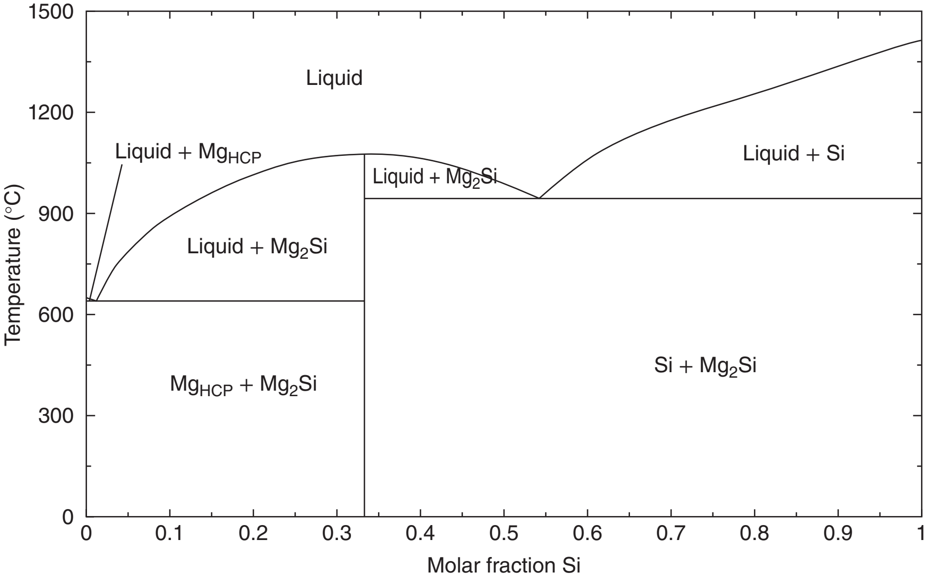

Figure 1.20 *Phase diagram of the Mg-Si system, showing the presence of the intermediate compound* Mg_2Si. *Scientific Group Thermodata Europe (SGTE). Reproduced with permission from SGTE*

maximum value at the eutectic point. In several binary systems, however, the solubility continues to increase at temperatures well above the eutectic temperature until a solubility maximum is reached, as shown schematically in Figure 1.21, for the solubility of an impurity M in Si on the Si-rich corner.

This phenomenon is called retrograde solubility and known to be common to several binary (Transition Metal) TM-Si or TM-Ge systems [78] but also to compound semiconductor systems [79, 80]. An example is given by the Ni-Si system, where the eutectic temperature is 964 °C while the maximum solubility is achieved at 1300 °C [81].

In spite of the vast number of cases where retrograde solubility occurs, this phenomenon has been considered, erroneously, thermodynamically anomalous [82, 83]. Actually [71], the common assumption of a maximum solubility at the eutectic temperature is contradicted by the regular solution theory, see Figure 1.19d, where one can observe that the solubility maximum for the species B lies well above the eutectic temperature for the equilibrium between regular liquid and solid solutions, characterized by very large, positive interaction coefficients ($\Omega^l = +10$; $\Omega^s = +30$).

Therefore, retrograde solubility is not an anomalous phenomenon, but one which should be considered in the case of potential occurrence of relevant interaction processes between solution components and solution components and point defects [80], as will be discussed in Chapter 2.

Retrograde melting is a possible consequence of retrograde solubility and is expected to occur at temperatures above the eutectic, as was recently discussed by Buonassisi *et al.* [30] and successfully confirmed by Hudelson *et al.* [27] with a delicate experimental approach, using μ-XAS.

In fact, if the phase diagram of a Si-M binary system has the shape of Figure 1.21, and a homogenous alloy of composition x_1 at point A is quenched from the temperature T_1 to T_2, the system is brought to thermodynamically unstable conditions in one phase configuration and spontaneously decomposes in two phases, one of which is a liquid of composition x_2. Independently of the thermodynamic aspects of this phenomenon, the formation of liquid droplets of known composition upon cooling a homogeneous semiconductor alloy might be of interest for the engineering of quantum devices, if the droplets size was nanometric.

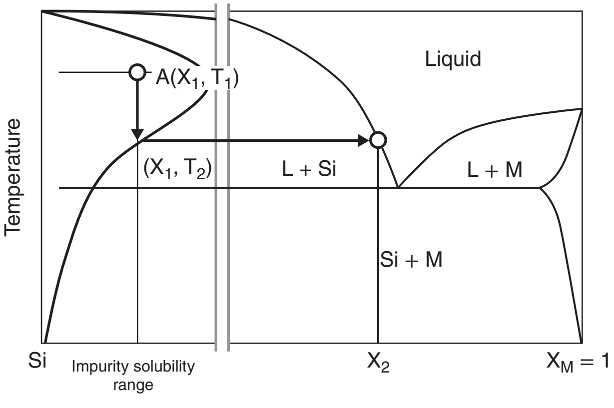

Figure 1.21 *Schematic diagram of a Si-M binary system exhibiting retrograde solubility. Adapted from Hudelson* et al.*, [27], with permission from John Wiley & Sons*

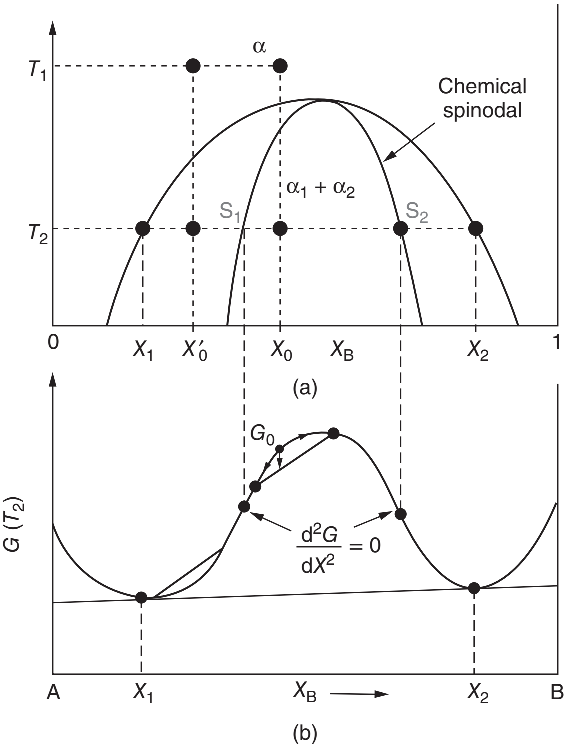

Figure 1.22 *Binodal and spinodal decomposition processes. Porter* et al.*, 2009 [265]. Reproduced with permission from Taylor & Francis*

Spinodal decomposition is another, frequently observed, phenomenon in semiconductor growth and processing, which occurs when a binary system presents a miscibility gap (see Figure 1.22a), its Gibbs free energy curves have the typical shape of Figure 1.22b for any temperature inside the range of existence of the miscibility gap and the process must be operated in the temperature/composition range of the miscibility gap for compelling technological reasons.

If an alloy of composition within X_1 and X_2 is quenched from temperature T_1 to the T_2, the system is brought from its homogeneous α-phase configuration to thermodynamically unstable conditions and the condition, therefore, occurs for its decomposition into two phases α_1 and α_2 of limiting composition X_1 and X_2, given by the common tangent procedure.

The curve drawn using a set of points X_1 and X_2 kept at the nodes of the Gibbs energy curves at different temperatures is the *coexistence* curve and represents the set of the isothermal boundaries of the miscibility gap in a T versus x diagram. Instead, a set of points S_1 and S_2, corresponding to the coordinates of the zeroing of the second derivative $\frac{\delta^2 G}{\delta x^2} = 0$ of the Gibbs free energy defines the shape of the *spinodal* curve, represented in Figure 1.22a.

Where the two branches of the coexistence and spinodal curve meet, one finds the critical point above which the system is thermodynamically stable in the homogeneous α-phase configuration.

Inside the miscibility gap the phase separation process $\alpha \rightarrow \alpha_1 + \alpha_2$ should occur spontaneously as it implies a Gibbs free energy variation $\Delta G < 0$, but it requires a suitable (thermal) activation in order to occur at a reasonable rate.[8] Under the assumption that the α_1 phase has the same, or a very close, structure as the original homogeneous α phase, the hypothesis should be made that the decomposition process may be either heterogeneous or homogeneous. Heterogeneous unmixing occurs by a nucleation process of the α_2 phase at suitable heterogeneous nucleation sites, which could be GBs, dislocations or point defect complexes.

Homogeneous phase decomposition is supposed, instead, to be initiated, in the absence of heterogeneous nuclei, by two different mechanisms, corresponding to two types of statistical concentration fluctuations, the heterophase- or the homophase-local fluctuation. The concentration width of these fluctuations is between the spinodal and the coexistence curves for the heterophase mechanism, which occurs when the concentration of the precursor phase is X_o, that is for a system only slightly supersaturated and requires overcoming a nucleation barrier typically larger than 5 kT (>0.5 eV at 1000 K) [84]. This process may be treated as a homogeneous nucleation and growth mechanism, initiated with the formation of a distribution of ordered domains (nuclei) of the α_2 phase, which will then grow to macroscopic size.

The concentration width of these fluctuations is, instead, between the two branches of the spinodal curves for the homophase process, which occurs when the concentration is X_o, deep into the solubility gap. This process is called *spinodal decomposition* and, differently from that initiated by nucleation, involves composition fluctuations in the whole bulk of the material [84, 85]. Both processes are controlled by the same mechanism, the isothermal diffusion of solvent and solute atoms driven by a gradient of the chemical potential, but the consequences, in terms of material quality and properties, are quite different. Spinodal decomposition of metallic alloys has the practical advantage of producing a very disperse microstructure which could improve the mechanical properties of the alloy. In the case of semiconductors, however, it has the drawback of producing local composition inhomogeneities, with consequent electrical and optical inhomogeneities which could be dramatic from the view point of devices. The role of spinodal decomposition in growth processes of compound semiconductors carried out in the region of the solubility gap will be discussed in the next section.

1.7 Solution Thermodynamics and Structural and Physical Properties of Selected Semiconductor Systems

1.7.1 Introductory Remarks

This section deals with the analysis of the thermodynamic properties of several binary and pseudo-binary semiconductor systems of technological interest, with the aim to discuss the relevant correlations between structural, physical, topological and solution thermodynamics aspects.

In this regard, while there is a well-settled empirical knowledge that the solid solubility of an element or of a compound in another one is generally favoured by equal crystal

---

[8] This is the reason why strained layers may survive in a metastable homogeneous single phase configuration.

structures, similar atomic sizes, close lattice parameters and equivalent stable charge states or electronic properties, the macroscopic correlations between thermodynamic behaviour and solution structure present important criticalities.

As an example, contrary to the common belief, complete mixing and ideality in binary or pseudo-binary systems, even belonging to the same crystal system, is not necessarily associated with the fulfillment of Vegard's law [35]

$$a^{o}_{\mathrm{A}_xB_{1-x}} = xa^{o}_{\mathrm{A}} + (1-x)a^{o}_{\mathrm{B}} \tag{1.11}$$

which was discussed in Section 1.3.

A number of binary metallic and non-metallic alloy systems present complete solid state miscibility but important deviations from this law. The possible presence of bimodal distributions of lattice constants, with values intermediate between those of the pure compound and the average Vegard values [70] and of very different distributions of bond distances as a function of the composition, has also been seen, as is the case for the Ge-Si systems which will be discussed later in this section.

The main reason for this behaviour is that the accomplishment of this law is based on the fulfilment of a continuum elasticity model, while the effective physics is fundamentally a problem of quantum mechanics and physical chemistry [86], on *which there already now begins to exist a sound theoretical background.*

Deeper information on structural relationships could be obtained using the EXAFS technique, which is particularly powerful for the determination of the distance between selected atomic pairs. It was, in fact, demonstrated to be capable of giving supplementary information on the evolution of the nearest neighbour distances for both ionic solutions (such as the pseudo-binaries $\mathrm{K}_{1-x}\mathrm{Rb}_x\mathrm{Br}$, $\mathrm{RbBr}_{1-x}\ \mathrm{I}_x$, $\mathrm{KCI}_{1-x}\mathrm{Br}_x$ compounds) and semiconducting alloys (such as $\mathrm{In}_{1-x}\mathrm{Ga}_x\mathrm{As}$, $\mathrm{GaAs}_{1-x}\mathrm{P}_x$ and $\mathrm{Si}_{1-x}\mathrm{Ge}_x$), as will be seen later.

As an example, the configurationally averaged lattice parameters versus composition for mixed nitrides ($\mathrm{In}_x\mathrm{Ga}_{1-x}\mathrm{N}$ and $\mathrm{Al}_x\mathrm{Ga}_{1-x}\mathrm{N}$) have been calculated using total energy minimization procedures, showing that they fulfil Vegard's law. Instead, for the experimental bond lengths measured using EXAFS measurements as a function of the composition, Vegard's law fails [64, 87, 88].

Furthermore [86], the size effects have often been studied from an idealized point of view and the limited success of the continuum elasticity model depends on the fact that the electronic interactions between the outermost quantum shells of the solute and solvent atoms are too complex to be only accounted for by a simple size effect.

By using an elasticity inclusion model Lubarda [86] calculated the apparent size of the solute atoms for a number of binary systems and carried out a comparison with the experimental data of selected systems, with a modest general success, which emphasizes the need to apply non-linear elasticity theories and *ab initio* methodologies.

More recently, Jacob *et al.* [89] showed with pure solution thermodynamics arguments that the conformity with Vegard's law is not an indication of ideal solution behaviour. For non-ideal solutions it is shown that positive Ω values increase the positive deviations from Vegard's law and that for very negative values of Ω the positive deviations of the law caused by lattice mismatch may be compensated by the large effect associated with the solute–solvent interaction. The conclusion is that Vegard's law, due to the absence of a sound theoretical background, might be downgraded to a simple approximation, at least until deeper experimental evidence becomes available.

1.7.2 Au-Ag and Au-Cu Alloys

To analyse the descriptive and predictive ability of solution thermodynamics, associated and implemented by a comprehensive knowledge of structural and physico-chemical properties, it is convenient to start with the analysis of two binary metal alloys (Ag-Au and Au-Cu), deeply discussed in the literature, for which there is an almost complete set of physical and structural information.

The experimental phase diagrams of these two binary systems are displayed in Figure 1.23. Both present a continuous series of solid solutions [90–92], while the Au-Cu system shows also the presence of low-temperature ordered phases [91].

First should be noted the very narrow liquidus–solidus gaps presented by both systems, which may be understood considering that the shape of an isomorphous type of phase diagram depends on the Gibbs free energy of fusion of the components and on the mixing terms Ω^{s} and Ω^{l}. In the hypothetical case of ideal behaviour and of close values of entropy of fusion, the liquid–solidus gap decreases with decrease in the entropy of fusion, as shown in Figure 1.24 [71] for the hypothetical case of an AB alloy.

The properties of the silver-gold system have been critically reviewed by Okamoto *et al.* [91], who argued that the very narrow liquid–solidus gap, of the order of 2 °C and less, leads to a segregation coefficient close to 1, almost independent of the temperature. Their study on the thermodynamic properties of the liquid solutions, carried out with calorimetric and EMF measurements, showed that the liquid solution is not ideal and found an interaction coefficient Ω^{l} value of -11 to 16 kJ mol^{-1} over the entire composition change, leading to a negative value of the enthalpy of mixing.

On the basis of the known values of the melting enthalpy for silver and gold ($\Delta H^{f}_{Ag} = 11.3\ \text{kJ mol}^{-1}$ and $\Delta H^{f}_{Au} = 12.5\ \text{kJ mol}^{-1}$), the entropy of fusion at 1200 K, a temperature intermediate between the melting point of Ag and Au, may be calculated as $\Delta S^{f} = \Delta H^{f}/T$, with $\Delta G_{f} = 0$ at the melting temperature. The resulting values of fusion entropy are 9.53 J K^{-1} for silver and 10.4 J K^{-1} for gold, so close to each other as to justify a very small liquid–solidus gap.

Moreover, the solid solutions are not ideal, as is suggested from accurate bond energy values for the Ag-Ag, Au-Au and Ag-Au pairs calculated by Jian-Jun *et al.* [93], for whom the Ag2 pair has a binding energy of 1.55 eV, the Au2 pair an energy of 1.88 eV and the Ag-Au pair an energy of 1.92 eV, with the Ag-Ag bond energy well comparable with the experimental value of 1.65 ± 0.03 eV [94] and with the theoretical values of 1.64–1.98 eV obtained by Kobayashi *et al.* [95]. On that basis we could estimate for the solid solution a value of the interaction coefficient $\Omega^{S} = -10\ \text{kJ mol}^{-1}$.

As could be inferred from an inspection of Figure 1.19q, these Ω values should lead to a positive curvature of the phase diagram, in extremely good agreement with the experimental shape of the Ag-Au phase diagram.

The thermodynamic properties of silver-gold alloys, therefore, are satisfactorily described by the regular solution model, which also foresees the set-up of conditions of local order in correspondence to the $Ag_{0.5}\ Au_{0.5}$ composition due to the strong Ag–Au interactions, in good agreement also with the results of Flanagan and Averbach [96], who interpreted the non-linear dependence of the Hall effect on the composition as a deviation from a free electron behaviour, due to the formation of new Brillouin zones in the solid, induced by local ordering.

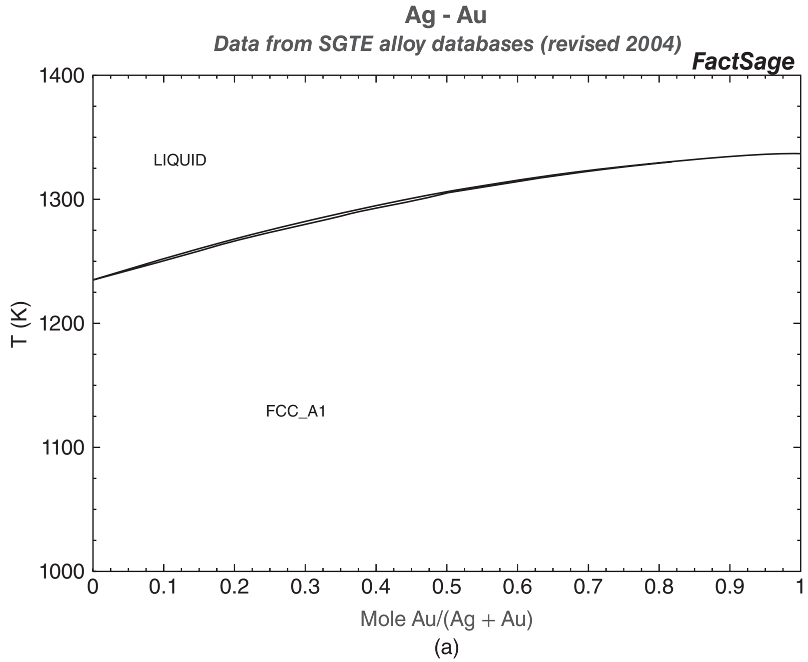

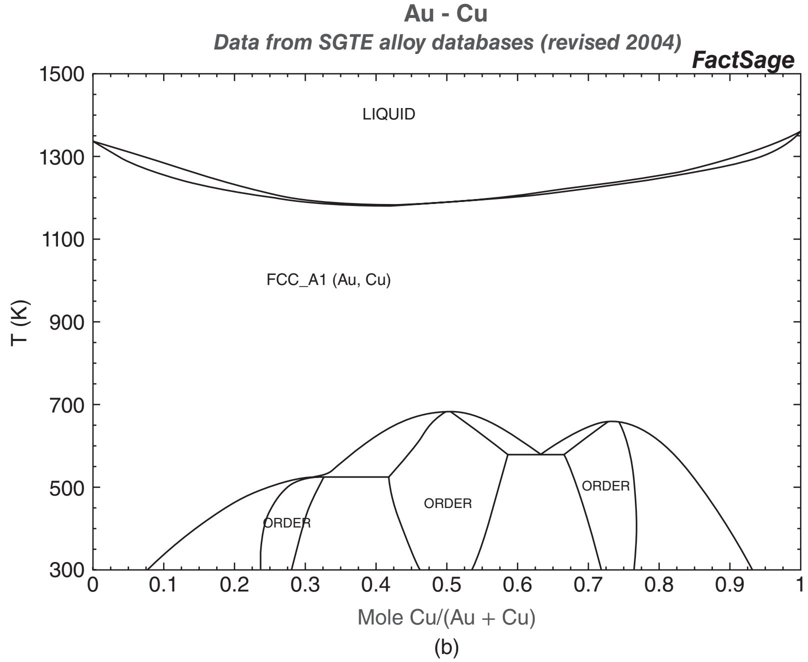

Figure 1.23 *Phase diagrams of (a) the silver-gold system and (b) the copper-gold system. Scientific Group Thermodata Europe (SGTE). Reproduced with permission from SGTE*

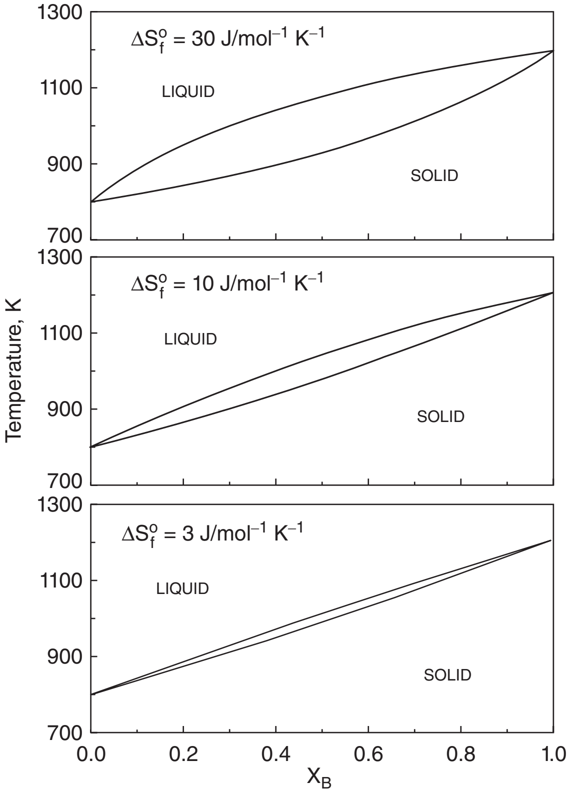

Figure 1.24 *Influence of the entropy of fusion on the width of the liquid-solidus gap. Pelton, 2001, [71]. Reproduced with permisssion from John Wiley & Sons*

The properties of the Au-Cu system, for which we expect, from an inspection of Figure 1.19p, regular behaviour for the solid solutions, with an Ω^s value around -15 kJ mol^{-1} and regular behaviour also for the liquid solutions, with an Ω^l value around -20 kJ mol^{-1}, have been critically reviewed by Okamoto *et al.* [90]. These authors give for the interaction parameter of the liquid solution a value of $\Omega^l(x) = -21.740 - 16.614\ x(\text{kJ mol}^{-1})$ and a value of $\Omega^s(x) = -11.053–22.878x\ (\text{kJ mol}^{-1})$ for the solid solutions, where x is the atomic fraction of copper. As the values of Ω correspond to the ratio $\frac{\Delta H_{\text{mix}}}{x(1-x)}$, a value of about 5.6 kJ mol^{-1} is obtained for ΔH_{mix} of the equimolar mixture.

The enthalpy of mixing values calculated using the interaction parameters given above fit well with the experimental values of heat of mixing reported by Weinberger *et al.* [97], who investigated the dependence of the heat of mixing on the composition over the whole range of Cu-Au solid solutions, see Figure 1.25.

The authors note that the shoulder at $x_{\text{Cu}} = 0.66$ may suggest the formation of the ordered phase with composition AuCu$_3$, actually present in the phase diagram of Figure 1.23b [91].

The calculated phase diagram using the interaction parameters given by Okamoto *et al.* [90] is reported in Figure 1.26, which shows a very good fit between the calculated solid–liquidus curve and the experimental results.

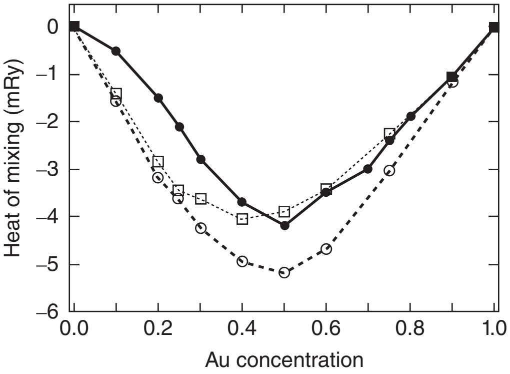

Figure 1.25 *Composition dependence of the heat of mixing of the Au-Cu system* (1 mRy = 1.31 kJ mol^{-1}). *Weinberger* et al.*, 1994, [97]. Reproduced with permisssion from American Physical Society and P. Weinberger*

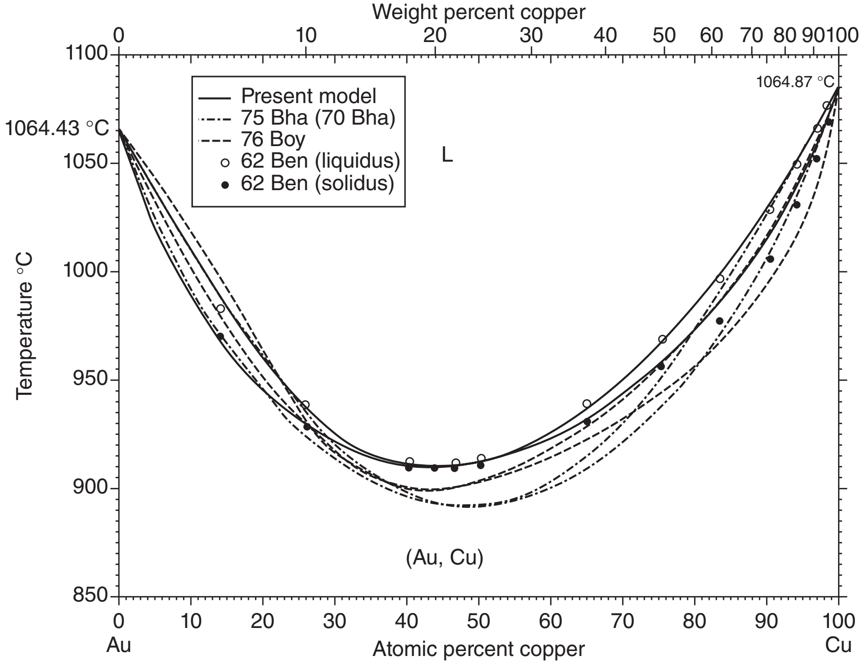

Figure 1.26 *Calculated phase diagram of the Au-Cu system. Okamoto* et al.*, 1987, [92]. Reproduced with permisssion from Springer Science and Business Media*

Okamoto's experimental values of the interaction coefficients Ω^s are composition dependent and a factor of 10 higher (−22.97 kJ mol^{-1} for the equimolar mixture) than those calculated using the bond energies determined by Szoldos [98], giving a value of 0.595 eV for the Au-Au bond, 0.590 eVfor the Cu-Cu bond and 0.623 eV for the Au-Cu bond, and thus an Ω^s value of −2.91 kJ mol^{-1}.

Apparently, the composition dependence of the Gibbs free energy of mixing in these alloys is not only ruled by chemical mixing contributions, but also by elastic energy contributions. It will be shown in Section 1.7.10 that an $\Omega^s x_A x_B$ relationship for the mixing enthalpy, according to Eq. (1.91), has a purely phenomenological character, as it accounts also for elastic energy contribution terms.

The analysis of the structural properties of these systems, which were studied, among others, by Lubarda [86], Bessiere *et al.* [91] and Weinberger *et al.* [97], add little, but significant, supplementary information about their overall behaviour.

The composition dependence of the experimental lattice parameters of Ag-Au alloys reported in Figure 1.27a shows a strong deviation from Vegard's law and a bimodal distribution of the lattice parameters, centred at $x_{Au} = 0.5$, which could be taken as a confirmation of the start of ordering in this composition range, suggested by the Hall effect measurements [96] discussed above.

The presence of slight positive deviations from Vegards law, with a maximum centred at $x_{Au} = 0.5$ (see Figure 1.27b) for the Cu-Au alloys could instead be correlated with the onset of ordered domains at low temperature (see Figure 1.23b), in agreement with the results of Hall effect measurements which show here an important decrease in the Hall effect with a minimum corresponding to $Au_{0.5}$ $Cu_{0.5}$. This effect was interpreted as due to the formation of new Brillouin zones, corresponding to the establishment of structural ordering and superlattice stabilization [95].

The analysis carried out on the properties of these metallic alloys shows the tremendous value of the complementary use of structural, physical and theoretical methods to implement the information coming from thermodynamics, a research methodology that will be demonstrated to be even more important in the case of semiconductor systems. The analysis shows also that in the case of these metallic alloys the regular solution model apparently works well, but that the model should be taken as a phenomenological rather than a physical model. In addition, as will be shown more clearly in the next sections, the deviations from Vegard's law have little to do with the thermodynamics of the solid solutions.

1.7.3 Silicon and Germanium

Silicon is known as the material of choice for microelectronic and photovoltaic applications and the study of its structural, physical and physico-chemical properties has been the subject of systematic experimental and theoretical investigations over the last 60 years. It has also been also as a model system for advanced simulations using *ab initio* MD calculations, as will be shown later in this section. Only recently, germanium gained a strategic role in microelectronic technology, after the development of strained Si-Ge structures presenting enhanced carrier mobility. The main physical properties of silicon and germanium, together with those of other elemental semiconductors which will be dealt with in this and the following chapters, are reported in Table 1.6.

In spite of being one of the most extensively studied semiconductors [99], the complete phase diagram of silicon is only known approximately because of the challenge of measurements in extreme temperature and pressure conditions.

It has, however, been demonstrated that certain tight binding models [100] and *ab initio* MD calculations provide an accurate description of the thermal properties of this system and the correct simulation of phase transformations, respectively. In the case of *ab initio*

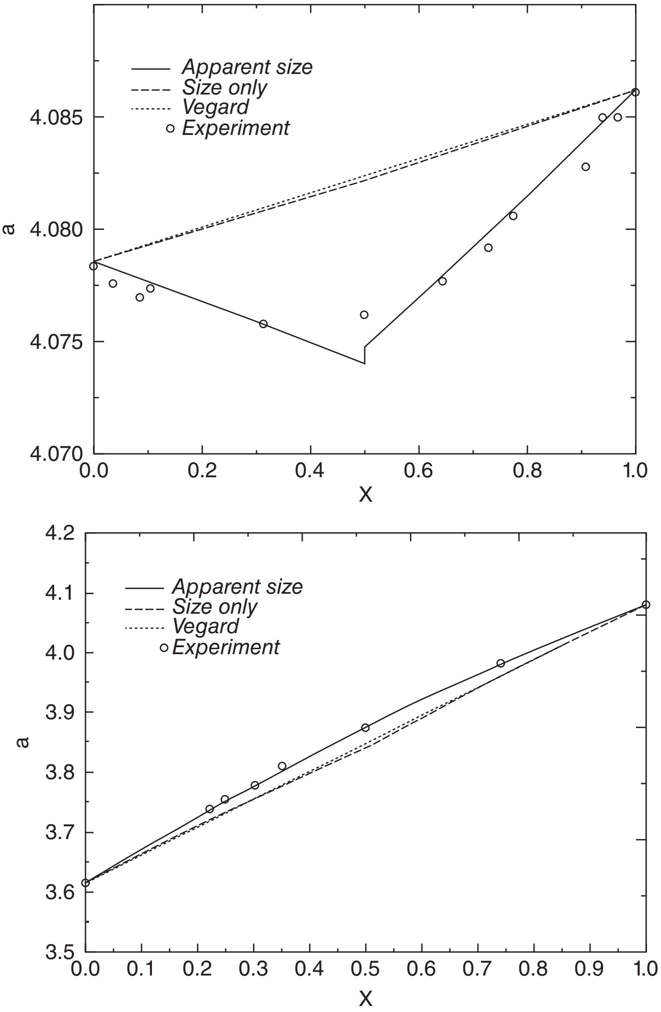

Figure 1.27 *Composition dependence of the lattice constants of the Au-Ag (a) and the Cu-Au system (b). Lubarda, 2003, [86]. Reproduced with permisssion from Elsevier*

MD calculations, the advantage is that the combination of the Car–Parrinello with the Car–Rahman method [101] allows a correct quantum-mechanical description of the interatomic forces and internal stresses of the material.

Concerning the properties experimentally available, both silicon and germanium present a negative Clapeyron slope $\mathrm{d}t/\mathrm{d}P$ along the melting line of their diamond-cubic, low pressure polymorphs (see Figure 1.28a,b) due to the higher density of the liquid phases and both present a number of different high-pressure polymorphs.

The most studied high-pressure polymorphs of silicon and germanium are the metallic β-Sn phases (Si II and Ge II in Figure 1.28), stable above ~12 GPa, but other Si and Ge phases are stable or metastable at increasing pressures. As an example, Table 1.7 reports

Table 1.6 *Physical properties of Group IV and VI semiconductors*

	Silicon	Germanium	Carbon	Selenium	Tellurium
Melting temperature (T_m (K))	1685	1210	3823	494	722.66
Structure	Diamond cubic	Diamond cubic	Diamond cubic	Monoclinic	Trigonal
Lattice constants (nm)	0. 5431	0.5658	0.35668	a : 0.9054 b : 0.9083 c : 1.1601 $\alpha = \gamma = 90°$ $\beta = 90.810°$	a : 0.4457 b : 0.4457 c : 0.5299 $\alpha = \beta = 90°$ $\gamma = 120°$
Density (g cm^{-3}) at 298 K	2.3296	5.323	3.52	4.809	6.240
Density of the solid at T_m	2.29	5.22	3.51	—	—
Density of the liquid at T_m	2.54	5.51	1.2	3.99	6.2
Electron mobility (cm^2 V^{-1} s^{-1})	1400	3900	2200	—	—
Hole mobility (cm^2 V^{-1} s^{-1})	450	1900	1600	—	—
Band gap (eV)	1.12	0.661	5.45	2.25	—

Data from Glazov and Shchelikov, 2000, [99].

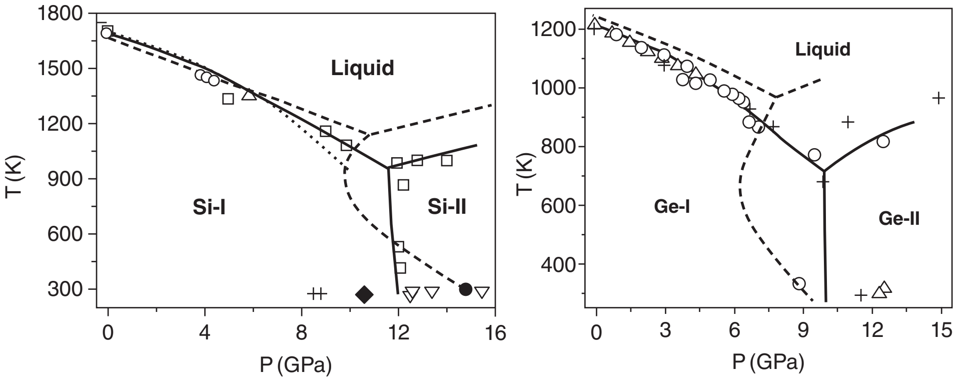

Figure 1.28 *(a) Phase diagram of silicon. Solid, dashed and dotted lines: theoretical predictions, symbols: experimental results. Yang* et al.*, 2004, [102]. Reproduced with permisssion from Elsevier. (b) Phase diagram of germanium. Solid, dashed and dotted lines: theoretical predictions, symbols: experimental results. Yang* et al.*, (2004) [103]. Reproduced with permission from Elsevier*

the crystal data for 6 high-pressure phases of silicon [105], but the actual situation is more complex as at least 11 silicon high-pressure phases are known to be stable.

It has been observed that the high-pressure Si phases never convert directly back to the diamond phase by pressure release, but undergo transformation into several metastable phases. As an example, the β-Sn phase of Si undergoes by pressure release first a transition to an intermediate rhombohedral R8 phase which then transforms to the metastable BC8 phase. On heating at ambient pressure the BC8 phase transforms to another phase which has the hexagonal diamond (HD) phase structure.

Table 1.7 *Crystal data structures of main silicon polymorphs*

Designation	Structure	Pressure region (GPa)
I	Cubic (diamond)	0 → 12.5
II	Body-centred tetragonal (β-Sn)	8.8–16
III	Body-centred cubic (BC8)	~10 → 0
V	Primitive hexagonal	~14 → 40
VII	Hexagonal close packed	40–78.3
VIII	FCC cubic	≥78.3

EMIS Data Review Series, 1988, [104]. Reproduced with permission from the Institution of Engineering and Technology.

The corresponding β-Sn phase of Ge undergoes instead a transformation to a short-lived metastable BC8 phase by rapid depressurization or to the tetragonal ST12 phase by slow depressurization [105, 106]. It should be noted, however, that the experimental transition pressures do not necessarily correspond to the equilibrium ones because kinetic factors are involved.

The phase diagrams of silicon and germanium were originally studied by Bundy [107] early in 1964 and recently revisited by Yang *et al.* [102, 103] and by Kaczmarski *et al.* [100], see Figure 1.28. It can be seen that in both cases the agreement between the theoretical predictions and the experiments is particularly good in the relatively narrow pressure/temperature range of the equilibria involving the cubic diamond and β-Sn type solids with the liquid phase.

The Car–Parrinello and Car–Rahman methods have been used by Bernasconi *et al.* [101] and Car and Parrinello [108] for the simulation of the transition of silicon from the cubic diamond- to β-Sn structure, which is complicated by the high energy barrier inherent to this transition and yielded large overpressurizations (42 GPa vs 12 GPa). To overcome the problem, Behler *et al.* [109] adopted a modified Parrinello–Rahman method, based on the introduction of a bias-potential to overcome the large energy potential of the transformation. Using this method several other high-pressure transitions were successfully studied [109].

The theoretical study of solid–liquid transitions in silicon and germanium is very challenging, as liquid silicon and germanium present some unusual properties. Upon melting, different from metals, a density increase of ~10% occurs in silicon and ~5% in germanium [50] (see Table 1.6) and the coordination rises from 4 to 6–7 at the phase transition. This is a lower coordination than would be expected if the liquid were entirely metallic, and is interpreted as an indication of persistence of covalent bonding [110], in agreement with XR-diffraction measurements carried out close to the melting temperature [111] and density measurements [112].

A recent re-examination of the properties of liquid silicon carried out by the Car and Parrinello group, aimed at getting direct information of the temperature dependence of the liquid Si density [113] not only supported the hypothesis of persistence of covalent bonding in liquid silicon [110, 113], but also indicated that liquid silicon is a mixture of two polymorphs, one covalently bonded and the other behaving as metallic silicon [114]. It has been found using inelastic X-ray scattering, that a population of 17% of covalent-bonded silicon atoms coexists at 1787 K with metallic-bonded silicon atoms in liquid silicon [115].

Similar behaviour has been observed in liquid germanium, where the persistence of a strong covalent bonding in the liquid state has been demonstrated [116–118], as well as a decrease in the fraction of the covalently bonded Ge with increase in pressure.

It will be shown also that carbon with the structure of diamond presents a similar, even more complicated behaviour, which is typical of Group IV semiconductors.

1.7.4 Silicon-Germanium Alloys

Few binary elemental semiconductors systems of Group IV present conditions of complete solid solubility, among which the case of silicon-germanium alloys is particularly interesting for the role played by these alloys in microelectronic and optoelectronic technology, together with their elemental precursors (see Table 1.6), as has been preliminarily mentioneded in the last section.

Silicon-germanium alloys, thanks to the elevated electron mobility of germanium, cover a technology sector where silicon is in decline, as they enable faster, more efficient devices to be manufactured using smaller, less noisy circuits than conventional silicon, through greater integration of components onto the chips.

The key advantage of silicon-germanium alloys over their rival technologies is their compatibility with mainstream complementary metal-oxide semiconductor (CMOS) processing. In addition, silicon-germanium alloys provide ultra high frequency capability (well over 100 GHz) on the identical silicon platform where baseband, memory and digital signal processing functions can also be integrated. This is the rationale and the reason why silicon-germanium alloys appear prominently on the technology roadmaps around the world and why they attract increasing attention.

The phase diagram of this system has been studied by Olesinski and Abbashian [119] and reported in a revised form in Figure 1.15: it looks qualitatively very close to the calculated one of Figure 1.14, based on the assumption of the ideality of both the liquid and solid solutions.

On the basis of the bond energies of solid alloys reported in the literature ($E_{\mathrm{Si-Si}} = -2.32$ eV, $\mathrm{E}_{\mathrm{Ge-Ge}} = -1.94$ eV and $\mathrm{E}_{\mathrm{Si-Ge}} = -2.12$ eV [120] one obtains an interaction coefficient for the solid solutions close to zero ($\Omega^{s}(\mathrm{eV}) = +0.01$ eV). This value is consistent with the assumption of ideality of the solid solutions and with the experimental values of the heat of mixing, which are small ($\Delta H_{\max} \sim 1.3\ \mathrm{kJ\ mol^{-1}}$) and positive (see Figure 1.29) [121].

These results also agree well with those obtained by Jivani *et al.* [121], see again Figure 1.29, who carried out the theoretical evaluation of the Gibbs free energy and of the heat of mixing of $\mathrm{Ge}_x\mathrm{Si}_{1-x}$ solutions using a pseudo-potential theory of covalent crystals [122].

They confirmed that the heat of mixing of the solid solution is small and positive, predicting small deviations from the ideality and un-mixing features at low temperature, in agreement with the results of an earlier study of Dunweg and Landau [123]. The modelling of the liquid solution is more challenging, in view of the presence of two phases, one metallic and the other covalent, as shown in the last section.

We could suppose, therefore, that the liquid $\mathrm{Si}_x\mathrm{Ge}_{1-x}$ alloys are heterogeneous mixtures of covalent- and metallic-bonded Si and Ge, making the evaluation of the liquid–solid equilibria questionable when carried out in terms of a simple regular solution model.

The structural aspects of these alloys are also challenging. There is experimental evidence from XR diffraction measurements of slightly negative deviations of the lattice

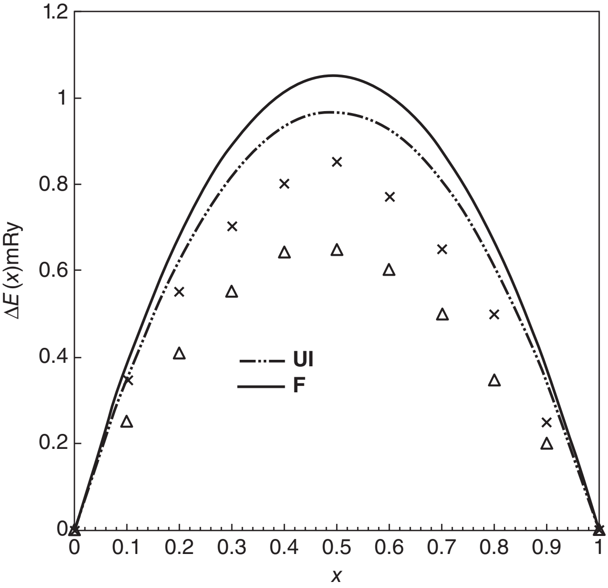

Figure 1.29 *Dependence of the heat of mixing on the composition of the* Ge_xSi_{1-x} *alloys. Jivani* et al.*, 2005 [121]*

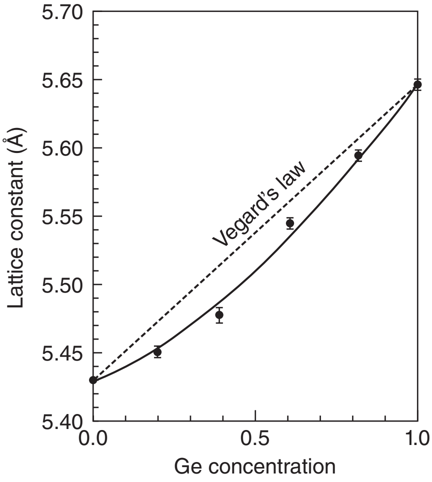

Figure 1.30 *Dependence of the lattice parameters on the* Si_xGe_{1-x} *alloy composition. Kajiyama* et al.*, 1992, [124]. Reproduced with permission from American Physical Society*

distances from Vegard's law (see Figure 1.30) and of almost complete relaxation of Ge-Ge and Ge-Si bonds, from EXAFS measurements (see Figure 1.31). These latter show that the bond lengths are independent of the solution composition and closely follow the Pauling limit [124]. The authors did not investigate directly the Si-Si bond distances, but it was supposed that these bonds are also completely relaxed close to a bond length of 0.235 nm, which is the sum of two Si atomic radii.

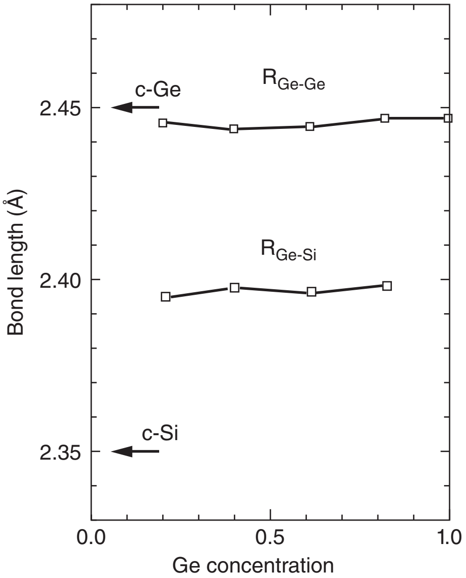

Figure 1.31 *Ge-Ge and Ge-Si bond lengths (R in the figure) as a function of the Ge concentration in* $Si_{(1-x)}Ge_x$ *alloys. Kajiyama* et al.*, 1992, [124]. Reproduced with permission from American Physical Society*

The explanation given is that bond angle distortion accounts for the monotonic variation of the lattice distances and that their non-linear variation might be considered a consequence of the bond lengths invariance.

Shen *et al.* [125] showed that the experimental values of the relaxed bonds could be significantly well predicted using a simple radial force model, while models based on the valence force field fail when the bond-bending forces are included.

Eventually, it was also found from the study of the coordination ratio of Ge in Ge-Si solutions that the distribution of Si and Ge atoms in the lattice is random [124].

The final conclusion is that close lattice parameters, random mixing and close bond energies values are sufficient to make Si-Ge alloys near to ideal solid solutions.

1.7.5 Silicon- and Germanium-Binary Alloys with Group III and Group IV Elements

The solubility of Group III and IV elements in germanium and silicon is generally low or negligible and, consequently, eutectic type phase diagrams are representative of these binary systems.

The solubility of boron in solid germanium is $5 \cdot 10^{18}$ at cm^{-3} at 850 °C [126], but it is known that its solubility might be enhanced, as occurs for B in silicon [127], by point defects engineering, a technique which will be discussed in Chapters 2 and 5.

The phase diagram of the B-Si system is reported in Figure 1.32 [128], which shows that the solid solubility of B at the eutectic temperature is around 2% in mass units or $3 \cdot 10^{21}$ at cm^{-3}, as also shown by later studies [129].

Carbon also exhibits a limited solubility in solid Si and Ge, see Figure 1.33 [130], as a consequence of the very large difference in lattice parameters (see Table 1.6) and of the

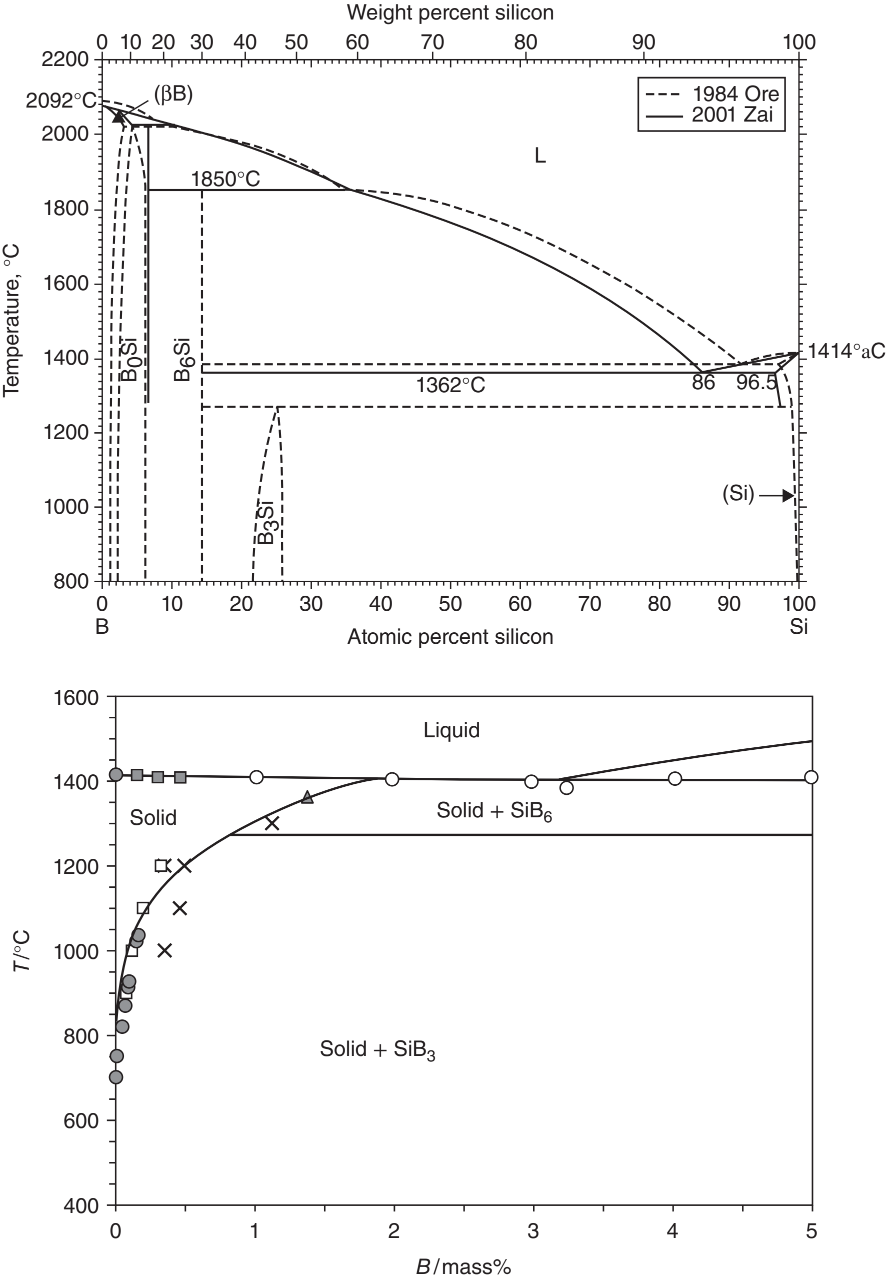

Figure 1.32 *Phase diagrams of the boron-silicon system. Okamoto, 2005, [128]. Reproduced with permission from Springer Science and Business Media*

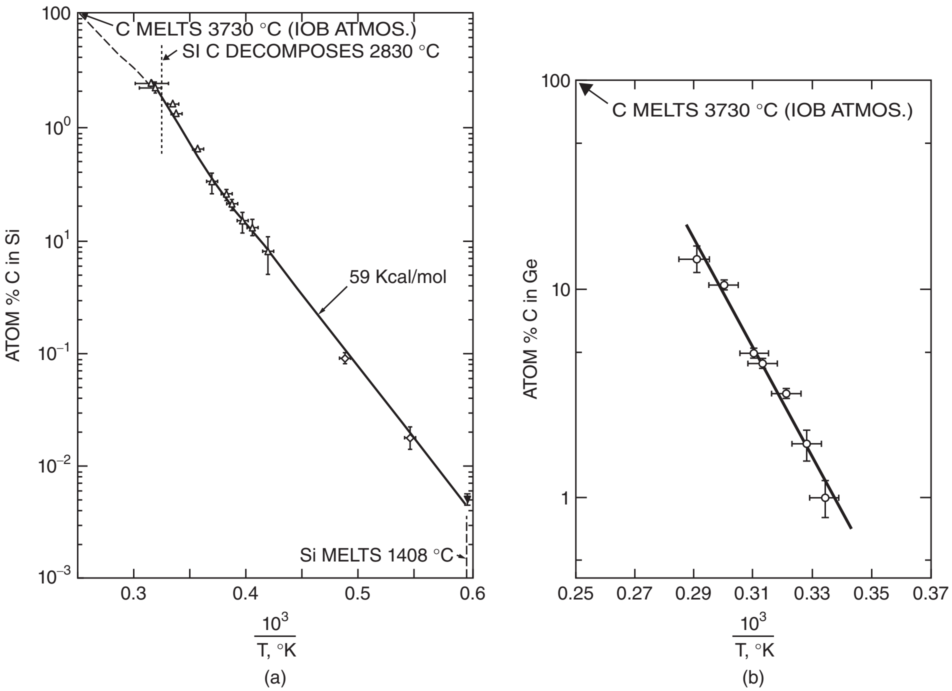

Figure 1.33 *Solubility of carbon in silicon (a) and germanium (b). Scace, 1959, [130]. Reproduced with permission from AIP Publishing*

large Si-C and Ge-C bond energies (318 and 238 kJ mol^{-1}, respectively), which leads to the stability of intermediate phases. While the C-Si system has been the subject of detailed studies in the last few decades, with thousands of published papers, in view of the role of C as an unwanted and detrimental impurity in semiconductor silicon and as the precursor of SiC precipitates, as will be dealt with in Chapters 2 and 3, very limited information is available on the C-Ge system [131].

For both binaries the phase diagrams are available, in full detail for the C-Si system, see Figure 1.34a, as originally investigated by Olesinki and Abbaschian [132], and in less detail for of C-Ge, which was originally investigated by Scace and Slack [130] (see Figure 1.34b). It is worth noting that all the Ge-C phase diagrams, including that recently calculated by Hu *et al.* [131] ignore the presence of the intermediate GeC phase.

Actually, different from the case of silicon carbide, only recently germanium carbide (GeC) has attracted experimental and theoretical interest [133, 134], mostly because it is now being considered as a promising alternative material for photovoltaic and electro-optical applications. The carbon addition in germanium results in an increase in its band gap and a reduction in the lattice parameters, thus allowing its ordered growth on Si substrates [135].

In spite of the relatively close atomic radii ($r_{\mathrm{Si}} = 0.1319$ nm, $r_{\mathrm{Ge}} = 0.1369$ nm, $r_{\mathrm{Al}} = 0.1432$ nm), which should favour larger solid solubilities, the phase diagrams of the Al-Ge

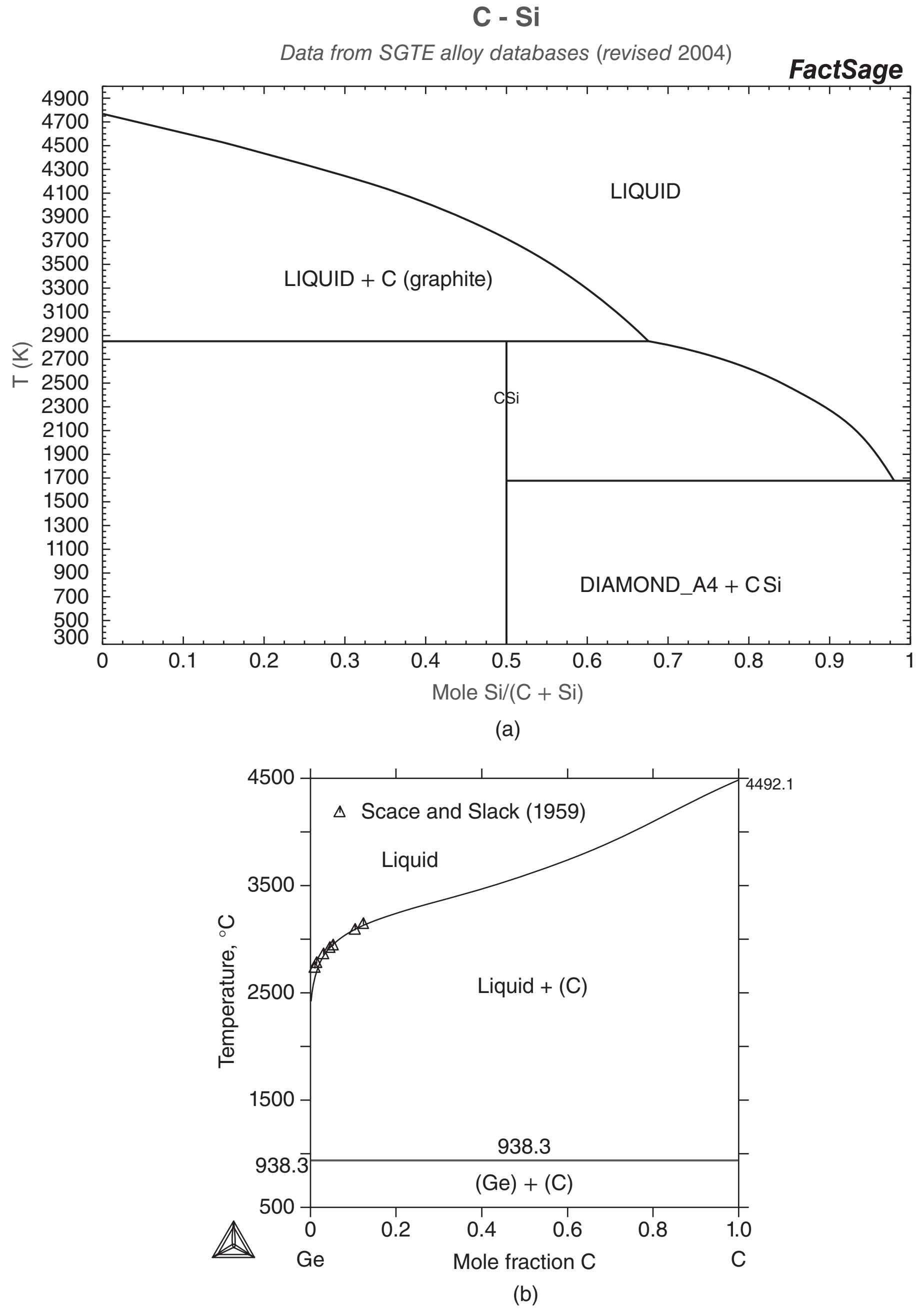

Figure 1.34 *(a) Phase diagram of the C-Si system. Scientific Group Thermodata Europe (SGTE). Reproduced with permission from SGTE (b) Calculated phase diagram of the C-Ge system. Hu* et al.*, [131]. Reproduced with permission from Y. Du*

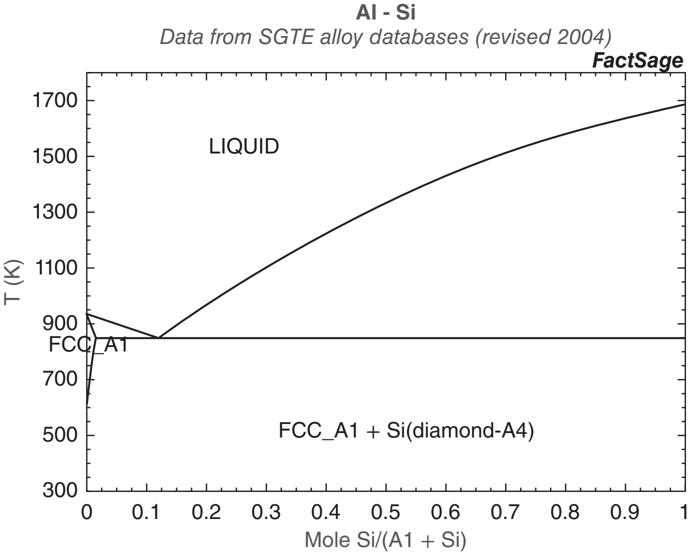

(a)

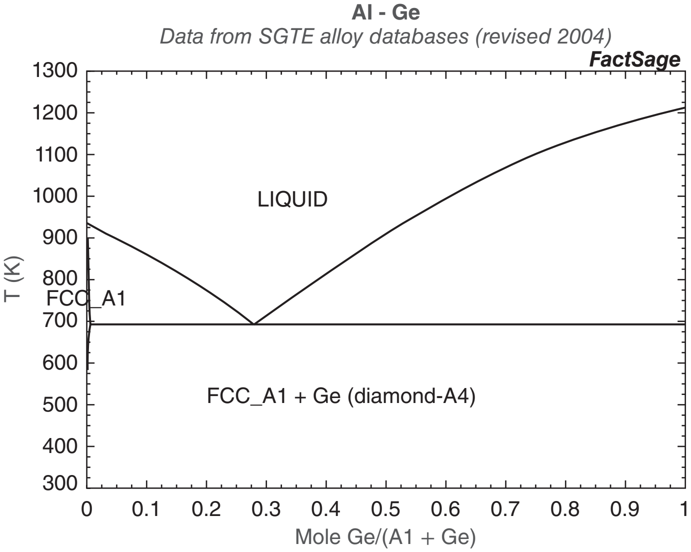

(b)

Figure 1.35 *Phase diagrams of (a) Al-Si and (b) Ge-Si. Scientific Group Thermodata Europe (SGTE). Reproduced with permission from SGTE*

and Al-Si systems are typical of metal-semiconductor systems presenting limited reciprocal solubility (see Figure 1.35). It is interesting to note, however, that the solubility of Al in Ge finds its maximum (1% in weight) at the eutectic temperature [136], while that of Al in silicon shows a retrograde behaviour (see Figure 1.36), with a solubility maximum (450 ppmw) at 1450 K [129, 137].

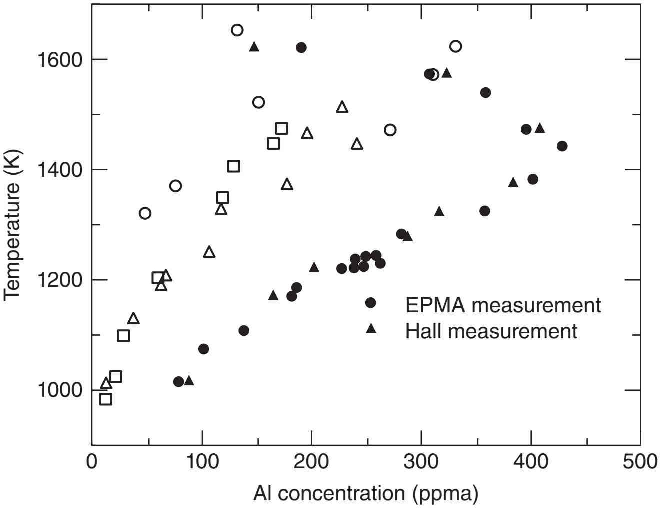

Figure 1.36 *Solid solubility of Al in silicon (EMPA = electron probe microanalysis). Yoshikawa and Morita, 2003 [137]. Reproduced with permission from Electrochemical Society*

The limited solid solubility of Si in Al is a technological obstacle to the growth of homogeneous, Si-rich Al-Si alloys, but the possibility of inducing a larger solid solubility of Si (and Ge) in Al was demonstrated experimentally using a rapid quenching process of Si-Al or Ge-Al melts under pressure (10 GPa) [138].

This last effect might be qualitatively accounted for by the increase in the melting temperature of aluminium with increase in pressure (see Figure 1.7) [53] and by the contemporaneous decrease in the melting temperature of silicon (see Figure 1.8) [42] (see Section 1.4.5 for details).

It was also explained theoretically [54, 139] using an extension to solid solutions of Lindeman's melting law [51] already discussed in Section 1.4.5. The agreement between the experimental and calculated values is reasonably good, as shown in Figure 1.37.

As the solubility of silicon in liquid Al (see again Figure 1.37) is appreciable at temperatures well below the melting point of silicon, Al has been proposed for use industrially as a refining medium for metallurgical (MG) silicon [140], in spite of potentially severe problems of minority carriers lifetime degradation caused by the presence of traces of Al in silicon crystallized from an Al-rich silicon melt [140].

It is known that Group III elements (B, Al, Ga) behave as electron acceptors, but that Al also behaves as recombination centre in silicon, thanks to the presence of two deep levels at 0.315 and 0.378 eV [141, 142], of which the second is a hole trap and the first is a recombination centre, both possibly associated to the Al–O centres in single crystal silicon, as will be discussed in Chapter 2.

A significant advantage of Al refining over other refining routes comes, however, from the very low segregation coefficients of metallic impurities in Al-Si solutions, which are even lower than the corresponding segregation coefficients in liquid silicon [143], thus granting an effective purification from B and TM elements, which are the main and the most deleterious contaminants of MG silicon.

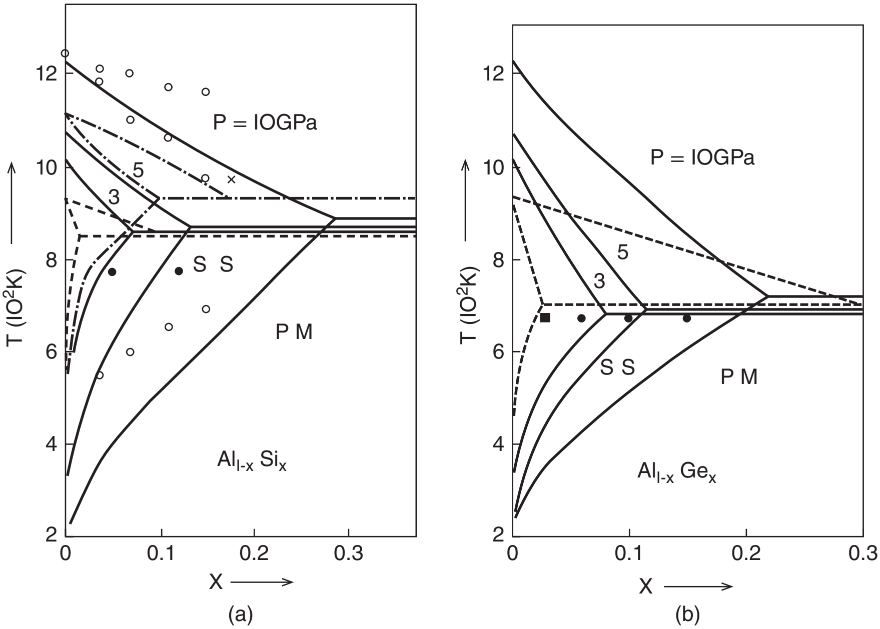

Figure 1.37 Effect of the pressure on the solubility of (a)silicon and (b)germanium (b) in aluminium. • experimental points. Kagaya et al.*, 1998 [139]. Reproduced with permission from Elsevier*

By a suitable quenching of saturated liquid solutions of Si in Al one can segregate virtually pure silicon lamellae which can be filtered from the liquid solution [143, 144] and further processed by ingot growth processes, which could bring the Al-content in silicon to acceptable levels, as will be discussed in Chapter 4.

1.7.6 Silicon-Tin and Germanium-Tin Alloys

The other Group IV elements (Sn and Pb), present a limited solubility in Ge and Si, leading to eutectic type diagrams. It should be mentioned here that Ge-Sn alloys are receiving growing attention because it is predicted that, at 10% Sn content, unstrained $Ge_{1-x}Sn_x$ should exhibit a direct band gap leading to important optoelectronic applications.

In strained, cubic diamond $Ge_{1-x}Sn_x$ theoretical studies suggest that the crossover concentration towards a direct band gap should be even lower [145–148], stressing the importance of Sn doping for advanced microelectronic applications of Ge.

Chapter 3 will deal with details concerning the preparation of strained materials, but here it is sufficient to note that although thermodynamic constraints would forbid the preparation of Ge-Sn alloys at equilibrium compositions above the saturation (the maximum solubility of Sn in Ge is 0.5 at%), the use of the epitaxial deposition of a thin epitaxial layer of a Ge-Sn alloy on a substrate presenting a proper lattice mismatch would provide the right solution. It has be shown that strained metastable epitaxial layers of $Sn_{0.07}Ge_{99.3}$, 40–100 nm thick, could be prepared on a silicon substrate with an intermediate, 1 μm thick, Ge buffer layer [24], opening the way to the use of these alloys in advanced optoelectronic applications.

1.7.7 Carbon and Its Polymorphs

Diamond is not only unique among semiconductors for its extreme values of hardness[9] and energy gap, which is of interest for the development of semiconductor devices working in harsh environments (i.e. very high temperature and high γ-rays level), but has been also selected as one of the materials of possible use for inertial confinement fusion (ICF) applications [149]. Graphite, on the other hand, is used as the precursor of diamond and, more recently, of graphene and is a material of common use in high-temperature applications as a mechanical support, as a crucible or as a heating element.

Due to the extreme difficulty of carrying out experiments even in the pressure/temperature range of the coexistence equilibria involving the two common solid polymorphs of carbon (graphite and diamond) and liquid carbon, which occur at temperatures between 4000 and 6000 K and pressures between 100 and 1000 GPa, the thermodynamic properties of this system are not yet well known and most, though not all, of the known properties are the result of theoretical studies.

So far, only the graphite/diamond and the graphite/liquid phase boundaries, that occur at relatively low temperatures and pressures, have been located experimentally with reasonable accuracy [150–155].

The phase diagrams of carbon, displayed in Figure 1.38a,b, are the result of the pioneering experimental studies of Bundy [150–153], who succeeded in defining the thermodynamic properties of the system in the temperature/pressure range of the graphite/diamond/liquid carbon coexistence.

It should be noted that in both diagrams the Clapeyron dT/dP slope of the graphite melting line is positive, in good agreement with the experimental values of the density of the liquid at low applied pressures (1.2 g cm^{-3}) compared to graphite (2.26 g cm^{-3}). The negative slope above the melting point of diamond shown in the original diagram of Figure 1.38a was, however, based on a hypothetical analogy of diamond with silicon and germanium, for which the density of the liquid is higher than that of the solid. This conjecture was abandoned after the 1980s when the results of experimental [153] and theoretical work [156] demonstrated that the slope is actually positive. Boundy *et al.* [153] also showed that the liquid in equilibrium with solid diamond is metallic but that there is also evidence of a transformation between a non-conducting and a conducting form of liquid carbon.

This conclusion is in good agreement with the results of Togaya [154], who suggests the onset of a first order transition in liquid carbon along the melting line of graphite at 5 GPa. The same author also showed that liquid carbon is 10 times more resistive than liquid silicon (80 μΩ cm) and germanium (75 μΩ cm) (see Figure 1.39) and proposed, as a preliminary qualitative explanation, that it could arise from the basically covalent structure of liquid carbon, with three of the four valence electrons involved in covalent bonding and the conducting electron being strongly localized. It is in any case apparent that liquid carbon, as silicon and germanium (see Section 1.7.3), is stable also in a non-metallic form, but that the larger C-C bond energy (347 kJ mol^{-1} vs 222 kJ mol^{-1} for Si-Si and 188 kJ mol^{-1} for Ge-Ge bonds) favours the persistence of a larger amount of covalently bonded C in liquid carbon.

---

[9] A recent work [149] shows that C60 molecules solvated with m-xylene give rise to an ordered structure phase that becomes harder than diamond at pressures above 32 GPa.

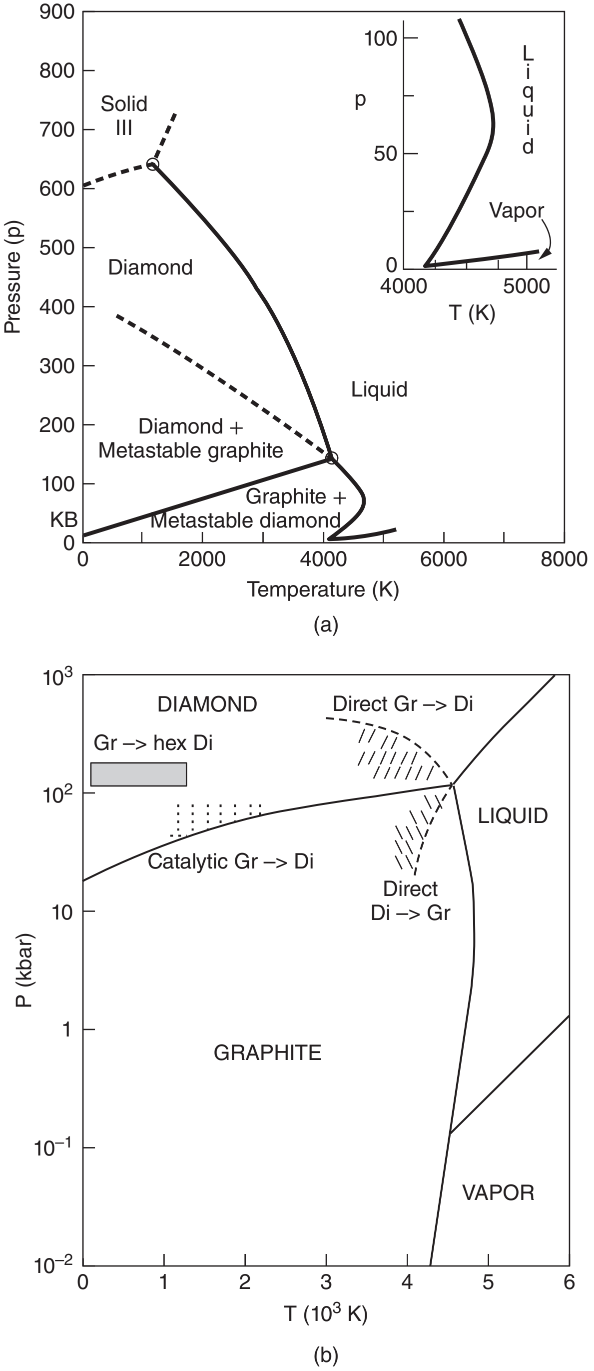

Figure 1.38 *(a) Phase diagram of carbon (dotted lines: extrapolations or predictions). Bundy, 1963 [151]. Reproduced with permission from AIP Publishing (b) Updated diagram. Bundy, 1989, [152]. Reproduced with permission from Elsevier*

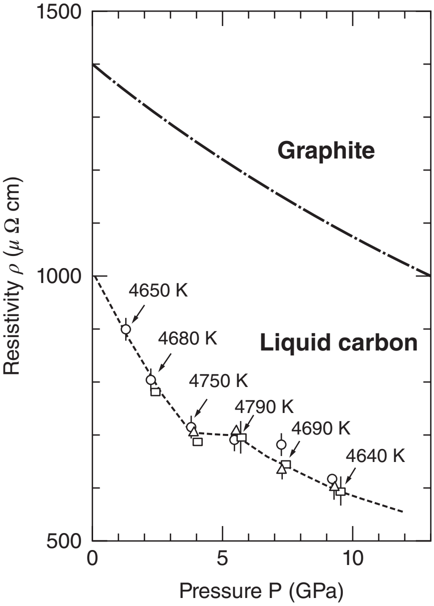

Figure 1.39 Experimental dependence of the resistivity of graphite and liquid carbon along the melting line of graphite. Togaya, 1997, [154]. Reproduced with permission from American Physical Society and M. Togaya

Additional information on the properties of the carbon system might be inferred from the phase diagram of Figure 1.38b, which shows that the triple point where diamond, graphite and liquid phases coexist occurs in a temperature range around 4500–5000 K for pressures close to 12 GPa. It also shows the presence of a region where a hexagonal polymorph of diamond can be found as a metastable phase and indicates that the equilibrium graphite → diamond transformation occurs under catalytic enhancement. In the same diagram it is also shown (dotted curves on the top region of the diagram) that the direct transformation of diamond (D) to graphite (G) and graphite to diamond (dotted line at the top of the figure) does not occur spontaneously at the coexistence pressures, but requires much higher pressures in the absence of catalysts.

This apparently happens notwithstanding graphite and diamond having very close Gibbs free energies of formation and, consequently, that the transformation enthalpy and entropy are very small ($\Delta H_{G\rightarrow D} = +1.897$ kJ mol^{-1}, $\Delta S_{G\rightarrow D} = -3.36$ J mol^{-1} K^{-1}). It can be demonstrated that excess temperatures and/or pressures are required to overcome the high activation energy for the transformation (728 kJ mol^{-1}), a process which implies the rupture of graphitic bonds and their rebonding via sp3 hybridization.

At lower synthesis temperatures, the formation of HD, a metastable polymorph of diamond, from graphite is favoured instead of the stable cubic diamond phase. Static compression of graphite at 1200–1700 K results in the formation of HD and further compression results in the formation of diamond, but never at pressures lower than 12 GPa, much higher than the coexistence pressure in this temperature range.

Moreover, the transformation of the metastable HD to graphite does not occur spontaneously, but requires either the assistance of catalysts or its enhancement by size effect factors [157], which were examined in detail by Khaliullin *et al.* [158], as will be seen later in this section.

These uncommon features have been the subject of a number of theoretical studies, aimed at the development of models capable of explaining the physical grounds of this behaviour.

Among the considerable amount of literature available on the subject, one has to deal, at first, with the work of Wang *et al.* [159] who calculated the diamond melting line using an *ab initio* Car–Parrinello MD scheme (see Figure 1.40a) and proposed the phase diagram shown in Figure 1.40b.

It can be observed that the Clapeyron slope is positive up to 600 GPa, turning then to slightly negative values. Using the density-functional theory based on MD *ab initio* simulations, Ghiringhelli *et al.* [161] obtained the phase diagram of Figure 1.41 which confirms the positive Clapeyron slope for the diamond melting line in the low-pressure range.

The same authors calculated the solid and liquid densities as a function of the pressure (see Table 1.8 [161]) and showed that the density of both solid and liquid increase with pressure, with a tendency for the liquid to become denser than the solid, in good agreement with the results of Wang *et al.* [159] and of Grumbach and Martin [162]. These last authors observed a change from fourfold to sixfold coordination in the liquid when the pressure varied from 400 to 1000 GPa, just in the range where the liquid becomes denser than the solid.

An important aspect of the physical chemistry of carbon is the thermodynamics of the phase transformations of carbon polymorphs, which have been studied by among others, Dmitriev *et al.* [163] and Khaliullin *et al.* [158]. According to Dmitriev *et al.* [163] the graphite → diamond transition may be interpreted as a transition between two low-symmetry, ordered phases, which are formed from a latent, parent disordered phase

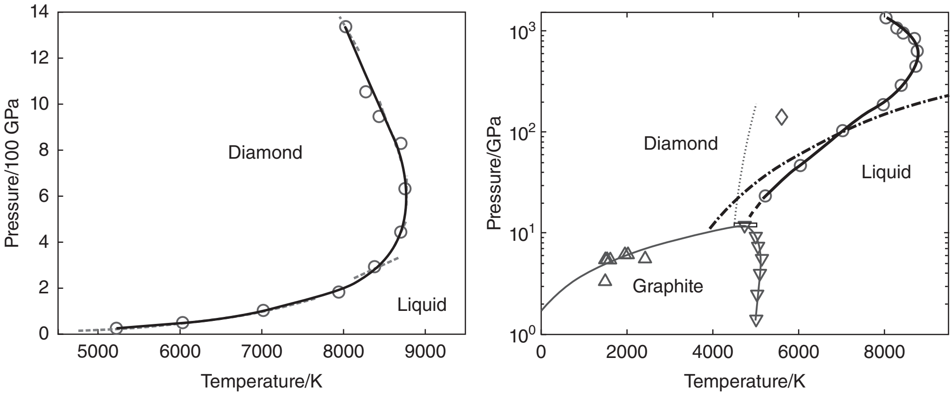

Figure 1.40 *(a) Calculated melting line of diamond (open circles are calculated values, dotted line are the Clapeyron slopes). (b) Phase diagram of carbon (solid line from F.P. Bundy* et al. *[160]). Wang* et al.*, 2005, [159]. Reproduced with permission from American Physical Society and S. Scandolo*

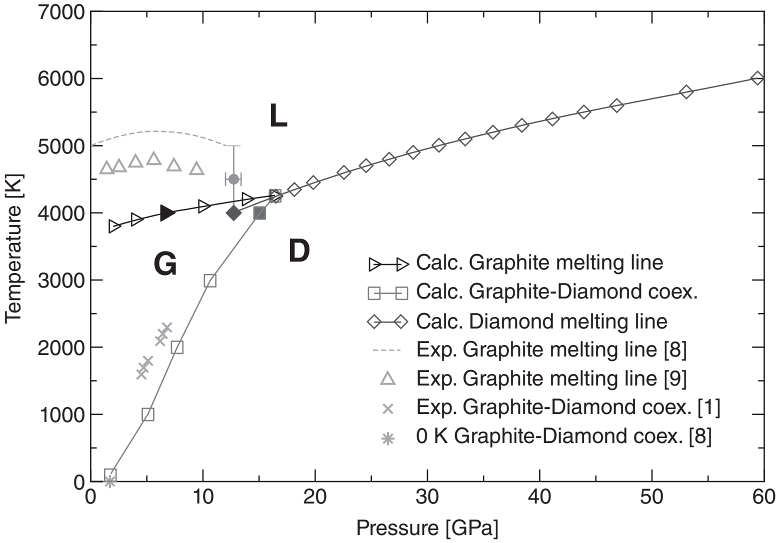

Figure 1.41 *Phase diagram of carbon. Ghiringhelli* et al.*, 2005, [161]. Reproduced with permission from American Physical Society and L. Ghiringhelli*

Table 1.8 *Effect of the pressure on the density of solid and liquid carbon*

P (GPa)		T (K)	ρ_s (g cm^{-3})	ρ_l (g cm^{-3})
2.0	Graphite	3 800	2.134	1.759
6.7		4 000	2.354	2.098
16.4		4 250	2.623	2.414
16.4	Diamond	4 250	3.427	2.414
25.5		4 750	3.470	2.607
43.9		5 500	3.558	2.870
59.4		6 000	3.629	3.043
99.4		7 000	3.783	3.264
148.1		8 000	3.960	3.485
263.2		10 000	4.286	3.868
408.1		12 000	4.593	4.236

Data from Ghiringhelli *et al.*, 2005, [161].

by a combined mechanism of ordering plus shift for the diamond structure and ordering plus decompression for the graphite structure.

Khaliullin *et al.* [158] studied the same process using first principle arguments and concluded instead that the slow stage of the phase transformation of graphite to diamond is a nucleation process of an embryo of the diamond phase, which forms by sp3 hybridization in defective regions of the graphite lattice, whose activation enthalpy strongly depends on the pressure (see Figure 1.42).

This result agrees well with the experimental features of the same transformation, which occurs under catalytic support. They could also demonstrate that the formation of the hexagonal polymorph of diamond during the transition of graphite to diamond is associated

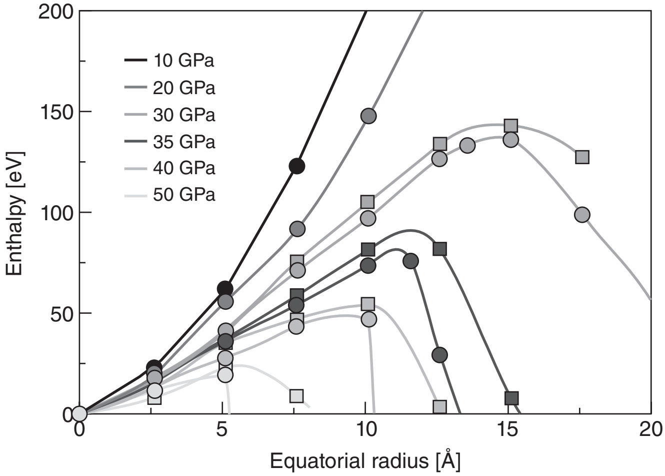

Figure 1.42 *Pressure dependence of the nucleation barriers for the graphite-diamond transition* RG → CD *(circles) and* HG → HD *(squares). Khaliullin* et al.*, 2011, [158]. Reproduced with permission from Macmillan Publishers*

with similar activation energies for the transition of rhombohedral graphite (RG) to CD and hexagonal graphite (HG) to HD.

The hexagonal and the cubic phases of diamond are not its sole polymorphs. A body centred cubic phase, labelled BC8, is predicted to be stable by, among others, Correas *et al.* [164] and Grumbach and Martin [162] (see Figure 1.43). The latter, as mentioned before, also predict the stability of several liquid carbon phases at high pressures, presenting different local coordination, of which the fourfold one is stable at pressures around 10^2 GPa and lower, while the sixfold one is that typical in the 1–4 $\cdot$ 10^3 GPa range. They also mention, as a theoretical prediction, that one of the liquid phases of carbon is insulating and the other is metallic.

The stability of at least two different liquid carbon phases is also predicted by several other authors [165–167], who speculate about the presence of a metallic liquid carbon phase, whose density depends on the pressure, being equal to 1.2 g cm^{-3} at low pressures and increasing to 1.8 g cm^{-3} at 5.4 GPa at the melting line [168], definitely lower than those of diamond and graphite at low pressures (3.51 and 2.26 g cm^{-3}, respectively). Knudson *et al.* [52]show, using a shock wave technique, a drastic increase in the density of the liquid, up to 7.2 g cm^{-3} at pressures in the 700–1000 GPa range, where liquid carbon is in equilibrium with the diamond and BC8 phases. It should be noted that these densities agree well with those obtained by linear extrapolation of the data reported in Table 1.9.

1.7.8 Silicon Carbide

Silicon carbide (SiC), thanks to its hardness (surface microhardness 2900–3100 kg mm^{-2}: Mohs values 9.2–9.3), second only to diamond (surface microhardness 8–10 $\cdot$ 10^3 kg mm^{-2}:10 on the Mohs scale), is used as an abrasive in cutting tools and is very popular in the silicon semiconductor industry where it is employed (now together with diamond) in the wire sawing technology of single crystal and multicrystalline silicon.

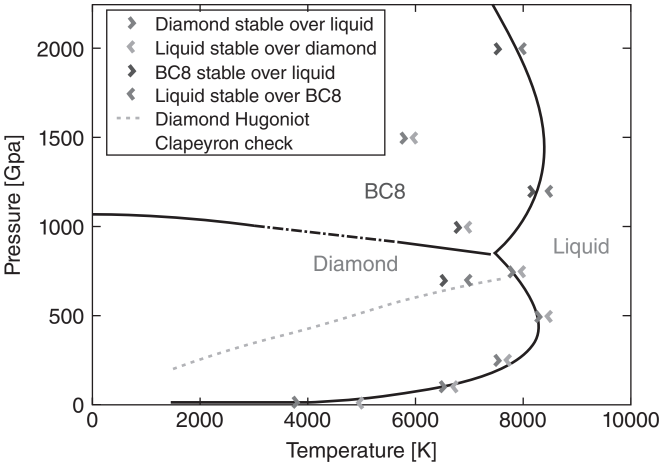

Figure 1.43 *Calculated phase diagram of the carbon system (the graphite phase has been omitted for simplicity). Correa* et al.*, 2006 [164]. Reproduced with permission from National Academy of Sciences, U.S.A*

Table 1.9 *Physical properties of the most common polytypes of silicon carbide*

SiC polytype	Structure	Lattice constant (nm) 300 K	Thermal conductivity (W cm^{-1} C^{-1})	Surface energy (J m^{-2})	Density (g cm^{-3}) 300 K	Heat of formation (kJ mol^{-1})	Energy gap (eV)	Electronic mobility (cm^2 V^{-1} s^{-1})
3C	Cubic:ZB	0.43590	3.6	1.724	3.166	−64	2.36	900
6H	Hexagonal:W	a : 0.3073 b : 1.0053	4.9	1.767	3.211	−63.5	3.23	a:370 b:50
4H	Hexagonal:W	a : 0.3073 b : 1.0053	3.7	1.8	3.21	−66.6	3.0	a:720 b:650

ZB = zinc blende and W = wurtzite.

Since the end of the 1980s, when single crystals of SiC became available, SiC has also been employed as the substrate of high voltage-high power transistors and thyristors, as it offers (see Table 1.10), in comparison with silicon, a lower intrinsic carrier concentration, a higher electric breakdown field and a higher thermal conductivity. It is also used as a substrate for the hepitaxial growth of III–V semiconductors [170–173].

As can be seen in the phase diagram of the C-Si system of Figure 1.34a, SiC is the stable, intermediate phase, which, however, cannot be formed by liquid crystallization techniques as it segregates from the liquid at the peritectic decomposition temperature (3103 ± 40 K and 3.5 MPa), together with carbon.

It could, obviously, be prepared in the polycrystalline form by sintering equimolar quantities of silicon and carbon in a reducing atmosphere at temperatures below the decomposition temperature, although the industrial route, known as the Acheson process, is to react silica (SiO_2) powder with carbon in an electric arc furnace at temperatures between 1600 and 2500 °C.

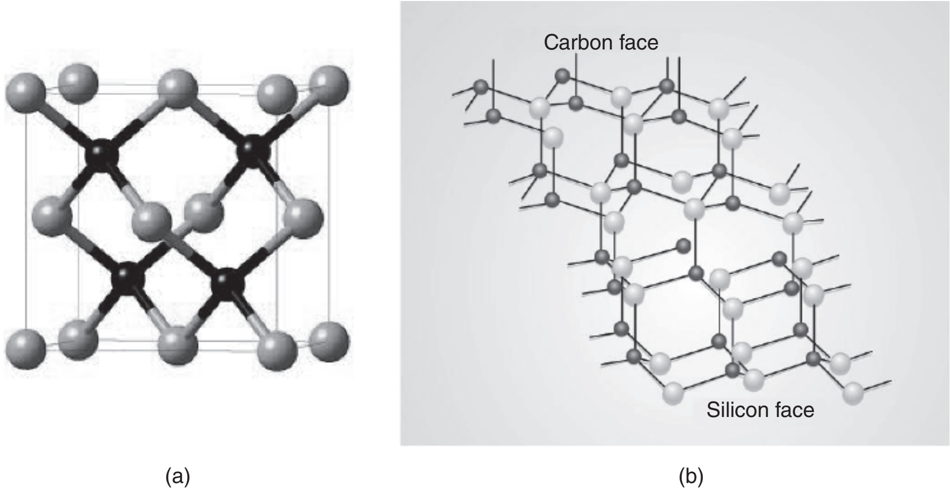

(a) (b)

Figure 1.44 (a) Structure of the cubic SiC Materials Design, 2014.(b) Structure of the 4H-SiC polytype. Madar, 2004 [175]. Reproduced with permission from Macmillan Group

The growth of single crystal samples, which will be described in Chapter 4, is carried out by seeded sublimation, a process often referred to as physical vapour transport (PVT) growth [174]. Seeded crystal growth is needed, as SiC is stable in more than 200 known polytypes, of which only a few are, however, of technological interest.

The polytypism of SiC is a kind of polymorphism which arises from the different order of stacking layers of Si-C tetrahedra in the SiC lattice. Three types of layers exist, labelled A, B, C, which allow a comfortable packing, and the difference between the different polytypes depends on the stacking sequence adopted. As an example, the common 6H-SiC polytype is formed by an infinite repetition of the sequence ABCACB and the cubic 3C-SiC results by an infinite repetition of the sequence ABC, see Figure 1.44.

Some structural and thermodynamic properties of the most common SiC polytypes [176] are reported in Table 1.9. The Gibbs energy of formation of 3C- and 6H-silicon carbide was determined electrochemically between 1623 and 1898 K [177] by measuring the silicon solubility in liquid gold in equilibrium with a mixture of silicon carbide and graphite. The behaviour of the Au-Si system provides a wide compositional range for the small difference in the activity of silicon exhibited by the two polytypes, thus offering greater experimental precision over previous similar methods. For 6H-SiC, a Gibbs free energy value ΔG (kJ mol^{-1}) = $-116\,900(\pm 7.2) + 38.2(\pm 4.1)T$ was obtained.

Major problems in the operation of SiC-based electronic devices arise from perturbations of the ideal layer stacking, with the formation of stacking faults, which are known as the origin of deterioration of SiC devices after long operation periods. This issue will be discussed in Chapter 3.

1.7.9 Selenium-Tellurium Alloys

In spite of more than half a century of investigations, the properties of the Se-Te system remain not entirely settled. The full miscibility of their hexagonal structures has been demonstrated, as well as the formation of a lens-shaped isomorph-type phase diagram, which calls for ideality of both solid and liquid solutions (see Figure 1.45).

The properties of the solid solutions were studied by Pattanaik *et al.* [178], who estimated the energy of the single covalent Se-Te bond, as 201.1 kJ mol^{-1}, on the basis of the literature values for the Se-Se (206.1 kJ mol^{-1}) and Te-Te (158.8 kJ mol^{-1}) bond energies [179], see also Table 1.10 [169].

Table 1.10 *Bond energies of selected pairs*

Bond	Bond energy (eV)	Bond	Bond energy (eV)	Bond	Bond energy (ev)
Ge-Ge	2.13	Ge-Se	2.44	Bi-Te	1.69
As-As	2.07	Ge-Te	1.87	Pb-S	2.55
Sb-Sb	1.55	As-S	2.48	Pb-Se	2.40
Bi-Bi	1.32	As-Se	2.26	Pb-Te	1.90
Pb-Pb	0.89	As-Te	1.99	Sn-Se	2.36
Sn-Sn	1.57	As-Sb	2.06	Sn-Te	1.86
S-S	2.69	Sb-Se	2.25	Se-Te	2.00
Se-Se	2.14	Sb-Te	1.73		
Te-Te	1.65	Bi-Se	2.17		

Rao and Mohan, 1981, [69]. Reproduced with permission from Elsevier.

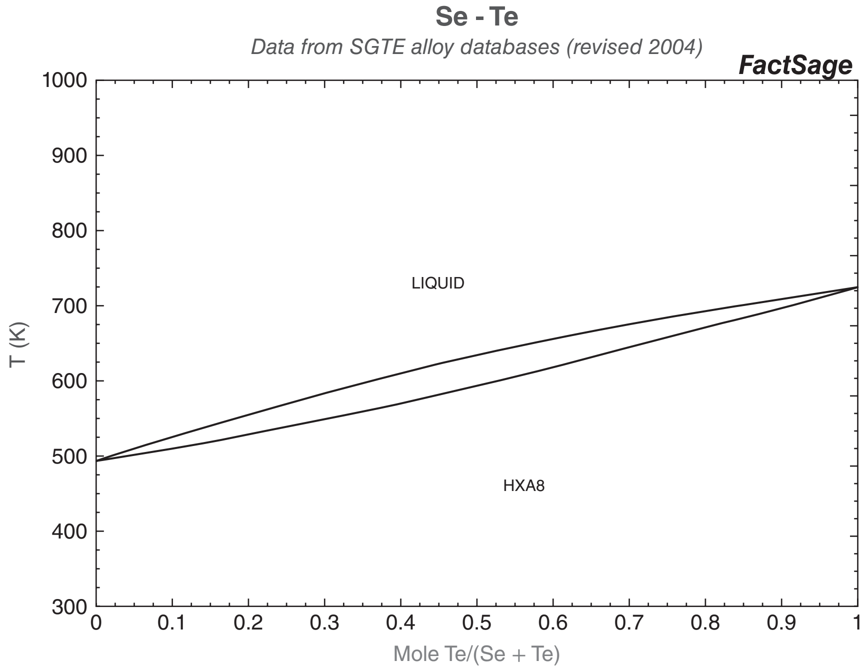

Figure 1.45 *Phase diagram of the Se-Te system. Scientific Group Thermodata Europe (SGTE). Reproduced with permission from SGTE*

The problem here is that the Se-Te bond has a partial heteropolar character [180] and, therefore, a simple chemical model could not be directly applied for evaluation of the interaction coefficient. Within this uncertainty, the interaction coefficient takes a value $\Omega = -18.55$ kJ mol^{-1}.

The thermodynamics of the liquid solutions are even more difficult to be settled, because the Se-Te solutions present a semiconductor character at high Se concentrations and undergo a transition to metallic character above 80% Te [181]. Qualitative information concerning the bond energies in the liquid phase might be inferred from the properties of calchogenide Bi-Se-Te glasses, considered as metastable liquids, from which a value of 1.43 eV for the Te-Te pair, 1.89 eV for the Se-Se pair and 1.87 eV for the Se-Te pair might be deduced [182].

From these values the interaction coefficient in the liquid solutions Ω^l might be estimated to range around 0.225 eV or 21.701 kJ mol^{-1}, within the errors of the bond energies [182]. Both the solid and the liquid solutions, therefore, have non-ideal behaviour.

The good fit with Vegard's law observed for the lattice distances along the *c*-axis in contrast with deviations observed along the *a*-axis, see Figure 1.46 [183] are issues which offer additional information on the overall physico-chemical behaviour of this system. The deviations along the *a* axis have been tentatively explained [183] considering that the chain structure of these materials would make the description of the microscopic structure of the Se-Te alloys different from that of conventional systems, where a simple substitutional or interstitial solution would form. The hypothesis was suggested that the formation of chains containing Se-Te covalent bonds, aligned along the *a*-axis, is favoured against that of homogeneous chains formed only by Se and Te atoms, in view of the larger energies of the Se-Te bonds.

1.7.10 Binary and Pseudo-binary Selenides and Tellurides

Sulfides, selenides and tellurides of Group II elements (Cd, Zn, Hg) are families of binary and pseudo-binary compound semiconductors of relevant scientific and technological interest, of which the selenides and tellurides are the most important.

As an example, thin film CdTe is a material of excellent photovoltaic properties [184, 185] in terms of efficiency, cost and pay-back time, in spite of the environmental problems

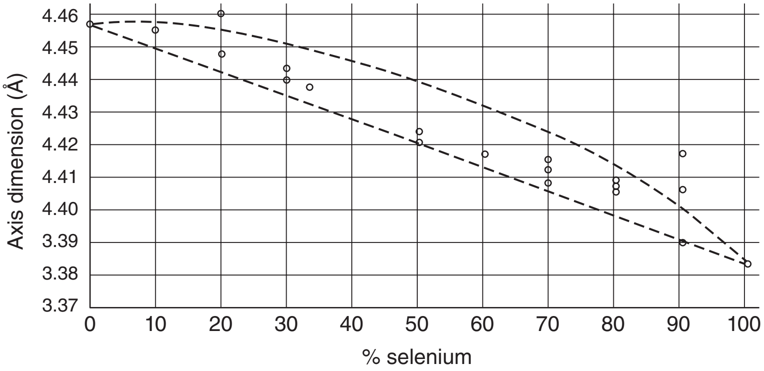

Figure 1.46 *Plot of the lattice constant, a, of Te-Se alloys as a function of the alloy concentration. Grison, 1951, [183]. Reproduced with permission from AIP Publishing*

associated with the toxicity of Cd and Se and Cd vapours or CdO spills in the case of fire. On the other hand, CdZnTe (CZT) is unrivalled for IR, X-rays and γ-detectors [186–189] and is also used as a lattice-matched substrate for the epitaxial growth of HgCdTe, another widely employed semiconductor used for the fabrication of detectors in the long-wavelength infrared spectral region.

Thin films of CuInSe (CIS) and of quaternary alloys belonging to the same family are strong competitors of CdTe as photovoltaic materials, in virtue of their high photovoltaic efficiency[10] and for being Cd-free and thus avoiding the main drawback of CdTe.

It will be shown in Chapter 3 that a problem concerning these materials is their ingot growth, which requires a proper control of the growth atmosphere, considering that the melt consists of highly volatile components. In the case of the growth of Cd_{1-x} Zn_xTe crystals, as an example, one has a steady loss of the constituents from the vapour phase above the melt or through the porous walls of the crucible during the growth. The loss of the constituents might be suppressed by the application of an external, inert gas pressure, typically ≈ 15 GPa of argon.

Since Cd has the highest vapour pressure among the Cd ZnTe melt constituents, the vapour phase predominantly consists of Cd atoms. Although the external Ar pressure greatly reduces sublimation, it does not completely eliminate Cd loss from the crucible [190], which induces the formation of non-stoichiometric deviations and the presence of Cd-vacancies and Te-antisites in the crystal lattice, as will be discussed in Section 2.4.3.

Knowledge of the pressure–temperature–composition $(P - T - x)$ phase equilibria gives, therefore, the necessary thermodynamic basis for the crystal growth of materials with controlled composition.

As an example, detailed studies of the $P - T - x$ phase diagram for the Cd-Te system and of the non-stoichiometry in CdTe have been reported [191, 192] and information on the vapour pressure measurement and estimates of solubility of the components in ZnTe are also available [193, 194].

A key property of these semiconductors is the presence of a second order transition between their stable cubic zinc blende phase and the hexagonal wurtzite phase (Figure 1.47) [195] and a further transition to a NaCl structure at pressures of the order of several GPa [196].

Polytype formation is proposed to be associated with the effect of a progressive distortion of the lattice due to the addition of ordered staggered layers and to internal-rotation forces, while configurational and vibrational entropy effects are not found to contribute to the stabilization of polytype lattices [195]. Two typical examples of this kind of phase transition will be given at the end of this section.

The challenges with the thermodynamic study of II–VI and IV–VI compounds are the marked deviations from the ideality of the liquid solutions, which cannot be accounted for by the QCA nor by the pseudo-regular solution model, based on the assumption of a linearly temperature-dependent interaction coefficient $\Omega(T)$. In these systems the large difference in electronegativity produces more ionic and stronger interactions among unlike atoms, evidenced by the onset of liquid immiscibility and by a step temperature peak in correspondence to the melting temperature of binary systems, as shown in Figure 1.48 [197].

---

[10] According to a January 2013 press release, EMPA, the Swiss Federal Laboratory for Materials Science and Technology, achieved a record efficiency of 20.4% with CIGS on polymer foils.

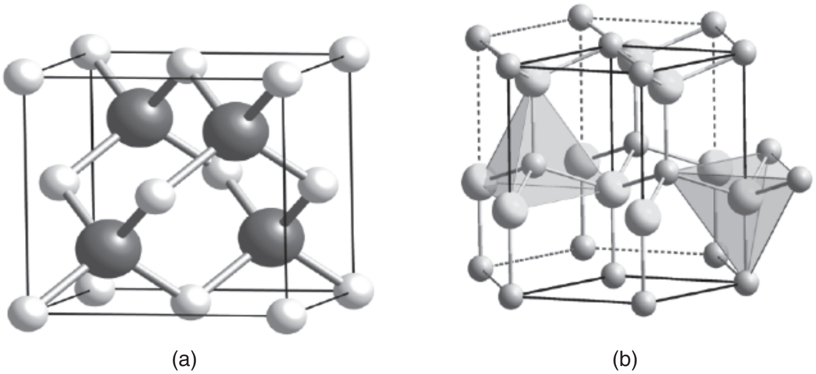

Figure 1.47 *(a) Zinc blende structure B. Mills and (b) wurtzite structure. Solid State*

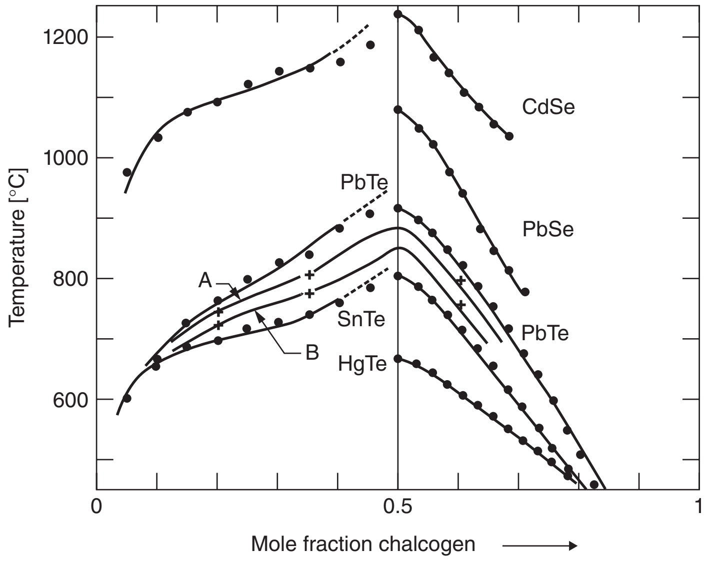

Figure 1.48 *Liquidus lines of some binary II–VI systems. Laugier, 1973, [197]. Reproduced with permission from EDP Sciences*

Better results were obtained using the so-called surrounded atoms model, in which the basic entity is an atom surrounded by all its neighbours, not a simple atom pair or the associated solution model, postulating the existence of stable complexes, and the polyassociative model, postulating the stability of a multiplicity of complexes in solution [198, 199], each of them representing an attempt at a better themodynamic description of the studied system.

Later in this section will be seen the advantages of these techniques, after having gained insight on some details of the phase diagrams of II–VI compounds.[11]

---

[11] A recent comprehensive analysis has been given by Adachi [200].

A number of II–VI semiconductors (CdTe, CdS, CdSe, PbTe, SnTe, to mention only the most important from the viewpoint of their technological applications) but also GaAs and InP, present significant deviations from the stoichiometry, whose onset might be described with the following defect reactions, taking CdTe as an example

$$\mathrm{Cd_{Cd}} \rightleftharpoons \mathrm{Cd^g} + \mathrm{V_{Cd}} \tag{1.100}$$

$$\mathrm{Te_{Te}} + \mathrm{Cd_{Cd}} \rightleftharpoons \mathrm{Te_{Cd}} + \mathrm{Cd^g} \tag{1.101}$$

$$\mathrm{Te_{Te}} \rightleftharpoons \mathrm{Te_i} + \mathrm{V_{Te}} \tag{1.102}$$

and whose extent depends on the Gibbs free energy of formation of the different point defects [201], as will be seen in Chapter 2.

Although the deviations from the stoichiometry are generally modest, and range between $\pm 10^{-4}$ molar fraction for GaAs and $\pm 10^{-3}$ for PbTe, their growth from the melt could be troublesome, as will be seen in Chapter 4.

The phase diagram of CdTe is reported in Figure 1.49 as a typical example. One can see in Figure 1.49a that the solid melts congruently [199, 202] but exhibits marked non-stoichiometry with decreasing temperature (see Figure 1.49b), below the melting point, with a maximum Te-excess around 1000 °C [201, 203].

It is also interesting to mention that the substitution of Se with S leads to an improvement in the stoichiometry [203]. This effect plays a beneficial role in photovoltaic materials based on Cd compounds and depends on the different Gibbs energy of formation of Cd vacancies in CdS and CdSe, as will be discussed in Chapter 2. Both defects are deep level and responsible for minority carriers lifetime degradation effects.

The phase diagrams of CdSe, ZnSe and ZnTe show close topologies with congruent melting and liquid immiscibility features [204–206], which has stimulated the interest of many authors [207–209] in the updating of the thermodynamic properties of these alloys.

As anticipated above, the problem found in the theoretical analysis of these binary systems is the description of the liquid phases, which behave neither as regular nor pseudo-regular solutions.

Good results were, however, obtained in the case of ZnTe using the polyassociative model, as shown in Figure 1.50 [206], where the calculated points are superimposed on the experimental diagram [205], in spite of some crude assumptions on the equilibrium partial pressures of Zn and Te.

The basic approach of this model is to consider the presence in the liquid solution of undissociated Zn and Te together with the complexes ZnTe, $\mathrm{Zn_2Te}, \mathrm{Zn_2Te_3}, \mathrm{ZnTe_2}$. Each complex has a dissociation constant $K_{xy}(T)$, which in the case of the complex $\mathrm{Zn}_p\mathrm{Te}_q$ could be written [206]

$$K_{pq}(T) = \frac{x^q_{\mathrm{Zn}} x^p_{\mathrm{Te}}}{x_{\mathrm{Zn}_p\mathrm{Te}_q}} \tag{1.103}$$

(where $x^q{}_{\mathrm{Zn}}$ and $x^p{}_{\mathrm{Te}}$ are the molar fractions of the undissociated Zn and Te in solution) which can be calculated using numerical procedures on the basis of the experimental values of the vapour pressures of Zn and Te.

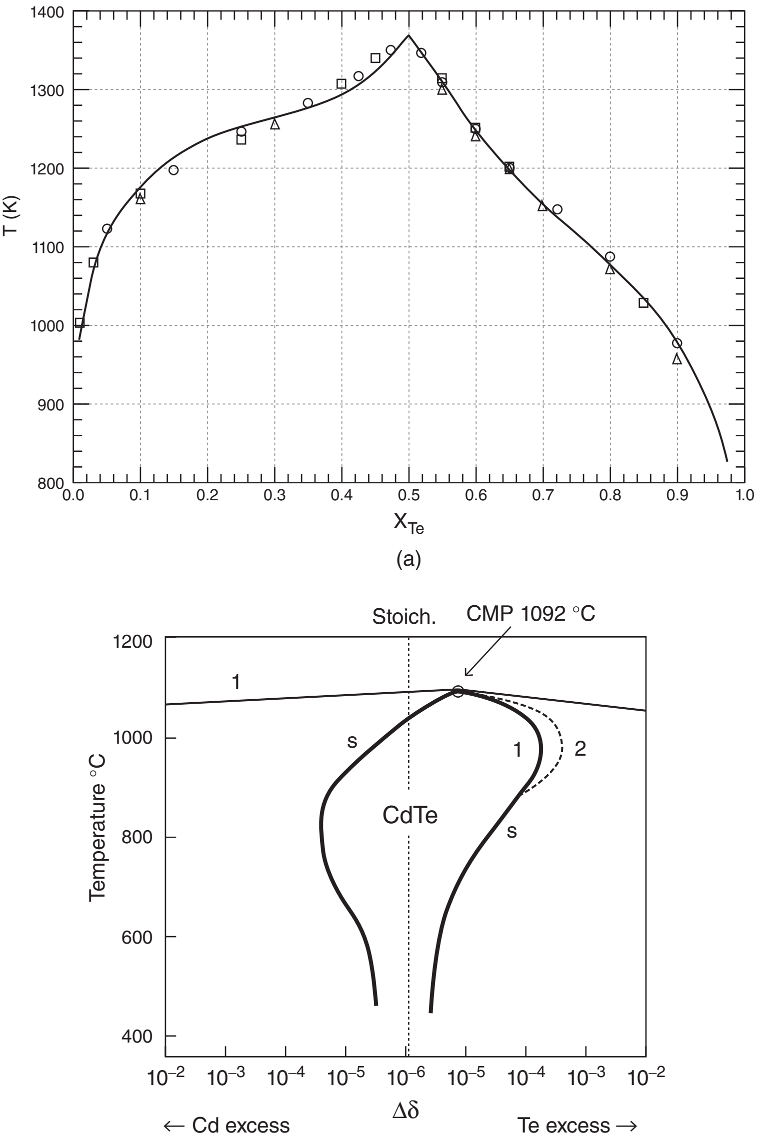

(a)

(b)

Figure 1.49 *(a) Phase diagram of Cd-Te system. Brebrick, 2010, [199]. Reproduced with permission from Elsevier. (b) Non-stoichiometry of the CdTe phase. Rudolph, 2003, [201]. Reproduced with permission from John Wiley & Sons*

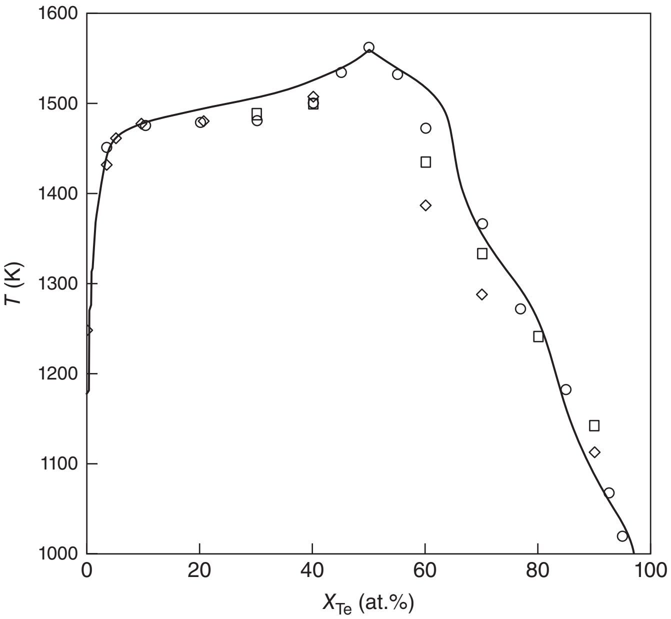

Figure 1.50 *Phase diagram of the Zn-Te system. Moskvin,* et al.*, 2011, [206]. Reproduced with permission from Centrum Informatyczne TASK*

The concentration of the complexes in solution is related to the overall concentration of the components in solution via mass balance equations and the T, x phase equilibrium is defined by the equation [206]

$$\Delta S^{f}_{ZnTe}\left(\frac{T^{f}_{ZnTe} - T}{RT}\right) + \ln\frac{x_{Zn}x_{Te}}{x^{soln}_{Zn}x^{soln}_{Te}} = 0 \tag{1.104}$$

where ΔS^{f}_{ZnTe} is the entropy of fusion of ZnTe and $T^{f}{}_{ZnTe}$ is the melting temperature of $Zn_{(1\pm x)}Te_x$ for a couple of values of $x^{soln}{}_{Zn}$ and $x^{soln}{}_{Te}$ in the liquid solution. Eventually, the experimental data relative to the temperature dependence of the vapour pressures of Zn and Te in equilibrium with the solid solution, under the assumption that only the free (dissociated from the complex) Zn and Te atoms determine the vapour pressure, allows one to obtain the dissociation constants for the ZnTe, Zn_2Te, Zn_2Te_3 and $ZnTe_2$ complexes and thus the phase equilibria.

Using the associated solution model, a simpler version of the polyassociative model, the dissociation coefficients β of a number of binary systems exhibiting complete miscibility in the liquid and solid state were also calculated [197]. The results are shown in Table 1.11, from which it is possible to conclude that 100% association in the liquid state occurs in most cases, except binaries involving tellurium (PbTe, SnTe and CdTe).

The values of the interaction coefficients Ω in Table 1.11 were instead evaluated by fitting the experimental solidus curves with the equations describing the solid–liquid equilibria, showing that CdTe, CdSe, SnTe and PbTe present the largest interaction coefficients and, therefore, the largest deviations from ideality.

Table 1.11 Interaction parameter Ω and dissociation coefficient β of the stoichiometric liquids according to the associated solution model

System	ZnTe (Te-rich)	ZnTe (Zn-rich)	CdTe (Te-rich)	CdTe (Cd-rich)	HgTe (Te-rich)	PbTe (Te-rich)	PbTe (Pb-rich)	SnTe (Te-rich)	SnTe (Sn-rich)	PbSe (Se-rich)	CdSe (Se-rich)	CdSe (Cd-rich)
Ω (kJ mol^{-1})	7.95	71.1	7.11	45.6	0	−25.94	23.01	−13	35.56	−39.33	32.64	50.2
β	0.00	0.065	0.00	0.055	0.04	0.04	0.14	0.04	0.10	0.00	0.02	0.12

For a completely dissociated liquid $\beta = 1$ and in this case Ω corresponds to the interaction coefficient of a regular solution [197].

Laugier, 1973, [197]. Reproduced with permission from EDP Sciences.

Table 1.12 Regular solution interaction coefficients for some pseudo-binary solid solutions

System	Melting temperature range (K)	Ω (kJ mol^{-1})
ZnTe-CdTe	1560 to 1365	5.60
ZnTe-HgTe	1560 to 943	13
ZnSe-ZnTe	1803 to 1560	6.48
CdTe-HgTe	1365 to 943	5.86
CdSe-CdTe	1528 to 1365	6.28
HgSe-HgTe	1073 to 943	2.93
PbSe-PbTe	1353 to 1200	6.28
PbTe-SnTe	1200 to 1080	0.73
MnTe-GeTe	1430 to 1013	3.38

Laugier, 1973, [197]. Reproduced with permission from EDP Sciences.

It should be noted that the actual interaction coefficient value and sign may depend on the stoichiometry of the melt, while here only metal-rich alloys were considered.

Using the regular solution model, the temperature-independent interaction coefficients Ω were also calculated for several pseudo-binary systems [197]. The results are reported in Table 1.12, which shows that all these systems present positive deviations from the ideality.

The phase diagram of the $Cd_{1-x}Zn_xTe$ system is reported in Figure 1.51 [210, 211].The high-temperature section of the phase diagram (Figure 1.51a) has been fitted, taking for the interaction coefficient of the solid solutions a value of $\Omega^s = -0.33$ kJ mol^{-1}, deduced from electrochemical measurements of the Gibbs energy of mixing and a value of $\Omega^l = 0.21$ kJ mol^{-1} for the liquid from a best fitting procedure of the liquid line.

This conclusion contradicts the occurrence of a solubility gap at low temperatures (Figure 1.51b) which would require a positive value of Ω^s, as that reported in Table 1.12. This conclusion is also in contradiction with the results of the concentration dependence of the Gibbs energy of mixing, reported in Figure 1.52, which show a small negative excess of Gibbs energy of mixing over the ideal one, calling for negative values of Ω^s [212].

In conclusion, the accuracy of the thermodynamic data available for this system and the use of regular solution approximations does not allow a reasonable fit of the phase diagram of this system, which, however, presents features very close to ideal. This conclusion is well supported by the rather close lattice parameters of CdTe and ZnTe (see Table 1.13), which

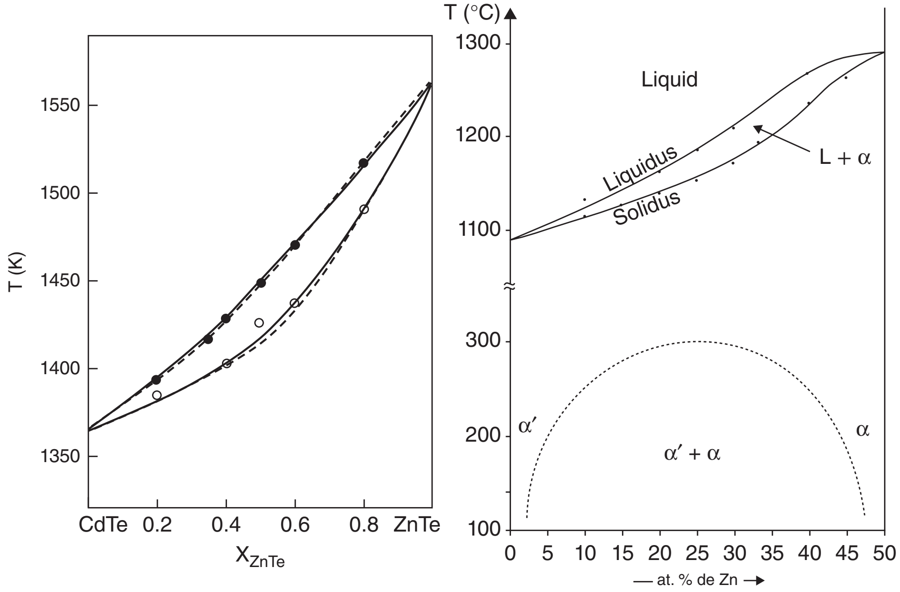

(a) (b)

Figure 1.51 *(a) High-temperature section of the phase diagram of the* $Cd_{1-x}Zn_x$ *Te system. Zabdyr, 1984, [210]. Reproduced with permission from Electrochemical Society. (b) Phase diagram of the* $Cd_{1-x}Zn_x$*Te system including the low-temperature biphasic region. Haloui* et al.*, 1997, [211]. Reproduced with permission from Elsevier*

Table 1.13 *Physical properties of sulfides, selenides and tellurides of Cd, Zn and Hg*

	CdS	CdSe	CdTe	ZnS	ZnSe	ZnTe	HgSe	HgTe
T_m (K)	2023 (100 atm)	1623	1314	2123 (150 atm)	1373	1513	1063	943
Structure	ZB	ZB	ZB	ZB[a]	ZB	ZB	ZB	ZB
Lattice constant (nm)	0.582	0.608	0.648	0.541	0.567	0.610	0.6085	0.6453
Structure	W[b]	W[b]	—	W[a]	—	—	—	—
a (nm)	0.4135	0.430	—	0.3811	0.398	0.427	—	—
c (nm)	0.6749	0.702	—	0.6234	0.653	0.799	—	—
Energy gap (eV)	2.5 (direct)	1.714 (direct)	1.474 (direct)	3.91 (direct)	2.82 (direct)	2.39 (direct)	8[c]	0.01–0.02

[a] Both zinc blende (ZB) and W phases are stable.
[b] Wurtzite (W) is the stable phase.
[c] HgSe is a semimetal with a valence and conduction overlap of 0.07 eV.

lead us to assume a negligible influence of elastic energy contribution to the free energy of mixing, which should be dominated by the contribution of complexes in solution.

The very symmetric phase diagram of the ternary $Hg_{1-x}Cd_xTe$ alloys is reported in Figure 1.53 which exhibits the typical features of ideality of both the liquid and solid solutions [213], in good agreement with the structural data of the components (see Table 1.13).

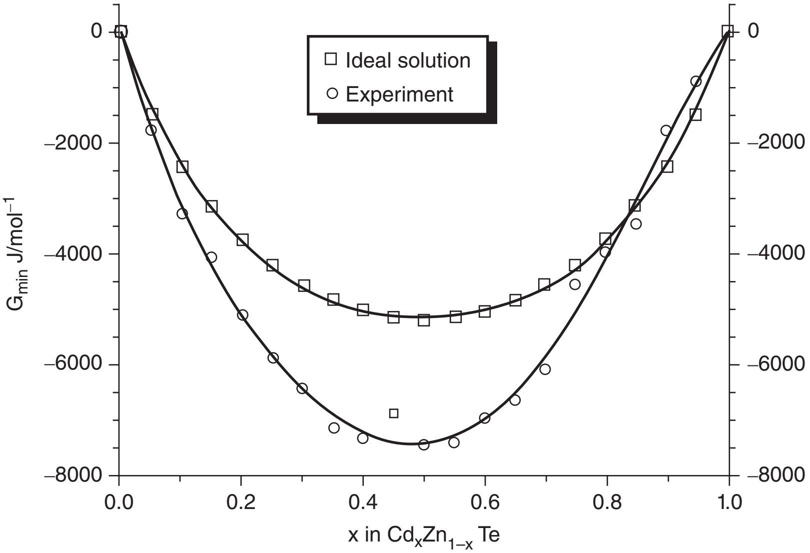

Figure 1.52 *Gibbs free energy of mixing of the CdZnTe system at 900 K. Alikhanian* et al.*, [212]. Reproduced with permission from Elsevier*

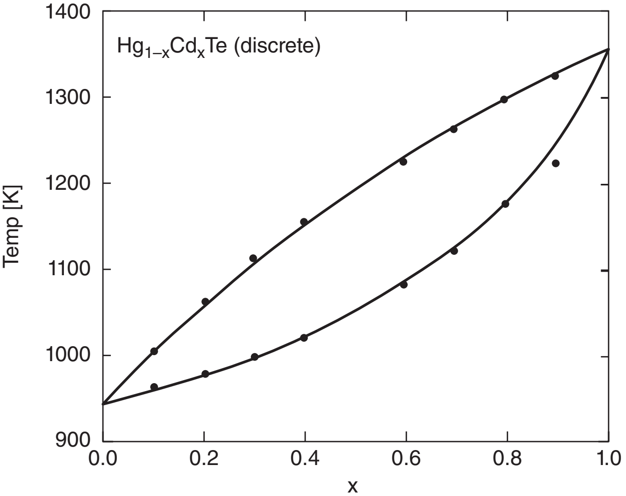

Figure 1.53 *Phase diagram of the* $Hg_{1-x}Cd_xTe$ *system. Patrick* et al.*, 1988, [213]. Reproduced with permission from AIP Publishing*

Also in this case the thermodynamic data of Table 1.12 indicate only close to negligible deviations from the ideality of the solid solutions, with a value of the interaction coefficient $\Omega = 5.6\ \text{kJ mol}^{-1}$.

A complementary approach to the analysis of these systems is to consider the role of the polytype equilibria relative to the binaries CdS, CdSe and ZnS on the structure of the corresponding pseudo-binary solutions.

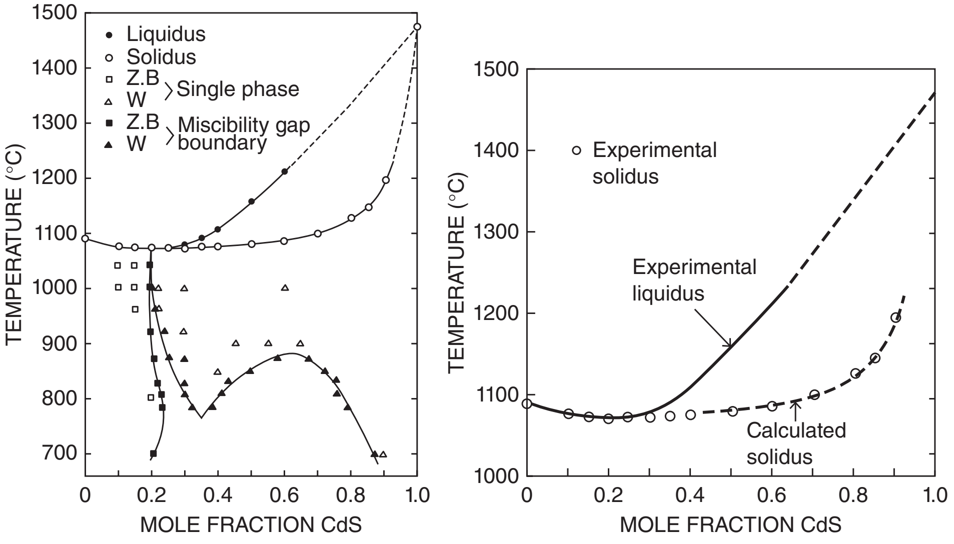

(a) (b)

Figure 1.54 *Phase diagram of the CdS-CdTe system (a) experimental phase diagram (b) calculated under the approximation of Eq. (1.95) for the excess strain energy. Ohata,* et al.*, 1973, [215]. Reproduced with permission from The Japan Society of Physics*

As an example, room-temperature lattice parameters of the systems CdZnTe and CdTeSe, measured over the full range of their solid solutions, show that the CdZnTe system remains cubic over its whole range of compositions, while the CdTeSe system shows a transition from the cubic phase to the hexagonal wurtzite structure at high Se contents [214].

A more significant example is given by the system CdS-CdTe [215, 216]. As shown in Figure 1.54, the structure of the CdTe-rich solid solutions is cubic (zincblende) but is hexagonal (wurtzite) at high CdS concentrations. In correspondence with the minimum at 1071 °C the zinc blende–wurtzite boundary coincides. At this temperature there is also the onset of a miscibility gap, whose size increases with decreasing temperature. Ohata *et al.* [215] succeeded in accounting for the thermodynamics of this system by considering that the S-Te bond is not the nearest bond and that the S-Te repulsive energy should not be too high, whereas the strain energy should be expected to be very large in view of the large difference in the covalent radii of S (0.105 nm) and Te (0.136 nm).

As in this system Vegard's law was demonstrated to hold both for the zinc blende (ZB)-type and W-type of solutions, the strain energy contribution W to the mixing enthalpy was evaluated by assuming the validity of Hooke's law over the whole range of compositions. Within these crude approximations we have

$$L_{\mathrm{x}} = L_{\mathrm{A}} x_{\mathrm{A}} + L_{\mathrm{B}} x_{\mathrm{B}} \tag{1.105}$$

$$W = {}^{1}\!/_{2}\, k\, x_{\mathrm{A}}(L_{\mathrm{x}} - L_{\mathrm{A}})^2 + {}^{1}\!/_{2}\, k\, x_{\mathrm{B}}(L_{\mathrm{x}} - L_{\mathrm{B}})^2 = {}^{1}\!/_{2}\, k\, (L_{\mathrm{A}} - L_{\mathrm{B}})^2 x_{\mathrm{A}} x_{\mathrm{B}} = {}^{1}\!/_{2}\, k\, x_{\mathrm{A}}(1 - x_{\mathrm{A}}) \tag{1.106}$$

where L_x is the average lattice parameter of the solid solution and L_A and L_B are the corresponding lattice distances in CdS and CdTe, leading eventually to the equation

$$\Delta H^s = C\,x(1-x) \tag{1.107}$$

for the strain contribution ΔH^s to the mixing enthalpy, where C is a fitting constant taken equal to 17.11 kJ mol^{-1}. A good fitting of the solidus curve over the whole range of compositions was obtained, as shown in Figure 1.54b.

It should be remarked that the composition dependence of the strain-induced enthalpy of mixing of Eq. (1.107) is formally equivalent to that of the enthalpy of mixing of a regular solution Eq. (1.89).

This formal equivalence shows that the interaction coefficient Ω of a system which follows the regular solution model may contain an elastic contribution which adds to the chemical energy terms or even dominates the interaction, in the approximation of validity of Hooke's law. Therefore, it would be misleading to deduce from the experimental evidence of a quadratic dependence of the enthalpy of mixing on composition a true regularity, as this quadratic dependence is a pure phenomenological law.

1.7.11 Arsenides, Phosphides and Nitrides

The success of modern optoelectronics and the potential of SSL for general illumination is closely related to the use of III–V compounds, to the development of specific technologies for their growth and processing and to a half century of dedicated research.

The availability of lasers and LEDs emitting in a bright range of wavelengths, from the mid-IR to the near-UV and of HEMTs (high electron mobility transistors) working in the gigahertz to terahertz range, is eminently due to the peculiar electronic properties of these compounds. They present direct gap features and high electronic mobilities (see Table 1.14), with a peak at $7.7 \cdot 10^4$ ($cm^2\ V^{-1}\ s^{-1}$) in the case of InSb, and, therefore, different from silicon and germanium, which are indirect gap semiconductors, presenting efficient light emission capabilities over a wide range of wavelengths.

Arsenides and phosphides were the first direct gap semiconductors used for micro- and opto-electronic purposes, because their melting properties are not so extreme as those of the nitrides, but they still present problems for their bulk single crystal growth due to their large decomposition pressures [46, 217, 218]. The benefits of GaAs and other III–V compounds over silicon for optoelectronic applications are similar to those given by the use of silicon instead of germanium as a transistor material [219].

However, though the GaAs transistor performance is better than that of silicon, silicon is still the material of choice for applications where physics is not against it, as is the case of SSL, and will probably remain unrivalled for the years to come until Moore's law will reach its limit at the silicon atoms size.

Among III–V compounds, Group III nitrides (InN, GaN, AlN and their alloys) are unique, because they share the benefits of a wide, direct gap range (6.2, 3.4 and 0.7 eV for AlN, GaN and InN, respectively) and strong chemical bonds. They share also the drawback of high melting temperatures (2500 °C for GaN) and high decomposition pressures (45.000 bar for GaN) that make their direct crystallization from liquids practically impossible. These drawbacks hindered for years their growth in single crystalline form,

Table 1.14 *Physical properties of III–V compounds of technological interest*

	GaAs	InAs	InP	InSb	GaP	InN	GaN	AlN	Si
T_m (K)	1523	1215	1333	800	1738	2173[a]	2773[a]	3473[a]	1688
P_{eq} (atm)	15	<1	<1	—	30	> 60.000 [b]	45.000[b]	200[b]	—
Band gap (eV)	1.424	0.354	1.344	0.17	2.24	0.7[c]	3.44	6.2	1.12
μ_e ($cm^2\ V^{-1}\ s^{-1}$)	8500	$4 \cdot 10^4$	5400	$7.7 \cdot 10^4$	<250	3200	<1000	300 (calc)	1400
μ_h ($cm^2\ V^{-1}\ s^{-1}$)	<400	$5 \cdot 10^2$	<200	≤850	150	—	<350	14	<450
Structure	ZB	ZB	ZB	ZB	ZB	W	W	W	Diamond
Lattice constant (nm)	0.5653	0.6058	0.5869	0.6479	0.5450	$a = 0.35446$ $c = 0.57034$	$a = 0.3187$ $c = 0.5186$	$a = 0.311$ $c = 0.4982$	0.5430

For comparison the properties of silicon are also reported.

[a] Calculated.

[b] Extrapolated.

[c] The energy gap value of InN is still under discussion.

ZB = zinck blende and W = wurtzite.

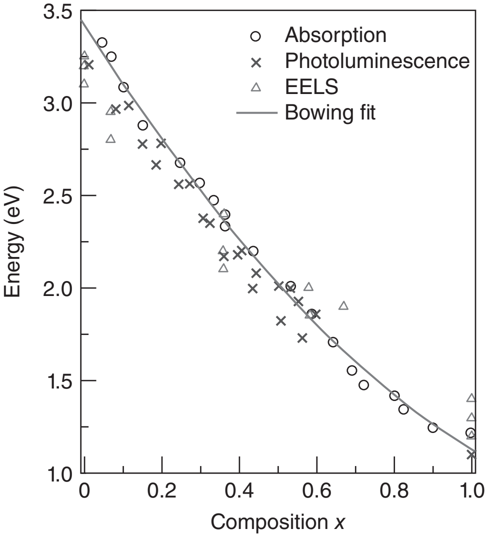

Figure 1.55 *Band gap of* $In_{1-x}Ga_x$ N *nanowires as a function of the gallium concentration. Kuykendall,* et al.*, 2007, [221]. Reproduced with permission from Macmillan Publishers*

needed for their use as substrates for microelectronic and optoelectronic devices since the discovery of Nakamura *et al.* in 1986 [220], who succeeded in the heteroepitaxial growth of crystalline multilayer structures of InGaN using MOCVD on a GaN buffer layer deposited on a sapphire substrate.

The GaN buffer layer has the scope to reduce the lattice misfit, which would be intolerable in the case of the direct growth of ternary nitrides on sapphire or SiC, being the origin of exceedingly high dislocation densities.[12]

The value of a GaP-buffer layer is particularly evident in the case of the $Al_{0.83}In_{0.17}N$ alloy, as the GaN-buffer is lattice-matched and allows deposition of a low dislocation density material.

Today small single crystals of GaN might be grown in high pressure furnaces or autoclaves,[13] but all the nitride devices present in the market are manufactured from GaN substrates grown heteroepitaxially on sapphire, 6H SiC and, more recently, on silicon.

Blue, nitride-based LEDs working as a pump for suitable phosphors show promise for the solid state lamps which will be used in the next decade for general illumination. An additional advantage of nitrides is that the $In_xGa_{1-x}N$ solutions allow the complete tunability of the light emission from the near-UV to the near-IR region by changing the composition, as seen in Figure 1.55 for the case of InGaN nanowires [221], but this feature is typical also of InGaN thin films.

The discussion on the understanding of the physico-chemical properties of these systems and the modelling of their phase diagrams is carried out in the next section, while their growth processes are discussed in Chapter 3.

---

[12] The effect of dislocations on the electronic properties of semiconductors will be discussed in Chapter 3.

[13] Details about growth processes of bulk GaN will be discussed in Chapter 3 [217].

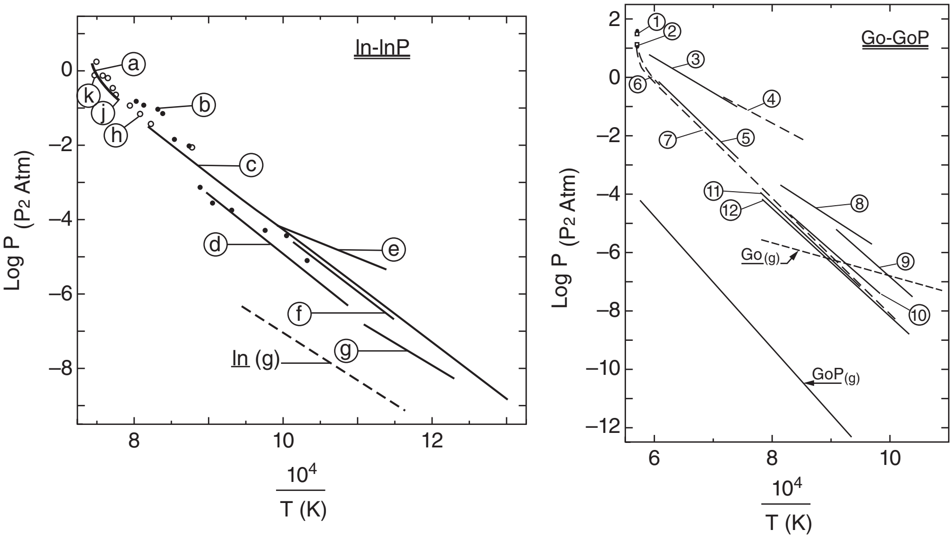

(a)

(b)

Figure 1.56 *Equilibrium vapour pressures of* P_2 *(solid line), In (dotted line) and Ga over (a) the In-InP and (b) the Ga-GaP systems. For the references indicated in the figures see original paper. Tmar* et al.*, 1984, [217]. Reproduced with permission from Elsevier*

1.7.11.1 Phosphides

Concerning the basic thermodynamic properties of phosphides, they exhibit, in general, high saturation pressure values, with their consequent decomposition if the system is not properly overpressurized. In what follows, only the properties of the binary In-InP and Ga-GaP and ternary InGaP systems will be discussed, since their properties are typical for all phosphide phases.

The equilibrium partial pressures of P_2 over InP and GaP are reported in Figure 1.56, while their binary phase diagrams are reported in Figure 1.57, which shows that only the intermediate stoichiometric phases segregate from the In-rich melts [217].

The phase diagram of the pseudo-binary $Ga_xIn_{1-x}P$ system [222] is reported in Figure 1.58. The properties of this system are dominated by the large elastic energy required to overcome the lattice mismatch (see Table 1.14) of the pure components [223], which results in the opening of a miscibility gap below a critical temperature of 923.7 K at $x_c = 0.6$ according to [222] (or 830 K at $x_c = 0.4$), in good agreement with the results of a theoretical evaluation [223].

Another key feature of this system is the calculated and experimental bimodal distribution of bond lengths (see Figure 1.59) at 1000 K, a temperature at which, according to the phase diagram of Figure 1.58, the alloy is homogeneous. The solid lines were calculated using a Monte Carlo simulation [223] which also indicates a random distribution of metallic atoms in the alloy. Here, as in the case of the Si-Ge alloys, the individual bond lengths maintain values close to those of the pure compounds and very different from the Vegard's law values of the lattice distances (dotted line).

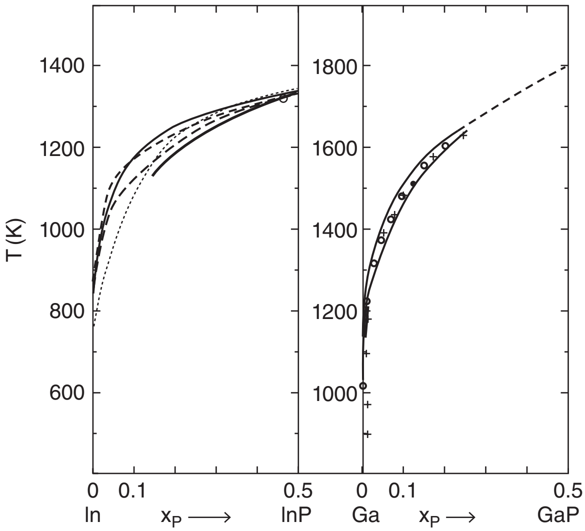

Figure 1.57 *Phase diagrams of the In-InP and Ga-GaP systems under their own equilibrium vapour pressures. Tmar* et al.*, 1984, [217]. Reproduced with permission from Elsevier*

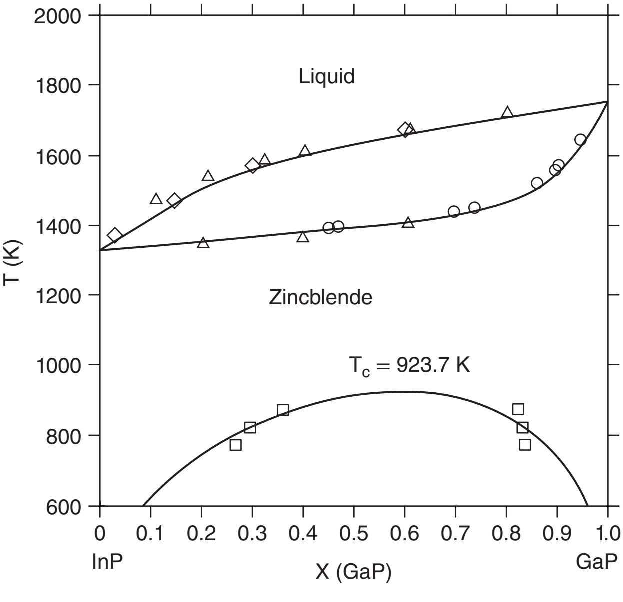

Figure 1.58 *Phase diagram of the pseudo-binary* Ga_xIn_{1-x} P *alloys. Ch-Li* et al.*, 2000, [222]. Reproduced with permission from ASM International*

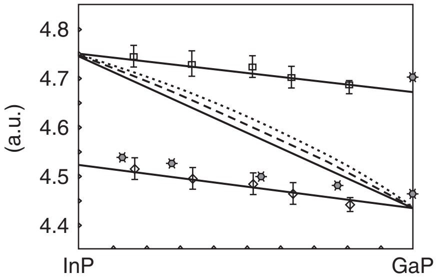

Figure 1.59 *Calculated and experimental bond lengths as a function of the composition of the* In_xGa_{1-x} P *alloy at 1000 K. Empty dots with error bars are calculated values, stars are experimental results from literature. The average lattice parameters, scaled to the bond lengths, are given by the dotted and dashed lines. Marzari,* et al. *1994, [223]. Reproduced with permission from American Chemical Society*

The thermodynamic modelling of these alloys has been carried out by a number of authors [222, 224–226], with the aim of obtaining the temperature-dependent interaction coefficients.

This approach has been used, as an illustrative example, by Li *et al.* [222] to calculate the Gibbs free energies of the Ga_xIn_{1-x} P system, where the largest contribution to the mixing enthalpy for the solid solutions is the elastic energy term.

Here the molar Gibbs free energy of the ternary liquid phase G^{l} is given by the following equation

$$G^{l} = \sum_{i=1}^{3} y_i G_i^{o,l} + RT \sum_{i=1}^{3} x_i \ln x_i + G^{l}{}_{\mathrm{Ga,P}} + G^{l}{}_{\mathrm{In,P}} + G^{l}{}_{\mathrm{Ga,In}} + G^{l}{}_{\mathrm{Ga,In,P}} \tag{1.108}$$

where $G_i^{o,l}$ is the Gibbs free energy of the pure element i (Ga, In, P) and x_i is the molar fraction of i in the liquid phase. The $G_{i,j}{}^{1}$ terms are the binary excess Gibbs free energies expressed by the Redlich-Kister equation

$$G_{i,j}{}^{1} = x_i x_j \sum_{n}^{k} L_{i,j}^{k} (x_i - x_j)_{i,j}^{k} \tag{1.109}$$

which could be calculated using the model parameters $L_{i,j}^{k}$ given by Ansara *et al.* [226] for 15 III–V semiconductor binary systems.

The Gibbs energy of the solid phase is given by the following equation

$$\begin{aligned} G^{s} = {} & G_{\mathrm{GaP}}^{o,s} x_{\mathrm{GaP}} + G_{\mathrm{InP}}^{o,s} x_{\mathrm{InP}} + RT(x_{\mathrm{GaP}} \ln x_{\mathrm{GaP}} + x_{\mathrm{InP}} \ln x_{\mathrm{InP}}) \\ & + x_{\mathrm{GaP}} x_{\mathrm{InP}} \sum_{k=0}^{n} L_{\mathrm{GaP-InP}} \; (x_{\mathrm{GaP}} - x_{\mathrm{InP}})^{k} \end{aligned} \tag{1.110}$$

where $G^{o,S}{}_{\mathrm{GaP}}$ and $G^{o,S}{}_{\mathrm{inP}}$ are the Gibbs free energies of formation of the solid GaP and InP and the $L_{\mathrm{GaP\text{-}InP}}$ terms are the interaction coefficients for the binary systems, which were optimized by Li *et al.* [222], including elastic energy correction terms.

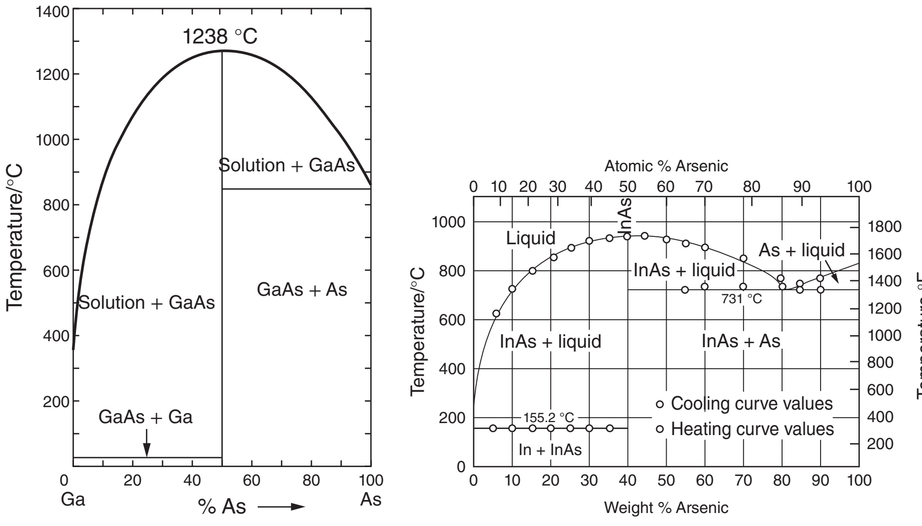

(a) (b)

Figure 1.60 *(a) Phase diagrams of GaAs [227] (b) Phase diagram of InAs*

The results of this simulation are the solid lines in the phase diagram of Figure 1.58, which fit well the experimental points of the liquid and solid lines, as well as those of the solubility gap.

1.7.11.2 Arsenides

InAs and GaAs-based multicomponent semiconductor alloys are widely used for the manufacture of lasers, LED$_S$[14] and photodiodes operating in the 2–5 μm range at room temperature. The quaternary alloys (GaInAsSb, InAsSbP, GaAlAsSb) have the advantage, overpseudo-binary ones, of allowing a better tuning of the emission wavelength by varying the alloy composition. A drawback of these systems is, however, the presence of a miscibility gap, which limits the application of liquid phase epitaxy to a narrow temperature range and induces regions of modulated composition due to spinodal decomposition.

In this section we will limit attention to bulk GaAs, InAs and Ga$_x$In$_{1-x}$ As pseudo-binary alloys and also to the features of epitaxial layers of the quaternary alloys deposited on InP or GaAs substrates by liquid phase epitaxy,[15] where large effects are expected due to misfit strain.

The phase diagrams of GaAs and InAs are displayed in Figure 1.60, which shows that the stoichiometric compounds GaAs and InAs segregate by crystallization of the understoichiometric and overstoichiometric melts, these last only at temperatures above the eutectic temperature.

The general approach to fit the experimental equilibrium data of bulk crystals is to use the regular or quasi-regular solution model with adjustable parameters. More recently,

---

[14] Typically employed for traffic lights and automotive applications.

[15] Liquid phase epitaxy (see details in Chapter 4) is typically used for these types of compounds, which can be deposited, almost stoichiometrically, from the liquid phase at temperatures much lower than the melting temperature of the compound.

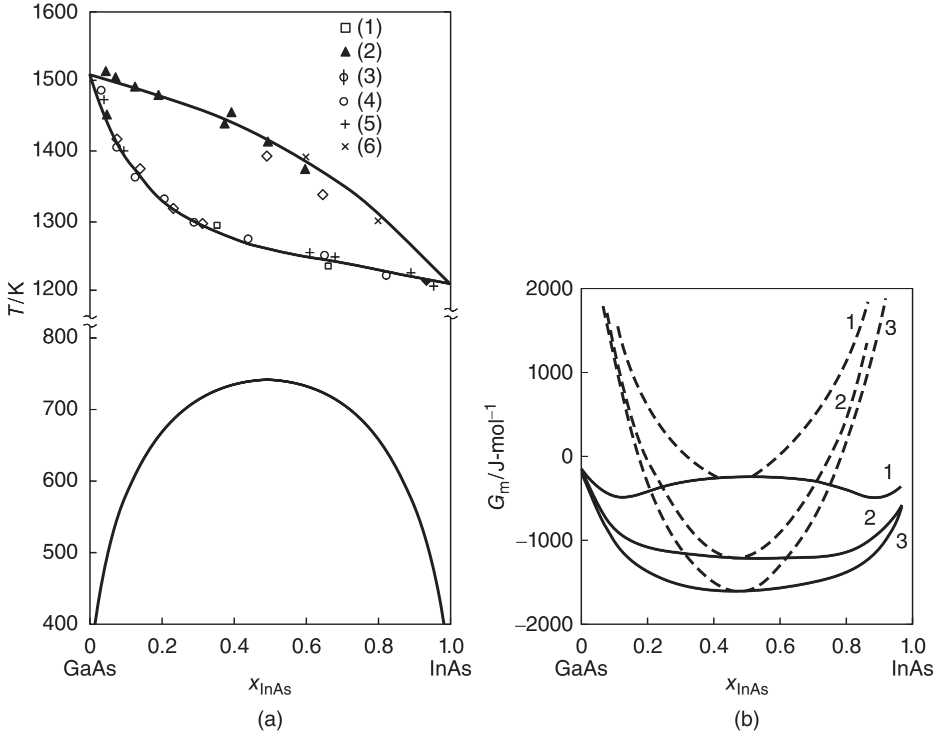

Figure 1.61 *(a) Phase diagram of the free standing system* $Ga_xIn_{1-x}As$*: solid curves are the calculated solid and liquid lines, symbols are experimental results according to references reported in the original paper. (b) Free energy curves for the same system deposited on an InP substrate: solid curves, without elastic energy contribution; dotted curves, with elastic energy contributions 1.* $T = 600$ K*, 2.*$T = 741$ K *and 3.*$T = 800$ K*. Quiao* et al.*, 1994, [229]*

however, the excess thermodynamic functions have been calculated applying the model of linear combinations of chemical potentials (EFLCP) [228].

The phase diagram of the pseudo-binary Ga_xIn_{1-x} As alloy is reported in Figure 1.61a [229], where it is easy to see the good fit between the experimental results and those arising from a simulation (solid lines). The simulation was carried out making use of a model similar to that adopted by Li *et al.* [222] for the GaInP alloys and discussed in the previous section, with optimized, temperature-dependent, interaction parameters. It should be noted that the fit is good in spite of having neglected the possible influence of internal elastic energy contributions, due to the different lattice parameters of the components (see Table 1.14). One can also see that the simulation foresees the opening of a miscibility gap, with a critical temperature of 742 K and a critical composition $x_c \sim 0.5$, whose isothermal composition widths were evaluated from the excess Gibbs free energy curves reported as solid lines in Figure 1.61b.

The effect of elastic energy contributions on the phase equilibria was instead evaluated for the same quaternary system, epitaxially deposited on the (100) surface of an InP substrate, at temperatures slightly above or within the miscibility gap.

The excess molar Gibbs free energy due to the lattice elastic energy was evaluated, in this case, using the following equation

$$\Delta G^{\mathrm{mix}} = -(Ax^2{}_{\mathrm{GaAs}} + Bx^2{}_{\mathrm{InAs}}) \tag{1.111}$$

where A and B are the elastic energy contribution terms associated with the misfit strain. The calculated Gibbs energy curves are reported as dotted lines in Figure 1.61b.

It is apparent that in the presence of elastic energy contributions the system remains homogeneous over the whole range of temperatures considered, including that corresponding to the miscibility gap.

These results are supported by a more recent work [230], addressed at the study of unstrained and strained thin films of III–V semiconductor alloys. The thermodynamic properties of the unstrained alloys are evaluated by assuming the regularity of the liquid solution and calculating its Gibbs energy with the following equation

$$\begin{aligned} G^{\mathrm{l}} = {} & G^{\mathrm{o,l}}_{\mathrm{A}} x_{\mathrm{A}} + G^{\mathrm{o,l}}_{\mathrm{B}} x_{\mathrm{B}} + G^{\mathrm{o,l}}_{\mathrm{C}} x_{\mathrm{C}} + RT(x_{\mathrm{A}} \ln x_{\mathrm{A}} + x_{\mathrm{B}} \ln x_{\mathrm{B}} + x_{\mathrm{C}} \ln x_{\mathrm{C}}) + \Omega^{\mathrm{l}}_{\mathrm{AB}} x_{\mathrm{A}} x_{\mathrm{B}} + \Omega^{\mathrm{l}}_{\mathrm{AC}} x_{\mathrm{A}} x_{\mathrm{C}} \\ & + \Omega^{\mathrm{l}}_{\mathrm{BC}} x_{\mathrm{B}} x_{\mathrm{C}} + \Omega^{\mathrm{l}}_{\mathrm{ABC}} x_{\mathrm{A}} x_{\mathrm{B}} x_{\mathrm{C}} \end{aligned} \tag{1.112}$$

which holds for a generic III–V ($\mathrm{A}_x\mathrm{B}_{1-x}\mathrm{C}$) alloy, where the G^{o} terms are the standard Gibbs energies of the pure components and the Ω terms are the composition-dependent interaction coefficients for the binary components and for the ternary alloy.

The Gibbs energy of unstrained $\mathrm{In}_x\mathrm{Ga}_{1-x}$ As thin films (0.1–1 µm) deposited on a GaAs substrate was calculated by means of the following equation

$$G^{\mathrm{s}} = G^{\mathrm{o,s}}_{\mathrm{AC}} y_{\mathrm{AC}} + G^{\mathrm{o,s}}_{\mathrm{BC}} y_{\mathrm{BC}} + RT(y_{\mathrm{AC}} \ln y_{\mathrm{AC}} + y_{\mathrm{BC}} \ln y_{\mathrm{BC}}) + L^{\mathrm{s}}_{\mathrm{AC\text{-}BC}} y_{\mathrm{AC}} y_{\mathrm{BC}} \tag{1.113}$$

where the G^{o} terms are the Gibbs energy of the binary compounds and L^{s} is the interaction coefficient for the ternary compound.[16]

The results of this simulation (solid lines in Figure 1.62) agree well with the experimental and theoretical results reported in Figure 1.61, although the calculated onset of the miscibility gap occurs at a lower critical temperature of 344 °C.

It is also apparent that the effect of misfit strain is very limited, and almost independent of the film thickness, when the calculated values of bulk samples (dotted curves in Figure 1.62) are compared to those of the films, although with a limited increase in the critical temperature.

For the $\mathrm{In}_x\mathrm{Ga}_{1-x}\mathrm{As}$ alloys deposited in thicker (1–10 µm) layers on (100)- or (111)-oriented InP substrates the effect of misfit strain is severe [230], see Figure 1.63. In this case, a phase with the zinc blende structure segregates in correspondence of equimolar solid solutions and the two phase separation below the solidus temperature should prevent homogeneous growth.

This problem is of critical importance in the epitaxial growth of III–V semiconductors, where it is known that elastically constrained alloys are stabilized against phase separation [232], although in practice phase separation and ordering often also occurs. We will not discuss this further, but it is worth mentioning here that phase separation and ordering in

---

[16] The thermodynamic parameters used for the calculations were obtained from tabulated SGTE (Scientific Group Thermodata Europe) data [231].

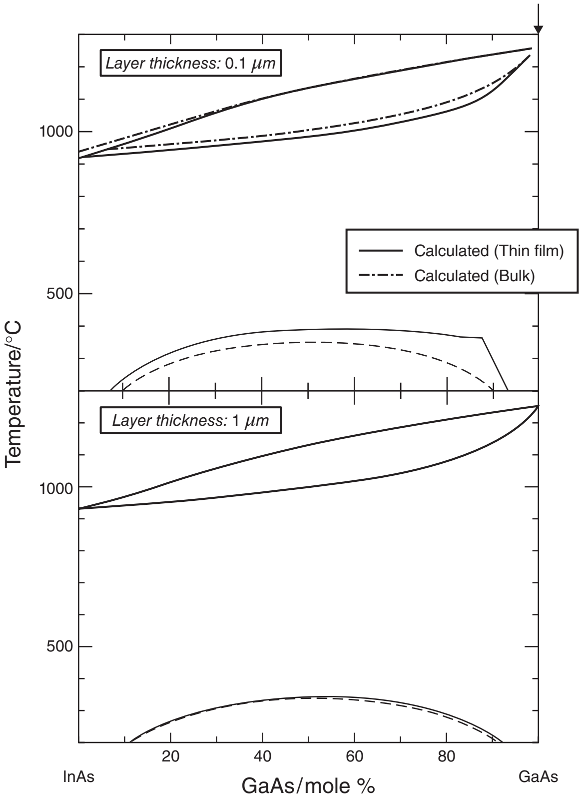

Figure 1.62 *Calculated phase diagram of the InGaAs system as deposited on a GaA substrate. Ohtani* et al.*, 2001, [230]. Reproduced with permission from ASM International*

bulk alloys depend on the sign of the heat of mixing, and that their simultaneous appearance in thin film samples can only be explained by surface energy effects [232]. Phase separation and ordering are features of direct concern for all III–V compounds, but of relevant interest for Group III nitrides, as will be shown in the next section.

1.7.11.3 Nitrides

As already mentioned, due to the extreme thermal properties of these materials, single crystal samples are only available for GaN, and the properties of 'bulk' materials can only be experimentally investigated on unstrained, free standing films separated from the substrate by suitable chemical or mechanical techniques. Due to these experimental challenges, very little is known about the thermodynamic properties of bulk nitride alloys.

The discussion here will be limited to two nitride systems, the InGaN alloys and the InAlN alloys, of which the seconds are very attractive because they could be used as the active layers of LEDs emitting from the red to the near-UV, depending on the alloy composition. In addition, the $Al_{0.83}In_{0.17}N$ alloy is lattice matched with the GaN buffer layer, thus leading to a substantial reduction in defects arising from lattice mismatch, when a single crystal of sapphire, SiC and, more recently, silicon are used as substrates.

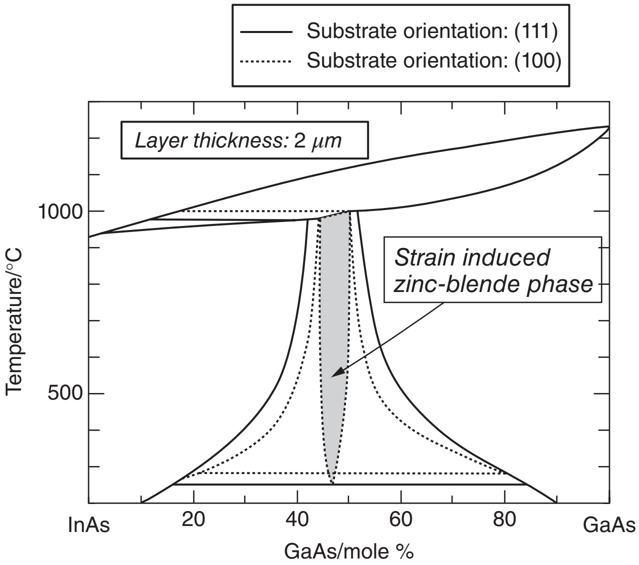

Figure 1.63 *Effect of misfit strain on the phase equilibria of InGaAs thin films deposited on InP substrates. Ohtani* et al.*, 2001, [230]. Reproduced with permission from ASM International*

The growth of the pseudo-binary nitride films is carried out from the vapour phase, at relatively low temperatures, normally using the MO-CVD technique. Therefore, the thermodynamic properties of interest are those concerning the stability and the homogeneity of the phases deposited in the temperature range of the solid phase domain, where the possible opening of a miscibility gap and phase separation processes are typical issues. As spinodal decomposition may involve clustering, phase separation and ordering, knowledge of the features of the phase decomposition processes is important for their direct influence on the optoelectronic properties of the devices which could be manufactured thereof.

Phase separation and ordering have been experimentally observed for $In_xGa_{1-x}N$ samples with $x \geq 0.25$, prepared at 800 °C with atomic layer-MOCVD on sapphire substrates [233]. Phase separation is supposed to be associated with spinodal decomposition and ordering is interpreted to occur via stacking of In and Ga atoms along the c-axis of their wurtzite structure. Ruterana *et al.* [234] also succeeded in showing ordering features in these alloys. Yamaguchi *et al.* [235] studied the $Al_xIn_{1-x}N$ and $Al_{1-y-z}Ga_yIn_z$ N ternary and quaternary alloys grown on a buffer layer of GaN on a sapphire substrate and showed that the Al_xIn_{1-x} N layers could be grown in the $0.01 < x < 0.58$ range without macroscopic phase decomposition, although the tendency to a microscopical phase decomposition was observed. It was also shown that the lattice matched $Al_{0.83}In_{0.17}N$ alloy presented the best crystallinity.

In view of the experimental difficulties associated with the study of phase diagrams of nitride alloys and in the practical absence of experimental results, theoretical studies are well suited and of great support for the design of device growth processes.

As an example, Teles *et al.* [236–238] calculated the phase diagram of the In_xGa_{1-x} N system (see Figure 1.64) which indicates the presence of a very wide region of immiscibility at temperatures lower than 1250 K, with phase separation or spinodal decomposition, in

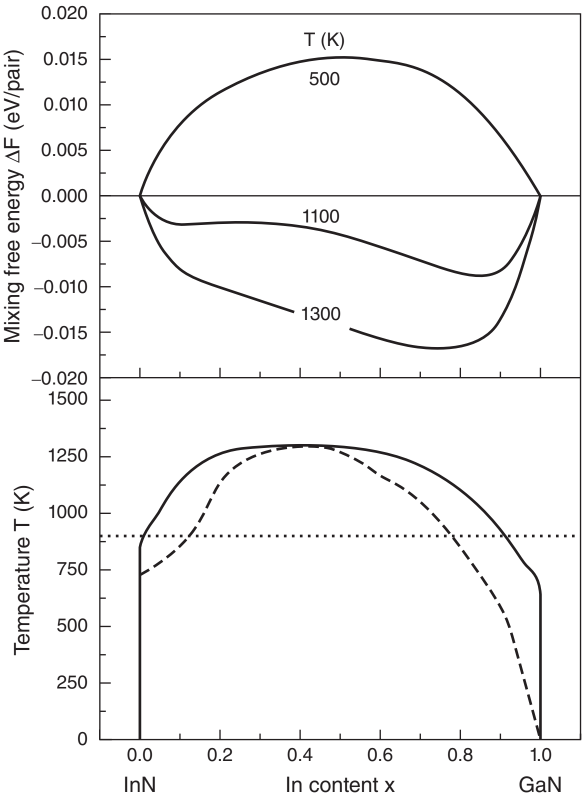

Figure 1.64 *Gibbs energy curves and phase diagram of the InGaN alloys (dotted curves define the region of spinodal decomposition) Teles* et al.*, 2004, [236]*

good agreement with the experimental results [237] which show that phase decomposition effects are active in this system, leading to In-rich crystalline inclusions in the layer.

A better thermodynamic description of the In_xAl_{1-x} N alloys was obtained by an *ab initio* calculation [238], using the Generalized QCA. This model [64] describes the temperature and composition dependence of the Helmholtz free energy $\Delta F(x, T)$ within a cluster approximation, that considers the crystal divided into an ensemble of clusters, statistically and energetically independent of the surrounding atoms. Each class of clusters has the same energy E_j. Each cluster fraction is unknown, but it can be taken as a variational parameter. At the mesoscopic scale the system is assumed to be spatially homogeneous.

Using this approach it was possible to show the presence of an extended miscibility gap in this system with a very high critical temperature, which is even higher (1485 K) in the case of $In_xGa_{1-x}N$ alloy. A substantial composition invariance of the In-N and Al-N bond lengths was also demonstrated in the In_xAl_{1-x} N alloy, which causes Vegard's rule to fail also for the $In_xGa_{1-x}N$ alloys.

Finally, the most complete theoretical investigation concerning the phase diagram of $In_xGa_{1-x}N$ alloys was carried out by Gan *et al.* [240], considering both the zinc blende and wurtzite structure of these alloys. The effect of lattice vibration was also included, which required additional computing time, but which was supposed to have a non-negligible contribution to the free energy.

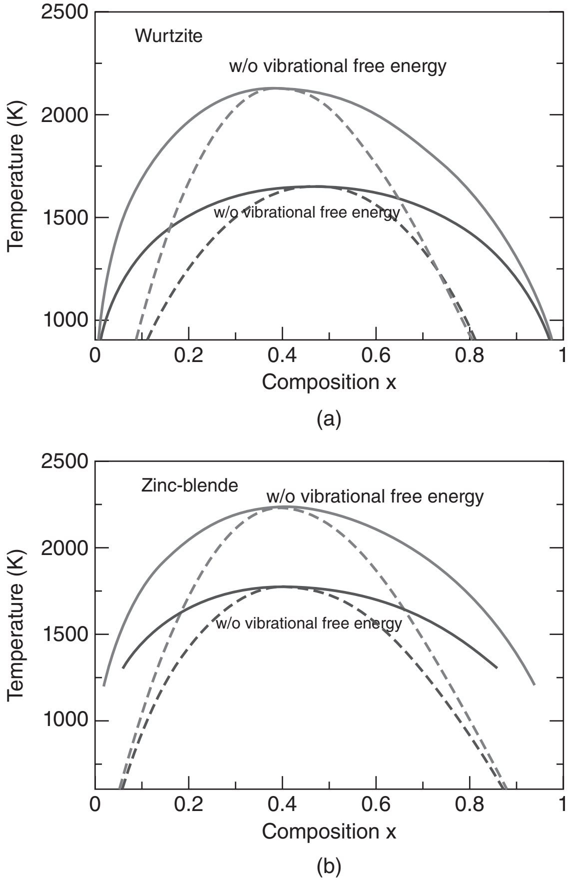

Figure 1.65 *Phase diagram of the InGaN system: the solid lines correspond to the equilibrium bimodal curves, the dotted ones the spinodal ones. Gan,* et al.*, [240]. Reproduced with permission from American Chemical Society and C. K. Gan*

The results of this study (see Figure 1.65) show that the effect of including the vibrational contribution is to decrease the critical temperature and the width of the two phase region, that is to increase the computed solubility range at low temperatures, thus making a notable difference in terms of predictivity compared to less sophisticated models. On that basis, the doping with suitable impurities capable of influencing the lattice vibration spectrum could be an effective strategy capable of extending the useful composition range of nitride alloys.

1.8 Size-Dependent Properties, Quantum Size Effects and Thermodynamics of Nanomaterials

The physical properties of semiconductor nanomaterials (quantum dots, quantum wells, nanowires) depend, as is well known, on their sizes and on quantum effects (increase in the energy gap, quantum localization effects) that do appear when the size is comparable with the Bohr radius of the excitons in the particular semiconductor under study [241] (see Table 1.15 for a number of selected materials). Quantum confinement of strong carriers,

Table 1.15 Bohr radii of excitons in selected semiconductors

Material	Exciton Bohr radius (nm)	Electron mass ($m_n/m°$)	Hole mass ($m_h/m°$)
Si	4.2	0.26	0.49
CdSe	6	0.8	0.45
GaP	6	0.82	0.5
CdTe	8	0.14	0.35
GaAs	15	0.068	0.50
Ge	36	0.12	0.30
PbS	20	—	0.15
InAs	34–74	0.023	0.023
PbSe	46	—	—
InSb	86–138	0.014	0.4
PbTe	1700	0.14	0.20

however, only occurs when the radius of the nanoparticle is much lower than the Bohr radius of the exciton ($R \ll a$) and it comes out that strong confinement would be very difficult to obtain with most of the semiconductors reported in Table 1.15, perhaps with the exception of In- and Pb-compounds.

Also the density of states (DOS) depends on the dimensionality of the nanoparticle. For a spherical particle it has the form

$$\frac{\mathrm{d}N}{\mathrm{d}E} \approx \frac{\mathrm{d}}{\mathrm{d}E} E^{3/2} \approx E^{1/2} \tag{1.114}$$

for a 2D system, such as a quantum well, the DOS is a step function

$$\frac{\mathrm{d}N}{\mathrm{d}E} \approx \frac{\mathrm{d}}{\mathrm{d}E} \sum_{\varepsilon_i<E} (E - \varepsilon_i) \approx \sum_{\varepsilon_i<E} (1) \tag{1.115}$$

for a 1D system (a quantum wire) the DOS is given by

$$\frac{\mathrm{d}N}{\mathrm{d}E} \approx \frac{\mathrm{d}}{\mathrm{d}E} \sum_{\varepsilon_i<E} (E - \varepsilon_i)^{1/2} \approx \sum_{\varepsilon_i<E} (E - \varepsilon_i)^{-1/2} \tag{1.116}$$

while for a 0D system (a quantum dot) the DOS is given by

$$\frac{\mathrm{d}N}{\mathrm{d}E} \approx \frac{\mathrm{d}}{\mathrm{d}E} \sum_{\varepsilon_i<E} \theta(E - \varepsilon_i) \approx \sum_{\varepsilon_i<E} \delta(E - \varepsilon_i) \tag{1.117}$$

There is, however, a problem that remains debated, concerning the role of the surface atoms, whose amount increases with the reduction in size, as seen in Table 1.16 [242] and that of surface reconstruction, passivation and oxidation, which makes the evaluation of 'intrinsic' quantum effects difficult, and strongly dependent on the nature of the material.

As an example, while in the case of CdSe a dot of 1.8 nm, with a relative size of 0.3 Bohr excitons, has 90% of the atoms as surface atoms, in the case of PbSe a dot of 13.8 nm has the same relative size of 0.3 Bohr excitons but only 15% of atoms as surface atoms. It is therefore questionable whether the luminescence of a quantum dot of CdSe comes from quantum confinement effects or from surface atoms. In other wordss, one could argue that when the size dimensions of the Bohr exciton are approached by a nanoparticle, the

Table 1.16 *Density,* D *(%), of surface atoms as a function of the relative size* (R/a_B) *and of the absolute size*(R) *of CdSe and PbSe nanoparticles*

R/a_B	R (nm)	D (%) (CdSe)	R (nm)	D (%) (PbSe)
1	6	30	46	5
0.3	1.8	90	13.8	15
0.1	—	—	4.6	45

Wise, 2000, [242]. Reproduced with permission from American Chemical Society.

distinction between bulk atoms and surface atoms can no longer be ignored with respect to their influence on the optical and electronic properties of the whole system.

It is also worth considering that when the particles are so small, their electronic structure changes and a continuum of energy states is substituted by discrete bonding and antibonding orbitals, in such a way that the properties of these entities in covalent semiconductors are closer to a cluster of molecules than to an extended solid. Therefore, strong quantum confinement effects are better explained using a hybrid molecular language than a semiconductor language [243, 244].

It should finally be noted that the confinement of carriers (electrons and holes) in a nanoparticle calls for a decrease in the thermodynamic stability of the system [243], as it is associated with a decrease in the entropic contribution to its Gibbs free energy.

Besides optoelectronic properties, thermodynamic properties are therefore expected to change when approaching the nanosize. This is the case for the decrease in the eutectic temperatures of nanocrystalline Si-alloys [245] and of the different melting behaviour of metallic, semiconductor and organic nanocrystals, which presents significant differences from that of the corresponding microscopic or macroscopic phases [246], as was already seen in Figure 1.9 for the case of silicon [49].

The decrease in the eutectic temperature[17] of binary metal-Si alloys might be formally evaluated taking into account the contribution of the surface energy to the total energy of the system

$$\Delta G_{\mathrm{tot}} = \Delta G_{\mathrm{bulk}} + \Delta G_{\mathrm{surf}} \tag{1.118}$$

where the first term of Eq. (1.118) may be calculated with the procedures illustrated in Section 1.6.2 and the surface excess term may be evaluated using the following equation

$$\Delta G_{\mathrm{surf}} = \frac{2}{R}\left[x_{\mathrm{A}}\left(\sigma_{\mathrm{l}}{}^{\mathrm{A}} V_{\mathrm{l}}^{\mathrm{A}} - \sigma_{\mathrm{s}}{}^{\mathrm{A}} V s_{\mathrm{s}}{}^{\mathrm{A}}\right) + x_{\mathrm{Si}}\left(\sigma_{\mathrm{l}}{}^{\mathrm{Si}} V_{\mathrm{l}}^{\mathrm{Si}} - \sigma_{\mathrm{s}}{}^{\mathrm{Si}} V_{\mathrm{s}}{}^{\mathrm{Si}}\right)\right] \tag{1.119}$$

where the σ and V terms are the surface tension and molar volume values for silicon and the metallic solute in the liquid and solid state.

The results of an evaluation for three Si alloys are reported in Figure 1.66 [245], which shows that the decrease in the eutectic temperature is substantial and should be taken into account for the design of growth processes of silicon nanowires seeded with gold or silver.

Concerning the size effect of the melting temperature, the information now available relates only to the properties of single components, not that of alloys. It is, however, known that the melting temperatures T_{m} and melting enthalpies decrease with the reduction in size when the nanocrystals are deposited on inert matrices or are free standing.

---

[17] The evaluation of the size dependence of the eutectic temperature of binary Si alloys is important because metallic dots are used to initiate the growth of silicon nanowires, as will be shown in Chapter 4.

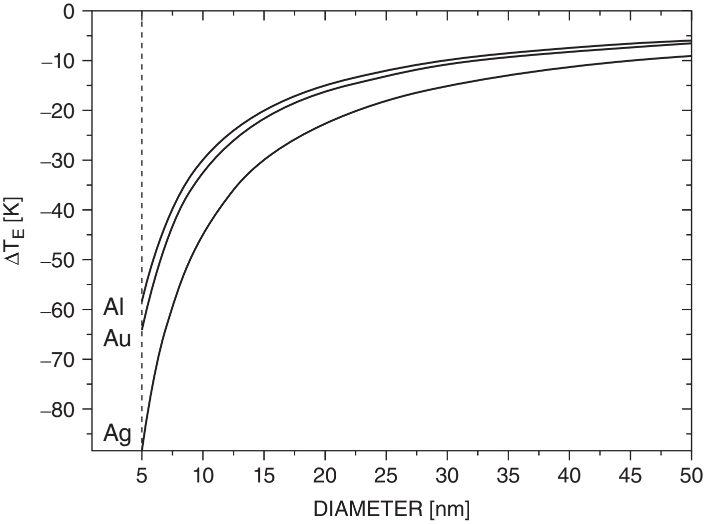

Figure 1.66 *Calculated decrease in the eutectic temperature for Al-Si, Au-Si and Ag-Si alloys with the decrease of the diameter of the nanoparticle. Schmidt,* et al.*, 2010, [245]. Reproduced with permission from American Chemical Society*

As nanophases are systems in metastable equilibrium, the experimental study of size-dependent phase diagrams for binary systems is very difficult, if not impossible. An empirical model without adjustable parameters [247] based on the Lindeman's criterion predicts, however, an exponential relationship between the melting temperature $T_m(D)$ and $1/D$ for metallic nanocrystals

$$T_m(D) = T_m^o \exp - \frac{2S_m^o(D^o - 1)}{3RD} \tag{1.120}$$

where D is the nanocrystal size, T_m^o is the bulk melting temperature, S_m^o is the bulk melting entropy and D^o is a critical size at which almost all the atoms are located at the surface, which corresponds approximately to a value of $D^o = 6\ h$, where h is the atomic/molecular diameter.

A model concerning the size dependence of the interaction coefficient $\Omega(D)$ of regular solutions is also available [248, 249]. As all thermodynamic properties are roughly dependent on 1/D, that is on the surface to volume ratio, it is supposed that Ω should also follow the same relationship. It is assumed, therefore, that the following equation should hold for the interaction coefficient

$$\frac{\Omega(D)}{\Omega^o} = 1 - \frac{2D^o}{D} \tag{1.121}$$

where Ω^o is the bulk value.

This assumption is based on the concept that spontaneous surface bond contraction occurs with reduction of the coordination number, a concept that has been experimentally proven with Raman measurements on several inorganic materials and, also, on AlGaN [250].

On the basis of the known values of the bulk interaction coefficients Ω^o for Ge-Si solutions and on the calculated values of $\Omega(D)$ reported in Table 1.17 [249], the calculated

Table 1.17 *Thermodynamic functions of the Ge and Si systems as a function of the crystal size*

D (nm)		Ge	Si
∞	T_m (K)	1210.4	1685
	H_m (kJ mol^{-1})	36.940	50.550
	Ω^s (kJ mol^{-1})	7.666	
	Ω^l (kJ mol^{-1})	7.715	
10	T_m (K)	1096.7	1472.2
	H_m (kJ mol^{-1})	24.542	33.135
	Ω^s (kJ mol^{-1})	4.437	
	Ω^l (kJ mol^{-1})	4.465	
5	T_m (K)	1096.7	1472.2
	H_m (kJ mol^{-1})	24.542	33.135
	Ω^s (kJ mol^{-1})	1.208	
	Ω^l (kJ mol^{-1})	1.215	

Liang *et al.*, 2003, [249].

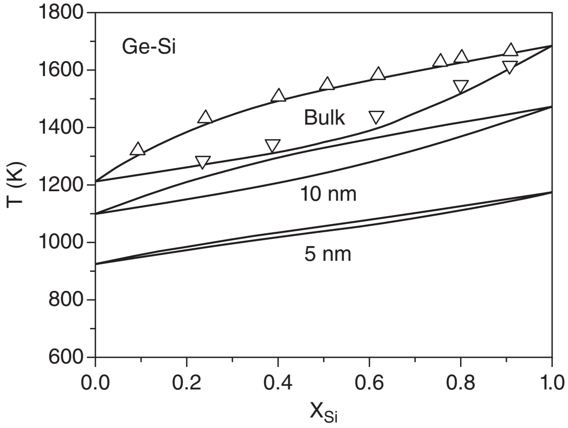

Figure 1.67 *Evolution of the Ge-Si phase diagrams as a function of the nanocrystallite size. Liang* et al.*, 2003, [249]. Reproduced with permission from Institute of Physics and Q. Jiang*

evolution of the phase diagram of the Ge-Si system as a function of the size is reported in Figure 1.67. As the size of the crystals decreases to a critical value, which for the case of Si-Ge alloys is close to the excitonic radius, the liquid and the solid phase are almost indistinguishable.

Another size-dependent transformation occurs inside the CdTe-CdSe system. It was shown [251] that the structure of spherical CdTe/CdSe quantum dots having a size ~8 nm, synthesized in a two-step procedure with CdTe nanoparticles (4 nm) as nuclei, have the structure of a CdTe-rich core enclosed by a CdSe shell. However, spherical CdSe/CdTe quantum dots with a size of about 9 nm, synthesized via a similar two-step procedure but with smaller CdSe nanoparticles (3 nm) as nuclei, appear single phase with a relatively uniform distribution of CdSe and CdTe.

Another, notable example of size-dependent thermodynamic properties is given by the phase transformation of bulk diamond to graphite which, in the absence of catalysts occurs at pressures larger than 10 GPa around 4000 K (see Figure 1.38), well above the equilibrium solidus line. When this phase transition is studied on diamond nanocrystallites having a grain size of 18 nm, it occurs at a pressure of about 5 GPa, as demonstrated by X-ray diffraction and Raman experiments, at 1623 K, close to the equilibrium conditions [252].

The effect of pressure on the transformation of silicon nanocrystals from the semiconducting- to the metallic β-Sn phase has also been considered, as well as that of the pressure on the transformation of CdSe nanocrystals from the wurtzite to the rocksalt structure [253].

In this last case it was demonstrated that the transformation involves single domains and only one nucleation event per crystallite and that the transformation pressure increases with decrease in the size of the nanocrystals [253], different from the case of phase transitions in bulk semiconductors, which are highly hysteretic, are nucleated by defects and typically involve multiple nucleation centres and domain fracture.

The result of this work leads to conclusions of serious impact for the study of phase transformations. As nanocrystallites are smaller than the domain fragments generated in a solid–solid transformation, nanocrystallites are ideally suited for the study of phase transformations, because they can be grown almost defectless, though with a large surface to bulk ratio, where the surface provides the nucleation sites.

Moreover, the increase in the transformation pressure with the decrease in nanocrystal size demonstrates that this effect is associated with a decrease in available nucleation centres at the surface and that the process is controlled by kinetic, not thermodynamic factors. The observed changes in nanocrystal shape during the transformation, induced by interior atoms motion towards the nucleation sites, provides direct evidence that homogeneous deformations play a role in phase transitions in semiconductors.

APPENDIX

Use of Electrochemical Measurements for the Determination of the Thermodynamic Functions of Semiconductors

EMF measurements with galvanic cells using solid electrolytes have been so widely used for the determination of the thermodynamic functions of inorganic solids at high temperatures in the last half century [254–256] that this method may be considered a standard thermochemical technique [257].

As is well known, the EMF of a galvanic cell with the following configuration

$$\mathrm{Pt/Me, MeX_2//electrolyte}\ (t_X = 1)//\mathrm{X_2}(P = 0.01325\ \mathrm{KPa})/\mathrm{Pt} \tag{A1}$$

where t_X the transport number of X^- anions in the electrolyte, gives a measure of the Gibbs free energy of formation $\Delta G^o{}_{MeX_2}$ of MeX_2

$$E = -\frac{RT}{2F}\Delta G^o{}_{MeX_2} \tag{A2}$$

where E in volts is the EMF of the cell and F is the Faraday constant.

In this kind of measurement the electrolyte must be a suitable solid material presenting pure ionic (X^-) conductivity in the range of temperatures where $\Delta G^o{}_{MeX_2}$ should be measured, the left-hand electrode is a heterogeneous mixture of Me and MeX_2 suitably pressed in the form of a pellet and the right-hand electrode works as a reversible X_2 electrode. Alkaline earth fluorides, such as CaF_2, are good examples of F^- conducting electrolytes.

The metallic Pt electrodes allow the exchange of electrons involved in both half-cell reactions

$$\mathrm{Me} + 2\,\mathrm{X}^- \rightleftharpoons \mathrm{MeX}_2 + 2\mathrm{e(Pt)} \tag{A3}$$

$$\mathrm{X}_2 + 2\mathrm{e(Pt)} \rightleftharpoons 2\mathrm{X}^- \tag{A4}$$

but could be substituted by other types of metals or electronic conductors able to satisfy the condition of electronic equilibrium between the metal electrode and the reactants in both the electrode compartments. The right-hand metallic electrode must behave as a reversible electrode, and this condition is not obvious for all types of X^-/X_2 redox couples.

Using the electrochemical potential definition given in Section 1.4.6 [7, 9] for the thermodynamic description of the processes occurring in the cell (Eq. A1), we can see that at the electrodes the following equilibria occur

$$2\eta_e^{Pt(1)} + \eta^{Me}_{Me^{2+}} = \mu_{Me} \tag{A5}$$

$$2\eta^{X_2}_{X^-} - \eta_e^{Pt(2)} = \mu_{X_2} \tag{A6}$$

$$\eta^{Me}_{Me_2} + \eta^{MeX_2}_{X^-} = \mu_{MX_2} \tag{A7}$$

At the different phase boundaries, instead, the following equilibria occur

$$\eta_e^{Pt(1)} = \eta_e^{Me} \tag{A8}$$

$$\eta^{Me}_{Me^{2+}} = \eta^{MeX_2}_{Me^{2+}} \tag{A9}$$

$$\eta^{MeX_2}_{X^-} = \eta^{Pt(2)}_{X^-} \tag{A10}$$

$$\eta_e^{X_2} = \eta_e^{Pt(2)} \tag{A11}$$

It is therefore possible to obtain a relationship between the difference in the internal electrical potentials $\Delta\varphi$ at the Pt electrodes and the cell reaction, by writing

$$\eta_e{}^{Pt(1)} - \eta_e{}^{Pt(2)} + \eta_e^{Me} - \eta_e^{X_2} = \eta^{Me}_{Me^{2+}} + \eta^{MeX_2}_{X^-} \tag{A12}$$

$$\begin{aligned}\mu_e{}^{Pt(1)} - \mu_e{}^{Pt(2)} &= \mu^{Me}_{Me^{2+}} + \eta^{MeX_2}_{X^-} - \eta_e^{Me} - \eta_e^{X_2} = \mu_{MX_2} - (\mu_{Me} + \mu_{X_2})\\ &= \Delta G^o{}_{MX_2} = -2F\Delta\varphi \end{aligned} \tag{A13}$$

Therefore the EMF of the cell (Eq. (A2)) in thermodynamic equilibrium conditions (open circuit voltage) is

$$\mathrm{EMF} = -\frac{\Delta G^o{}_{MX_2}}{2F} \tag{A14}$$

If MX_2 is MeO_2, the electrolyte consists of an yttria-doped ZrO_2 solid solution, presenting pure O^{2-} conductivity and the right-hand electrode works as an oxygen electrode at a pressure P = 0.101325 kPa, the overall cell reaction may be written as

$$\mathrm{Me} + \mathrm{O_2}(P = 0.101325\ \mathrm{kPa}) \rightleftharpoons \mathrm{MeO_2} \tag{A15}$$

Therefore, under the assumption that both electrode reactions are reversible and that the ionic conductivity of the electrolyte is sufficiently high to allow fast equilibration, the EMF measured at the electrodes is proportional to the standard Gibbs free energy of formation of MeO_2, $\Delta G°(MeO_2)$ according to the following equation

$$E = -\frac{\Delta G^{o}_{\mathrm{MeO_2}}}{4F} \tag{A16}$$

If at the left-hand electrode we have, instead, a non-stoichiometric oxide, formally considered as a solution of MeO in MO_2 and at the right-hand electrode we have pure MO_2, the measured EMF is proportional to the activity of MO_2 in the MeO_{2-x} solution at the left-hand electrode compartment

$$E = -\frac{RT}{4F}\ln a_{\mathrm{MeO_2}} = -\frac{RT}{4F}\ln \gamma x_{\mathrm{MO_2}} \tag{A17}$$

thus allowing determination of the activity $a = \gamma x$ and then the chemical potential of MO_2 in solution and of the interaction coefficient Ω for that particular solid solution system.

Provided a suitable electrolyte is available, the thermodynamic functions of a variety of complex solids may be investigated, as is the case for the potassium–graphite lamellar compounds, which have been studied [258] in the temperature range 200–350 °C with a solid-state EMF technique, using as the electrolyte a glass reversible to potassium ions and liquid potassium as the reference electrode.

The cell used was the following:

$$\mathrm{K_l}//\mathrm{glass}\ (t_{\mathrm{K+}} = 1)\ //\mathrm{K_{graphite}} \tag{A18}$$

using Ni wires as the electrodes. The EMF of the cell is proportional to the activity of K in the lamellar compound through the equation

$$E = -\frac{RT}{F}\ln a_{\mathrm{K(graphite)}} \tag{A19}$$

as the activity of K in liquid potassium is unity.

This technique has been rarely applied to semiconductors, as the challenge of EMF measurements for the determination of thermodynamic functions of semiconductors is the availability of suitable electrolytes. Oxides, fluorides, chlorides electrolytes are available, as well as pure H^+, Ag^+, Li^+ or Al^{3+} (β-Al_2O_3 or aluminium tungstate $Al_2(WO_4)_3$ electrolytes [259], which are, however, of little interest for most semiconductors of common use, with the potential[18] exception of Al-based compound semiconductors or hydrogenated semiconductors.

Therefore, as an alternative route, the possibility of equilibrating the semiconductor with an intermediate buffer phase which, in turn, should undergo fast equilibrium conditions with an oxide- or chalcogenide-type of electrolyte has been studied.

---

[18] To the author's knowledge, EMF measurements with Al^{3+} or H^+ ionic conductors have been never carried out on semiconductors.

In this case the problem could be the slow rate of the equilibration processes between the semiconductor and the intermediate buffer phase (which must also exhibit electronic conduction to satisfy electrochemical potentials equilibria) due to slow ion exchange reactions at the semiconductor/intermediate material interface.

This technique was originally applied [260] for the study of the structure relationships in the $CaO - ZrO_2$ system in the 900–1100 °C temperature range, using CaF_2 as the electrolyte, which is a pure F^- conducting electrolyte, in the following cell

$$\begin{aligned}\mathrm{Pt}\ /(O_2)P = 0.101\mathrm{KPa}//CaO(+CaF_2)//CaF_2(t_{F^-} = 1)//Zr_{1-x}Ca_xO_{2-x}\\ \times(+CaF_2)//(O_2)P = 0.101\mathrm{KPa}/\mathrm{Pt}\end{aligned} \tag{A20}$$

for which the EMF is proportional to the activity of CaO in the $CaO_xZrO_{2(1-x)}$ system

$$E = -\frac{RT}{2F}\ln a_{CaO(CaO_xZrO_{2(1-x)})} \tag{A21}$$

In this case, a fast equilibrium between the oxide and CaF_2 phases in the left-hand and right-hand compartments was experimentally demonstrated to occur at the high temperatures of the experiment.

The same approach was recently followed [261] for the study of the thermodynamic functions of the ternary Zn_xCd_{1-x} Te alloys and binary Zn_xTe_{1-x} alloys using ZnO as the intermediate phase, and an yttria-doped ZrO_2 electrolyte.

The cell used to measure the activity of Zn in the alloy was:

$$\mathrm{Zn, ZnO}\ //ZrO_2\text{-}Y_2O_3//Zn_xCd_{1-x}Te/ZnO \tag{A22}$$

with a Zn/ZnO reference electrode which keeps the activity of Zn at unity.

The EMF of this cell

$$E = -\frac{RT}{2F}\ln a_{Zn\ (Zn_x\ Cd_{1-x}\ Te)} \tag{A23}$$

is therefore directly proportional to the activity of Zn in the Zn_xCd_{1-x} Te alloy.

The results of the measurements fit well with the calculated ones, as can be seen in Figure A.1.

A $CdCl_2$-CuCl electrolyte, presenting a pure Cu^+ conductivity, was instead used to study the properties of $Cu_{2\pm\delta}$ Se semiconductors [262] and a $Cu_4RbCl_3I_2$ was used as a Cu^+ ion conducting solid electrolyte for the study of the Cu–As–S system at temperatures from 300 to 370 K using EMF measurements [263]. From the EMF data the standard thermodynamic functions of formation and standard entropies of the ternary compounds were obtained, showing the significant potential of the EMF technique as a thermochemical tool in the field of compound semiconductors. EMF measurements were also used to study the oxygen activity in liquid silicon [264] with an oxygen sensor directly dipped in the melt of a CZ puller, using a zirconia-based electrolyte and a V/V_2O_3 reference electrode.

The EMF of the cell

$$C//O_{Si}/ZrO_2\text{-}Y_2O_2//V, V_2O_3//\text{Pt-Rh} \tag{A24}$$

gives the relative activity of the oxygen in liquid silicon directly

$$E = \frac{RT}{2F}\ln\frac{p''_{O_2}}{p'_{O_2}} = \frac{RT}{2F}\ln a_O \tag{A25}$$

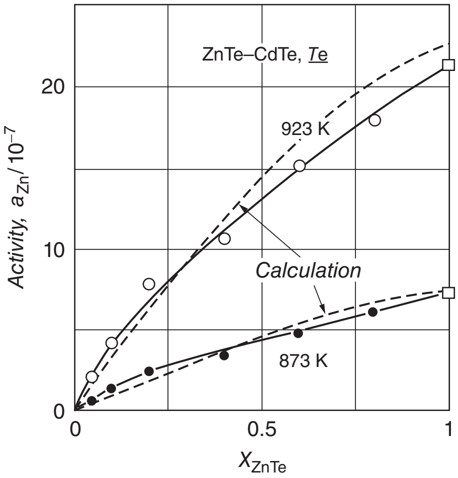

Figure A.1 *Activity of Zn (in* 10^{-7} *units) in the Te-rich region of the ternary* Zn_xCd_{1-x} *Te alloy [261]*

where $p''(O_2)$ is the equilibrium partial pressure of oxygen of the oxygen-liquid silicon solution and $p'(O_2)$ is the equilibrium oxygen pressure of the V/V_2O_3 system.

As the oxygen content in a silicon melt at the temperature of the measurements (slightly above the melting temperature of silicon) is in the range 0.001–0.01%, the activity coefficient was assumed equal to 1. The results of the EMF measurements were compared to the results of oxygen content measured by FTIR measurements[19] and showed encouraging potential of this technique as a routine analytical tool.

Last but not least, the Gibbs free energies of formation of 3C- and 6H-silicon carbides were determined between 1623 and 1898 K by measuring the silicon solubility in liquid gold in equilibrium with silicon carbide and graphite [177]. The solution behaviour of the Au–Si system provides a good fit with the small difference in the activity of silicon exhibited by the two polytypes, thus offering greater experimental precision over previous similar methods. For 6H-SiC, the Gibbs free energy of its formation, ΔG (J mol^{-1}) $= -116\,900(\pm 7.2) + 38.2(\pm 4.1)T$ (where T is in K) relative to liquid silicon and graphite standard states, is in excellent agreement with other investigations, indicating that the method is capable of determining the Gibbs energy of formation with a precision of about 0.7 kJ mol^{-1}. The measurements on 3C-SiC exhibited greater experimental scatter, which may have been due to variations in the density of non-equilibrium defects of the crystals used, although experimental problems encountered with the complex crystal shapes may have also contributed. The precision of the technique is, however, sufficient to get information on polytype stability and perhaps on the Gibbs energy contributions of non-equilibrium defects.

---

[19] Fourier Transform IR measurements are routinely used for the determination of the concentration of oxygen in solid silicon samples.

References

1. Swalin, R.A. (ed) (1961) *Thermodynamics of Solids*, John Wiley & Sons, Inc., New York.
2. Rao, C.N.R. and Gopalakrishnan, J. (1986) *New Directions in Solid State Chemistry*, Cambridge University Press, Cambridge.
3. West, A.R. (1992) *Solid State Chemistry*, John Wiley & Sons, Ltd, Chichester.
4. Elliot, S. (1998) *The Physics and Chemistry of Solids*, John Wiley & Sons, Ltd, Chichester.
5. Le Roy, E. and O'Keeffe, M. (1970) *The Chemistry of Extended Defects in Non-Metallic Solids*, North Holland, Amsterdam.
6. Barron, A. *Chemistry of Electronic Materials Open Educational Resource*, http://cnx.org/content/col10719/latest/ (accessed 22 December 2014) (2013).
7. Guggenheim, E.A. (1952) *Thermodynamics*, North Holland, Amsterdam.
8. Kittel, C. (2005) *Introduction to Solid State Physics*, John Wiley & Sons, Inc., New York.
9. Ashcroft, N.W. and Mermin, N.D. (1988) *Solid State Physics HRW International Editions*, Sounders College, Philadelphia.
10. Cool, T., Bartol, A., Kasenga, M. *et al.* (2010) Gibbs: phase equilibria and symbolic computation of thermodynamic properties. *Calphad*, **34**, 393–404.
11. Santhanaman, P., Gray, D.J. Jr., and Ram, R.J. (2012) Thermoelectrical pumped light emitting diodes operating above unit efficiency. *Phys. Rev. Lett.*, **108**, 097403-1–097403-4.
12. Shockley, W. and Queisser, H.J. (1961) Detailed balance limit of efficiency of p-n junction solar cells. *J. Appl. Phys.*, **32**, 510–519. doi: 10.1063/1.1736034
13. Prigogine, I. (1967) *Thermodynamics of Irreversible Processes*, 3rd edn, Interscience, John Wiley & Sons, Inc., New York.
14. de Panfilis, S. and Filipponi, A. (1997) Short-range order in liquid tellurium probed by X-ray absorption spectroscopy. *Europhys. Lett.*, **37**, 397–402.
15. DeCicco, A., Rosoleny, M.J., Marassiz, R. *et al.* (1996) Short range order in liquid and solid KBr probed by EXAFS. *J. Phys. Condens. Matter*, **8**, 10779–10797.
16. Pizzini, S., Binetti, S., Calcina, D. *et al.* (2000) Local structure of erbium-oxygen complexes in erbium-doped silicon and its correlations with the optical activity of erbium. *Mater. Sci. Eng.*, **B 72**, 173–176.
17. Inui, M. (2000) EXAFS studies of liquid semiconductors. *J. Phys. Chem. Solids*, **61**, 2007–2012.
18. Lebedev, I., Michurin, A.V., Sluchinskaya, I.A. *et al.* (2000) EXAFS and electrical studies of new narrow-gap semiconductors: $inTe_{1-x}Se_x$ and $In_{1-x}Ga_xTe$. *J. Phys. Chem. Solids*, **61**, 2007–2012.
19. Byrne, A.P., Ridgway, M.C., Glover, C.J. and Bezakova, E. (2004) Comparative studies using EXAFS and PAC of lattice damage in semiconductors. *Hyperfine Interact.*, **158**, 245–231.
20. Kazmerski, L.L. (1998) Photovoltaics characterization: a survey of diagnostic measurements. *J. Mater. Res.*, **13**, 2684–2708.

21. Adams, F., Van Vaeck, L. and Barrett, R. (2005) Advanced analytical techniques: platform for nano materials science. *Spectrochim. Acta, Part B*, **60**, 13–26.
22. Razeghi, M. (2006) Semiconductor characterization techniques, in *Fundamentals in Solid State Engineering*, Springer, pp. 521–549.
23. Hockett, R.S. (2012) Advanced analytical techniques for solar grade feedstock, in *Advanced Materials for Photovoltaic Applications* (ed S. Pizzini), John Wiley & Sons, Inc., pp. 215–234.
24. Kumar, A., Gencarelli, F., Kambham, A.K. *et al.* (2012) Study of Sn migration during relaxation of Ge(1-x)Sn(x) layers using atom probe tomography. *Phys. Status Solidi C*, **9**, 1924–1930.
25. Miller, M.K. (1999) *Atom Probe Tomography*, Kluger Academic, Plenum Press, New York.
26. Lauhon, L.J., Adsumilli, P., Rosenheim, P. *et al.* (2009) Atom probe tomography of semiconductor materials and device structures. *MRS Bull.*, **34**, 738–743.
27. Hudelson, S., Newman, B.K., Bernardis, S. *et al.* (2010) Retrograde melting and internal liquid gettering in silicon. *Adv. Mater.*, **22**, 3948–3953.
28. Buonassisi, T., Istratov, A.A., Pickett, M.D. *et al.* (2006) Chemical natures and distributions of metal impurities in multicrystalline silicon materials. *Prog. Photovoltaics Res. Appl.*, **14**, 513–531.
29. Buonassisi, T., Marcus, M.A., Istratov, A. *et al.* (2005) Analysis of copper-rich precipitates in silicon: chemical state, gettering, and impact on multicrystalline silicon solar cell material. *J. Appl. Phys.*, **97**, 063503.
30. Buonassisi, T., Heuer, M., Istratov, A.A. *et al.* (2007) Transition metal co-precipitation mechanisms in silicon. *Acta Mater.*, **55**, 6119–6126.
31. Bertoni, M.I., Fenning, D.P., Rinio, M. *et al.* (2011) Nanoprobe X-ray fluorescence characterization of defects in large-area solar cells. *Energy Environ. Sci.*, **4**, 45–52.
32. Sarma, B.N., Prasad, S.S., Vijayvergiva, S. *et al.* (2003) Existence domains for invariant reactions in binary regular solution phase diagrams exhibiting two phases. *Bull. Mater. Sci.*, **26**, 423–430.
33. Sher, A., van Schilfgaarde, M., Chen, A.-B. and Chen, W. (1987) Quasichemical approximation in binary alloys. *Phys. Rev. B*, **36**, 4279–4295.
34. Wei, S.-H., Ferreira, L.G. and Zunger, A. (1990) First principle calculations of temperature-composition phase diagrams of semiconductors alloys. *Phys. Rev. B*, **41**, 8240–8269.
35. Vegard, L. (1921) Die Konstitution der Mischkristallen und die Raumfüllung der Atome. *Z. Phys.*, **5**, 17–26.
36. Crawford, J.H. Jr. and Slifkin, L.M. (1972) *Point Defects in Solids*, vol. **1** and **2**, Plenum Press, New York.
37. Auguillo-Lopez, F., Catlow, C.R.A. and Towsend, P.D. (1988) *Point Defects in Materials*, Academic Press, London.
38. Pizzini, S. (2002) *Defect Interaction and Clustering in Semiconductors*, Scitech Publications, Ueticon-Zürich.
39. Pichler, P. (2004) *Intrinsic Point Defects, Impurities and Their Diffusion in Silicon*, Springer.

40. Kröger, F.A. and Vink, H.J. (1956) Relations between the concentration of imperfections in crystalline solids, in *Solid State Physics*, vol. **3** (eds F. Seitz and D. Turnbull), Academic Press, New York, pp. 307–435.
41. *CRC Handbook of Chemistry and Physics*, 88th edn, (2007–2008) CRC Press, Taylor & Francis Group, Boca Raton, FL, London, and New York.
42. Soma, T. and Matsuo, H. (1982) Lindeman's Melting Law and the effect of pressure on the melting point of Si and Ge. *Phys. Status Solidi B*, **109**, 387–391.
43. Hänström, A. and Lazor, P. (2000) High pressure melting and equation of state of aluminium. *J. Alloys. Compd.*, **305**, 209–315.
44. Bundy, F.P. (1964) Phase diagrams of silicon and germanium to 200kBar at 1000°C. *J. Chem. Phys.*, **41**, 3809–3814.
45. Kailer, A., Gogotsi, Y.G. and Nickel, K.G. (2002) Phase transformations of silicon caused by contact loading. *J. Appl. Phys.*, **81**, 3057–3064, and references therein.
46. Besson, J.M., Itie, J.P., Polian, A. *et al.* (1991) High pressure phase transitions and phase diagram of gallium arsenide. *Phys. Rev. B*, **44**, 4214–4236.
47. Guinier, A., Bokij, G.B., Boll-Dornberger, K. *et al.* (1984) Nomenclature of polytype structures. *Acta Crystallogr., Sect. A*, **40**, 399–404.
48. Luo, F., Chen, Y.-R., Cai, L.-C. and Jing, F.-Q. (2011) The melting curves and the entropy of iron under high pressure. *J. Chem. Eng. Data*, **56**, 2063–2070.
49. Yang, C.C., Li, G. and Jiang, Q. (2003) Effect of pressure on melting temperature of silicon. *J. Phys. Condens. Matter*, **15**, 4961–4965.
50. Glazov, V.M. and Shchelikov, O.D. (2000) Volume changes during melting and heating of silicon and germanium melts. *High Temp.*, **38**, 405–412.
51. Lindeman, F. (1910) The calculation of molecular vibration frequencies. *Z. Phys.*, **11**, 609.
52. Knudson, M.D., Desjarlais, M.P. and Dolan, D.H. (2008) Phases of carbon: shock-wave exploration of the high pressure. *Science*, **322**, 1822–1825.
53. Soma, T., Itoh, T. and Kagaya, H.M. (1984) Pressure dependence of melting point of Al. *Phys. Status Solidi A*, **126**, 661–669.
54. Kagaya, H.-M., Imazawa, K., Sato, M. and Soma, T. (1998) Lindeman's melting law and solidus curve under pressure of Al-Si and Al-Ge solid solutions. *J. Mater. Sci.*, **33**, 2595–2599.
55. Yang, C.C., Li, J.C. and Jiang, Q. (2003) Effect of pressure on melting temperature of silicon determined by Clapeyron equation. *Chem. Phys. Lett.*, **372**, 156–159.
56. Garai, J. and Chen, J. (2008) Pressure Effect on the Melting Temperature, NSF Grant #0711321. Physics Archive arXiv:0805.0249.
57. Li, C., Wang, F. and Zhang, W. (2004) Pyrolysis effect of group V vapor sources on the composition ranges for metal-organic vapor phase epitaxy growth of III-V semiconductors. *J. Phase Equilib. Diffus.*, **25**, 53–58.
58. Kattner, U.R. (1997) Thermodynamic modeling of multicomponent phase equilibria. *J. Manage.*, **49**, 14–19.
59. Pelton, A.D. (1991) Thermodynamics and phase diagrams of materials, in *Materials Science and Technology* (eds R.W. Cahn, R. Haasen and E.J. Kramer), Wiley-VCH Verlag GmbH, Weinheim, pp. 3–73.

60. Stolen, S., Grande, T. and Allan, N.L. (2004) *Chemical Thermodynamics of Materials*, John Wiley & Sons, Ldt, Chichester.
61. Mbaye, A.A., Ferreira, L.G. and Zunger, A. (1987) First principle calculation of semiconductor alloy phase diagrams. *Phys. Rev. Lett.*, **58**, 49–52.
62. Ansara, I. (1998) Thermodynamic modelling of solution and ordered phases. *Pure Appl. Chem.*, **70**, 449–459.
63. Austin Chang, Y., Chen, S., Zhang, F. *et al.* (2004) Phase diagram calculation: past, present and future. *Prog. Mater. Sci.*, **49**, 313–345.
64. F. Bechsedt Nitrides as seen by a theorist, in *Low Dimensional Nitride Semiconductors*, B. Gil Ed, pp, 11–49, Oxford. Oxford University Press 2002.
65. van Laar, J.J. (1908) Melting-point and freezing-point curves in binary systems, when the solid phase is a mixture (amorphous solid solution or mixed crystals) of both components. *Z. Phys. Chem.*, **63**, 216.
66. van Laar, J.J. (1908) Die Schmelz- oder Erstarrungskurven bei biL̈aren Systemen, wenn die feste Phase ein Gemisch (amorphe feste L̈osung oder Mischkristalle) der beiden Komponenten ist. *Z. Phys. Chem.*, **64**, 257.
67. Hildebrand, J.H. (1929) Solubility. XII. Regular solutions. *J. Am. Chem. Soc.*, **51**, 66.
68. Fowler, R.H. and Guggenheim, E.A. (1939) *Statistical Thermodynamics*, Cambridge University Press, Cambridge, pp. 350–366.
69. Guggenheim, E.A. (1952) *Mixtures*, Oxford University Press.
70. Baldereschi, A. and Peressi, M. (1993) Atomic scale structure of ionic and semiconducting solid solutions I. *J. Phys. Condens. Matter*, **5**, 837–848.
71. A.D Pelton, Thermodynamics and phase diagrams of materials, in *Phase Transformations in Materials*. G. Kostorz Ed, 3–80 Wiley-VCH Verlag GmbH, Weinheim (2001)
72. Desay, P.T. (1986) The thermodynamic properties of iron and silicon. *J. Phys. Chem. Ref. Data*, **16**, 967–980.
73. Zhigilei , L.V. Phase Diagrams and Kinetics, (2015) University of Virginia, Department of Materials Science and Engineering **MSE 3050: Thermodynamics and Kinetics of Materials**
74. Pelton, A.D. and Thompson, W.T. (1975) Phase diagrams. *Prog. Solid State Chem.*, **10**, 119–155.
75. Oonk, H.A. (1981) *Phase Theory: The Thermodynamics of Heterogeneous Equilibria*, Elsevier, Amsterdam.
76. DeHoff, R.T. (1993) *Thermodynamics in Materials Science*, McGraw-Hill, New York.
77. Chang, Y.A., Chen, S.L., Zhang, F. *et al.* (2004) Phase diagram calculation: past, present and future. *Progr.Mater.Sci.*, **49**, 313–345.
78. Weber, E. (1983) Transition metals in silicon. *Appl. Phys. A*, **30**, 1–22.
79. Swain, S.K., Jones, K.A., Datta, A. and Lynn, K.G. (2011) Study of different cool down schemes during the crystal growth of detector grade CdZnTe. *IEEE Trans. Nucl. Sci.*, **58**, 2341–2345.
80. Fistul, V.I. (2005) *Impurities in Semiconductors: Solubility, Migration and Interactions*, CRC Press.
81. Istratov, A.A., Zhang, P., McDonald, R.J. *et al.* (2005) Nickel solubility in intrinsic and doped silicon. *J. Appl. Phys.*, **9**, 0235051.

82. McKelvey, A.L. (1996) Retrograde solubility in semiconductors. *Metall. Mater. Trans. A*, **27A**, 2704–2707.
83. Varamban, S.V. and Jacob, K.T. (1996) Discussion of retrograde solubility in semiconductors. *Metall. Mater. Trans. A*, **29A**, 1525–1526.
84. Wagner, R. and Kampmann, R. (1991) Homogeneous second phase precipitation, in *Materials Science and Technology*, Phase Transformations in Materials, vol. **5** (ed P. Haasen), Wiley-VCH Verlag GmbH, Weinheim, pp. 213–303.
85. Binder, K. (1991) in *Spinodal Decomposition in Materials Science and Technology*, Phase Transformations in Materials, vol. **5** (ed P. Haasen), Wiley-VCH Verlag GmbH, Weinheim, pp. 405–471.
86. Lubarda, V.A. (2003) On the effective lattice parameter of binary alloys. *Mech. Mater.*, **35**, 53–68.
87. Jeffs, N.J., Blant, A.V. and Cheng, T.S. (1998) EXAFS studies of group III nitrides. *MRS Proc.*, **512**, 519–524.
88. Miyano, K.E., Woicik, J.C., Robins, L.H. *et al.* (1997) Extended X rays absorption fine structure study of Al_xGa_{1-x} N films. *Appl. Phys. Lett.*, **70**, 2108–2110.
89. Jacob, T., Raj, S. and Rannesh, L. (2007) Vegard's Law: a fundamental law or an approximation? *Int. J. Mater. Res.*, **9**, 776–779.
90. Okamoto, H., Chakrabarti, D.J., Laughlin, D.E. and Massalki, T.B. (1987) The Au-Cu (gold-copper) system. *Bull. Alloy Phase Diagrams*, **8**, 454–473.
91. Bessiere, M., Lefebvre, M. and Calvayrac, Y. (1983) X ray diffraction study of short range order in a disordered Au_3Cu alloy. *Acta Crystallogr.*, **39B**, 145–153.
92. Okamoto, H. and Massalki, T.B. (1983) The Ag-Au (silver-gold) system. *J. Phase Equilib.*, **4**, 30–38.
93. Jian-Jun, G., Ji-Xian, Y. and Dong, D. (2007) First principle calculation on Au-Ag clusters. *Commun. Theor. Phys. (Bejing)*, **48**, 348–352.
94. Morse, M.D. (1986) Clusters of transition metal atoms. *Chem. Rev.*, **86**, 1049–1109.
95. Kobayashi, K., Kurita, N., Kumahora, H. and Tago, K. (1991) Bond energy calculations of Ag_2, Au_2 and CuAg with the general gradient approximation. *Phys. Rev. A*, **43**, 5810–5813.
96. Flanagan, W.F. and Averbach, B.L. (1956) Hall effect in solid solutions. *Phys. Rev.*, **10**, 11441–11442.
97. Weinberger, P., Drchal, V., Szunyogh, L. *et al.* (1994) Electronic and structural properties of copper-gold alloys. *Phys. Rev. B*, **49**, 13366–13372.
98. Szoldos, L. (1965) The determination of bond energies in the alloy system Au-Cu. *Phys. Status Solidi A*, **11**, 667–671.
99. Glazov, V.M. and Shchelikov, O.D. (2000) Volume changes during melting and heating of silicon and germanium melts. *High Temp.*, **38**, 405–412.
100. Kaczmarski, M., Bedoya-Martinez, O.N. and Hernadez, E.R. (2005) Phase diagrams of silicon by atomistic simulations. *Phys. Rev. Lett.*, **94**, 095701-1–095701-4.
101. Bernasconi, M., Chiarotti, G.L., Focher, P. *et al.* (1995) First-principle constant pressure molecular dynamics. *J. Phys. Chem. Solids*, **56**, 501–505.
102. Yang, C.C., Li, J.C. and Jiang, Q. (2004) Temperature–pressure phase diagram of silicon determined by Clapeyron equation. *Solid State Commun.*, **129**, 437–441.
103. Yang, C.C. and Yang, Q. (2004) Temperature–pressure phase diagram of germanium determined by Clapeyron equation. *Scr. Mater.*, **51**, 1081–1085.

104. *Properties of Silicon*, EMIS Data Review Series, vol. **4**, INSPEC, London (1988).
105. Hu, Z., Merkle, L.D., Manoni, C.S. and Spain, I.L. (1986) Crystal data for high-pressure phases of silicon. *Phys. Rev. B*, **34**, 4679–4684.
106. Piltz, R.O., Maclean, J.R., Clark, S.J. *et al.* (1995) Structure and properties of silicon XII: a complex tetrahedrally bonded phase. *Phys. Rev. B*, **52**, 4072–4084, and reference therein.
107. Bundy, F.P. (1964) Phase diagrams of silicon and germanium to 200 kbar, 1000°C. *J. Chem. Phys.*, **41**, 3809–3814.
108. Car, R. and Parrinello, M. (1985) Unified approach for molecular dynamics and density functional Theory. *Phys. Rev. Lett.*, **55**, 2471–2474.
109. Behler, J., Martonak, R., Donadio, D. and Parrinello, M. (2008) Pressure-induced phase transformations in silicon studied by neural network – based metadynamic simulations. *Phys. Status Solidi B*, **12**, 2618–2629.
110. Štich, I., Car, R. and Parrinello, M. (1991) Structural, bonding, dynamical and electronic properties of liquid silicon: an *ab initio* molecular-dynamics study. *Phys. Rev. B*, **44**, 4262–4274.
111. Waseda, W. and Suzuki, K. (1975) Structure of molten silicon and germanium by X-Ray diffraction. *Z. Phys. B*, **20**, 339–343.
112. Sato, Y., Nishizuka, T., Hara, K. *et al.* (2000) Density measurements of molten silicon by a pycnometric method. *Int. J. Thermophys.*, **21**, 1463–1471.
113. Stich, I., Car, R. and Parrinello, M. (1989) Bonding and disorder in liquid silicon. *Phys. Rev. Lett.*, **63**, 2240–2243.
114. Chelikowsky, J.R., Derby, J., Godlevsky, V. *et al.* (2001) *Ab initio* simulations of liquid semiconductors using the pseudopotential–density functional method. *J. Phys. Condens. Matter*, **13**, R817–R854.
115. Okada, J.T., Sit, P.H.-L., Watanabe, Y. *et al.* (2012) Persistence of covalent bonding in liquid silicon probed by inelastic x-ray scattering. *Phys. Rev. Lett.*, **108**, 067402.
116. Kulkarni, R.V., Aulbur, W.G. and Stroud, D. (1997) Ab initio molecular-dynamics study of the structural and transport properties of liquid germanium. *Phys. Rev. B*, **55**, 6896–6904.
117. Koga, T., Okumura, H., Nishio, K. *et al.* (2002) Simulation study of liquid germanium under pressure. *J. Non-Cryst. Solids*, **312–314**, 95–98.
118. Chaoui, N., Siegel, J., Wiggins, S.M. and Solis, J. (2005) Pressure-induced transient structural change of liquid germanium induced by high-energy picosecond laser pulses. *Appl. Phys. Lett.*, **86**, 221901–221903.
119. Olesinski, R.W. and Abbashian, G.I. (1984) The Ge-Si system. *Bull. Alloys Phase Diagrams*, **5**, 180–183.
120. Lee, S.M., Kim, E., Lee, Y.H. and Kim, N. (1998) Ge(Si) ordering on double layer stepped Si(Ge) (001) surface. *J. Korean Phys. Soc.*, **33**, 684–688.
121. Jivani, A.R., Trivedi, H.J., Gajjar, P.N. and Jani, A.R. (2005) Some physical properties of $S_{i1\text{-}x}Ge_x$ solid solutions using a pseudo alloy atom model. *Semicond. Phys. Quantum Electron. Optoelectron.*, **8**, 14–17.
122. Soma, T. (1979) The electronic theory of Si-Ge solid solution. *Phys. Status Solidi B*, **95**, 427–431.
123. Dunweg, B. and Landau, D.P. (1993) Phase diagram and critical behavior of the Si-Ge unmixing transition. *Phys. Rev. B*, **48**, 14182–14197.

124. Kajiyama, H., Muramatsu, S., Shimada, T. and Nishino, Y. (1992) Bond length relaxation in crystalline $Si_{1-x}Ge_x$ alloys: an extended X-ray absorption fine study. *Phys. Rev. B*, **45**, 14005–14010.
125. Shen, S., Zhang, D. and Fan, X. (1995) Tight-binding studies of crystalline $Si_{1-x}Ge_x$ alloys. *J. Phys. Condens. Matter*, **7**, 3529–3538.
126. Claeys, C. and Simoen, E. (2007) *Germanium Based Technologies: From Materials to Devices*, Elsevier.
127. Shao, L., Zhang, J., Chen, J. *et al.* (2004) Enhancement of boron solid solubility in Si by point-defect engineering. *Appl. Phys. Lett.*, **84**, 3325–3327.
128. Okamoto, H. (2005) B-Si (Boron-Silicon). *J. Phase Equilib. Diffus.*, **26**, 396.
129. Tang, K., Ovrelid, E. J., Tranell, G., Tangstad, M. (2009) *Thermochemical and Kinetic Databases for the Solar Cell Silicon Materials in Crystal Growth of Si for Solar Cells*, K. Nakajima, N. Usami Ed. Springer pp. 219–250 .
130. Scace, R.I. and Slack, G.A. (1959) Solubility of carbon in silicon and germanium. *J. Chem. Phys.*, **30**, 1551–1555.
131. Hu, B., Du, Y., Xu, H. *et al.* (2010) Thermodynamic description of the C-Ge and C-Mg systems. *J. Min. Metall. Sect. B*, **46**, 97–103.
132. Olesinski, R.W. and Abbaschian, G.J. (1984) The C-Si system. *Bull. Alloy Phase Diagrams*, **5**, 486–489.
133. Brazier, C.R. and Ruiz, J.I. (2011) The first spectroscopic observation of germanium carbide. *J. Mol. Spectrosc.*, **270**, 26–32.
134. Mahmood, A. and Sansores, L.E. (2005) Band structure and bulk modulus calculations of germanium carbide. *J. Mater. Res.*, **20**, 1101–1106.
135. Chroneos, A. (2008) Stability of impurity–vacancy pairs in germanium carbide. *J. Mater. Sci: Mater. Electron.*, **19**, 25–28.
136. Trumbmore, F.A., Porbanski, E.M. and Tartaglia, A.A. (1959) Solid soubilities of Aluminum and Gallium in germanium. *Phys. Chem.*, **11**, 239–245.
137. Yoshikawa, T. and Morita, K. (2003) Solid solubilities and thermodynamic properties of aluminum in solid silicon. *J. Electrochem. Soc.*, **150**, G465–G468.
138. Degtyareva, V.F., Chipenko, G.V., Belash, I.T. *et al.* (1985) F.C.C. solid solutions in Al-Ge and Al-Si Alloys under high pressure. *Phys. Status Solidi A*, **89**, 127–128.
139. Kagaya, H.-M., Imazawa, K., Sato, M. and Soma, T. (1998) Phase diagrams of Al–Si and Al–Ge systems. *Phys. B: Condens. Matter*, **245**, 252–255.
140. Ceccaroli, B. and Pizzini, S. (2012) Processes, in *Advanced Silicon Materials for Photovoltaic Applications* (ed S. Pizzini), John Wiley & Sons, Ltd, Chichester, pp. 21–78.
141. Rodot, M., Bourèe, J.E., Mesli, A. *et al.* (1987) Al-related recombination center in polycrystalline Si. *J. Appl. Phys.*, **62**, 2556–2558.
142. Marchand, R.L. and Shah, C.T. (1977) Study of thermally induced deep levels in Al doped Si. *J. Appl. Phys.*, **48**, 336–341.
143. Yoshikawa, T. and Morita, K. (2005) Refining of Si by the solidification of Si–Al melt with electromagnetic force. *ISIJ Int.*, **45**, 967–971.
144. Kotval, P.S. and Strock, H.B. (1980) *Process for producing of refined MG silicon*. US Patent 4,195,067, March 25, 1980.
145. He, G. and Atwater, H.A. (1997) Intraband transitions in $Sn_xGe_{1-.x}$ alloys. *Phys. Rev. Lett.*, **79**, 1937–1940.

146. Costa, R.D., Cook, C.S., Birdwell, A.G., Littler, C.L., Canonico, M., Zollner, S., Kouvetakis, J., Menendez, J. (2006) Optical critical points of thin-film $\mathrm{Ge}_{1-\mathrm{y}}\mathrm{Sn}_{\mathrm{y}}$ alloys: a comparative $\mathrm{Ge}_{1-y}\mathrm{Sn}_y/\mathrm{Ge}_{1-x}\mathrm{Si}_x$ study. *Phys. Rev. B*, **73**, 125207
147. Moontragoon, P., Ikonic, Z. and Harrison, P. (2007) Band structure calculations of Si–Ge–Sn alloys: achieving direct band gap materials. *Semicond. Sci. Technol.*, **22**, 742–748.
148. Mathews, J., Beeler, R.T., Tolle, J. *et al.* (2010) Direct-gap photoluminescence with tunable emission wavelength in $\mathrm{Ge}_{1-y}\mathrm{Sn}_y$ alloys on silicon. *Appl. Phys. Lett.*, **97**, 221912.
149. Lindl, J.D. (1995) Development of the indirect-drive approach to inertial confinement fusion and the target physics basis for ignition and gain. *Phys. Plasmas*, **2**, 3933–4024.
150. Bundy, F.P. (1963) Melting of graphite at very high pressure. *J. Chem. Phys.*, **38**, 618–631.
151. Bundy, F.P. (1963) Direct conversion of graphite to diamond in static pressure apparatus. *J. Chem. Phys.*, **38**, 631–643.
152. Bundy, F.F.P. (1989) Pressure-temperature diagram of elemental carbon. *Physica A*, **156**, 169–178.
153. Bundy, F.P., Bassett, W.A., Weathers, M.S. *et al.* (1996) The pressure-temperature phase and transformation diagram for carbon; updated through 1994. *Carbon*, **34**, 141–153.
154. Togaya, M. (1997) Pressure dependences of the melting temperature of graphite and the electrical resistivity of liquid carbon. *Phys. Rev. Lett.*, **79**, 2474.
155. Savvatimski, A.I. (2003) Melting point of graphite and liquid carbon. *Phys. Usp.*, **46**, 1295–1303.
156. Galli, G., Martin, R.M., Car, R. and Parrinello, M. (1990) Ab initio calculation of properties of carbon in amorphous and liquid state. *Science*, **250**, 1547.
157. Davydov, V.A., Rakhmanina, A.V., Rols, S. *et al.* (2007) Size-dependent phase transition of diamond to graphite at high pressures. *J. Phys. Chem. C*, **111**, 12918–12925.
158. Khaliullin, R.Z., Eshet, H., Kühne, T.D. *et al.* (2011) Nucleation mechanism for the direct graphite-to-diamond phase transition. *Nat. Mater.*, **10**, 693–697.
159. Wang, X., Scandolo, S. and Car, R. (2005) Carbon phase diagram from *Ab initio* molecular dynamics. *Phys. Rev. Lett.*, **95**, 185701–185704.
160. Bundy, F.P., Bovenwerk, H.P., Strong, H.M. and Wentorf, J.R.H. (1961) Diamond-graphite equilibrium line from growth and graphitization of diamond. *J. Chem. Phys.*, **35**, 383–391.
161. Ghiringhelli, L., Los, J.H., Mejier, E.J. *et al.* (2005) Modeling the phase diagram of carbon. *Phys. Rev. Lett.*, **94**, 145701–145704.
162. Grumbach, M.P. and Martin, R.M. (1996) Phase diagram of carbon at high pressures and temperatures. *Phys. Rev. B*, **54**, 15730–15741.
163. Dmitriev, V.P., Rochal, S.B., Gufan, Y.M. and Toledano, P. (1989) Reconstructive transitions between ordered phases: the martensitic fcc-hcp and the graphite-diamond transitions. *Phys. Rev. Lett.*, **62**, 2495–2498.
164. Correa, A.A., Bonev, S.A. and Galli, G. (2006) Carbon under extreme conditions: phase boundaries and electronic properties from first-principle calculations. *Proc. Natl. Acad. Sci. U.S.A.*, **103**, 1204–1208.

165. Steinbeck, J., Dresselhaus, G. and Dresselhaus, M.S. (1990) The properties of liquid carbon. *Int. J. Thermophys.*, **11**, 789–796.
166. Steinbeck, J., Braunstein, G., Dresselhaus, M.S. *et al.* (1985) A model for pulsed laser melting of graphite. *J. Appl. Phys.*, **58**, 4374–4381.
167. Malvezzi, A.M., Bloembergen, N. and Huang, C.Y. (1986) Time-resolved picosecond optical measurements of laser-excited graphite. *Phys. Rev. Lett.*, **57**, 146.
168. Savvatimskiy, A.I. (2008) Liquid carbon density and resistivity. *J. Phys. Condens. Matter*, **20**, 114112–114117.
169. Rao, K.J. and Mohan, R. (1981) Chemical Bond approach to determining conductivity band gaps in amorphous chalcogenides and pnictides. *Solid State Commun.*, **39**, 1065–1068.
170. Choyke, W.J., Mastromami, H. and Pensl, G. (1997) *Silicon Carbide: A Review of Fundamental Questions and Applications to Current Device Technology*, John Wiley & Sons, Ltd, Chichester.
171. Choyke, W.J., Matsunami, H. and Pensl, G. (2004) *Silicon Carbide: Recent Major Advances*, Springer-Verlag, Berlin.
172. Friedrichs, P., Kimoto, T., Ley, L. and Pensl, G. (2009) *Silicon Carbide: Growth, Defects, and Novel Applications*, vol. **1**, John Wiley & Sons, Inc., New York.
173. Friedrichs, P., Kimoto, T., Ley, L. and Pensl, G. (2009) *Silicon Carbide, Power Devices and Sensors*, vol. **2**, John Wiley & Sons, Inc., New York.
174. Sakwe, S.A., Stockmeier, M., Hens, P. *et al.* (2009) Bulk growth of SiC – Review on advances of SiC vapor growth for improved doping and systematic study on dislocation evolution, in *Silicon Carbide: Growth, Defects, and Novel Applications*, vol. 1 (eds P. Friedrichs, T. Kimoto, L. Ley and G. Pensl), John Wiley & Sons, Inc., pp. 1–31.
175. Madar, R. (2004) Materials science: silicon carbide in contention. *Nature*, **430**, 974–975.
176. Fissel, A. (2001) Relationship between growth conditions, thermodynamic properties and crystal structure of SiC. *Int. J. Inorg. Mater.*, **3**, 1273–1275.
177. Sambasivan, S., Capobianco, C. and Petuskey, W.T. (1993) Measurement of the free energy of formation of silicon carbide using liquid gold as a silicon potentiometer. *J. Am. Ceram. Soc.*, **76**, 397–400.
178. Pattanaik, A.K., Robi, P.S. and Srinivasan, A. (2003) Microhardness of Pb-modified calchogenide glasses. *J. Optoelectron. Adv. Mater.*, **5**, 35–38.
179. Sanderson, R.T. (1976) *Chemical Bonds and Bond Energy*, 2nd edn, Academic Press, London.
180. Singh, K., Saxena, N.S., Srivastava, O.N. *et al.* (2006) Energy gap of selenium chalcogenide glasses. *Chalcogenide Lett.*, **3**, 33–36.
181. Silva, L.A. and Cutler, M. (1990) Optical properties of liquid Se-Te alloys. *Phys. Rev. B*, **42**, 7103–7113.
182. Kumar, A., Barman, P.B. and Sharma, R. (2010) Study of the physical properties with compositional dependence of Bi content in Bi-Se-Te glasses. *Adv. Appl. Sci. Res.*, **1**, 47–57.
183. Grison, E. (1951) Studies on tellurium-selenium alloys. *J. Chem. Phys.*, **19**, 1109–1113.

184. Fthenakis, V. and Alsema, E. (2006) Photovoltaics energy payback times, greenhouse gas emissions and external costs: 2004– early 2005 status. *Prog. Photovoltaics Res. Appl.*, **14**, 275–280.
185. Raugei, M., Bargigli, S. and Ulgiati, S. (2007) Life cycle assessment and energy pay-back time of advanced photovoltaic modules: CdTe and CIS compared to poly-Si. *Energy*, **32**, 1310–1318.
186. Guskov, N., Greenberg, J.H., Fiederle, M. and Benz, K.-W. (2004) Vapour pressure investigation of CdZnTe. *J. Alloys Compd.*, **371**, 118–121.
187. Cavallini, A. and Fraboni, B. (2013) Point defects in cadmium zinc telluride. *J. Cryst. Growth*, **379**, 41–54.
188. Capper, P. (1994) *Properties of Narrow Gap Cadmium Based Compounds*, EMIS Review Series, vol. **10**, INSPEC.
189. Franc, J., Grill, R., Hl'ıdek, P. *et al.* (2001) The influence of growth conditions on the quality of CdZnTe single crystals. *Semicond. Sci. Technol.*, **16**, 514–520.
190. Szeles, C. and Driver, M.C. (1998) Growth and properties of semi-insulating CdZnTe for radiation detector applications. *Proc. SPIE*, **3446**, 1–8.
191. Greenberg, J.H., Guskov, V.N., Lazarev, V.B. and Shebershneva, O.V. (1992) Vapor pressure scanning of nonstoichiometry in CdTe. *J. Solid State Chem.*, **102**, 382–389.
192. Greenberg, J.H. (1996) $P - T - X$ phase equilibrium and vapor pressure scanning of non-stoichiometry in CdTe. *J. Cryst. Growth*, **161**, 1–4.
193. Feltgen, T., Greenberg, J.H., Guskov, V.N. *et al.* (2001) P–T–X phase equilibrium studies in Zn–Te for crystal growth by the Markov method. *Int. J. Inorg. Mater.*, **3**, 1241–1249.
194. Guskov, V.N., Greenberg, J.H., Alikhanyan, A.S. *et al.* (2002) P–T–X phase equilibrium in the Zn–Te System V.N. *Phys. Status. Solidi B*, **229**, 137–140.
195. Weltner, W. (1969) On polytypism and internal rotation. *J. Chem. Phys.*, **51**, 2469–2484.
196. McMahon, M.I., Nelmes, R.J., Wright, N.G. and Allan, D.R. (1994) Crystal structure studies of II-VI semiconductors using angle dispersive diffraction techniques with an image plate detector. *AIP. Conf. Proc.*, **309**, 633. doi: 10.1063/1.46413.
197. Laugier, A. (1973) Thermodynamics and phase diagram calculation in II-VI and IV-VI ternary systems using an associated solution model. *Rev. Phys. Appl.*, **8**, 259–270.
198. Moskvin, P., Olchowik, G., Olchowik, J.M. *et al.* (2011) New approach to the determination of phase equilibrium in the ZnTe system. *Task Q.*, **15**, 209–217, http://www.bop.com.pl (accessed 20 December 2014).
199. Brebrick, R.F. (2010) The Cd–Te phase diagram. *Calphad*, **34**, 434–440.
200. Adachi, S. (2009) *Properties of Semiconductor Alloys: Group IV, III-V and II-VI Semiconductors*, John Wiley & Sons, Ltd, Chichester.
201. Rudolph, P. (2003) Non-stoichiometry related defects at the melt growth of semiconductor compound crystals: a review. *Cryst. Res. Technol.*, **38**, 542–554, and references therein.
202. Sharma, R.C. and Chang, Y.A. (1989) The Cd-Te system. *J. Phase Equilib.*, **10**, 334.
203. J. Greenberg, *Thermodynamic Basis of Crystal Growth* Springer (2002), ISBN: 3642074529, ISBN: 13: 9783642074523.

204. Sharma, R.C. and Chang, Y.A. (1966) The Cd-Se system. *J. Phase Equilib.*, **17**, 140–145.
205. Sharma, R.C. and Chang, Y.A. (1987) The Te-Zn system. *J. Phase Equilib.*, **85**, 417.
206. Moskvin, P., Olchowik, G., Olchowik, J.M. *et al.* (2011) New approach to the determination of phase equilibrium in the ZnTe system. *Task Q.*, **15**, 209–217.
207. Gavrichev, K.S., Sharpataya, G.A., Guskov, V.N. *et al.* (2002) High-temperature heat capacity and thermodynamic functions of zinc telluride. *Thermochim. Acta*, **381**, 133–138.
208. Gavrichev, K.S., Sharpataya, G.A., Guskov, V.N. *et al.* (2002) Thermodynamic properties of ZnTe in the temperature range 15–925 K. *Phys. Status Solidi*, **229**, 133–135.
209. Stukes, A.D. and Farrel, G. (1964) Electrical and thermal properties of alloys of CdTe and CdSe. *J. Phys. Chem. Solids*, **25**, 477–482.
210. Zabdyr, L.A. (1984) Thermodynamics and phase diagram of the pseudobinary ZnTe-CdTe system. *J. Electrochem. Soc.*, **131**, 2157–2160.
211. Haloui, A., Feutelais, Y. and Legendre, B. (1997) Experimental study of the ternary system Cd-Te-Zn. *J. Alloys Compd.*, **260**, 179–192.
212. Alikhanian, A.S., Guskov, V.N., Natarovsky, A.M. *et al.* (2002) Mass spectrometric study of the CdTe–ZnTe system. *J. Cryst. Growth*, **240**, 73–79.
213. Patrick, S., Chen, A.B., Sher, A. and Berding, M.A. (1988) Phase diagrams and microscopic structures of (Hg,Cd)Te, (Hg,Zn)Te and (Cd,Zn)Te alloys. *J. Vac. Sci. Technol., A*, **6**, 2643–2649.
214. Williams, D.J. (1994) Densities and lattice parameters of CdTe,CdZnTe and CdTeSe, in *Properties of Narrow Gap Cd Based Compounds*, Emis Data Review Series, vol. **10** (ed P. Capper), INSPEC, p. 399.
215. Ohata, K., Saraie, J. and Tanaka, T. (1973) Phase diagram of the CdS-CdTe pseudobinary system. *Jpn. J. Appl. Phys.*, **12**, 1198–1204.
216. Lane, D.W., Conibeer, G.J., Wood, D.A. *et al.* (1999) Sulphur diffusion in CdTe and the phase diagram of the CdS–CdTe pseudo-binary alloy. *J. Cryst. Growth*, **197**, 743–748.
217. Tmar, M., Gabriel, A., Chatillon, C. and Ansara, I. (1984) Critical analysis of the thermodynamic properties and phase diagrams in the III-V compounds: the InP-In and Ga-P systems. *J. Cryst. Growth*, **68**, 557–580.
218. Mizuno, O. (1975) Vapor growth of InP. *Jpn. J. Appl. Phys.*, **14**, 451–457.
219. Haitz, R. and Tsao, J.T. (2011) Solid-state lighting: "The Case" 10 years after and future prospects. *Phys. Status Solidi A*, **208**, 17–29.
220. Nakamura, S., Senoh, M., Nagahama, S.-I. *et al.* (1996) InGaN-based multi-quantum-well-structure laser diodes. *Jpn. J. Appl. Phys.*, **35**, L74–L76.
221. Kuykendall, T., Ulrich, P., Alon, S. and Yang, P. (2007) Complete composition tunability of InGaN nanowires using a combinatorial approach. *Nat. Mater.*, **6**, 951–956.
222. Li, C., Li, J. and Zhang, W. (2000) A thermodynamic assessment of the GaInP system. *J. Phase Equilib.*, **21**, 357–363.
223. Marzari, N., de Gironcoli, S. and Baroni, S. (1994) Structure and phase stability of Ga_x $In_{1-x}P$ solid solutions from computational Alchemy. *Phys. Rev. Lett.*, **72**, 4001–4004.
224. Stringfellow, G.B. (1974) Calculation of ternary and quaternary III-V phase diagrams. *J. Cryst. Growth*, **27**, 21–34.

225. Jenichen, A. and Engler, C. (2010) Stability and band gaps of InGaP, BGaP, BInGaP alloys: density functional supercell calculations. *Phys. Status Solidi B*, **247**, 59–66.
226. Ansara, I., Chatillon, C., Lukas, H.L. *et al.* (1994) A binary data base for III-V compound semiconductor systems. *Calphad*, **18**, 177–222.
227. Scofield, D., Davison, J.E., Smith, S.R. (1991) Calculation of Phase Diagrams for Metal-GaAs System. Interim Report for period January 1990 January 1991, project WL-TR-91-2097.
228. Charykov, N.A., Litvak, A.M., Mikhailova, M.P. *et al.* (1997) Solid solution $In_xGa_{1-x}As_ySb_zP_{1-y-z}$: a new material for infrared optoelectronics. I. Thermodynamic analysis of the conditions for obtaining solid solutions, isoperiodic to InAs and GaSb substrates, by liquid-phase epitaxy. *Semiconductors*, **31**, 344–349.
229. Quiao, H., Shen, J., Xi, G. and Chatillon, C. (1994) Calculation of phase diagram for pseudobinary GaAs-InAs. *Trans. Nonferrous Met. Soc.*, **4**, 25–28.
230. Ohtani, H., Kobayashi, K. and Ishida, K. (2001) Thermodynamic study of phase equilibria in strained III-V alloy semiconductors. *J. Phase Equilib.*, **22**, 276–286.
231. Dinsdale, A.T. (1991) SGTE data for pure elements. *Calphad*, **15**, 317–425.
232. Okada, T., Weatherly, G.C. and McComb, D.W. (1997) Growth of strained InGaAs layers on InP substrates. *J. Appl. Phys.*, **81**, 2185–2196.
233. Behbehani, M.K., Piner, E.L., Liu, S.X. *et al.* (1999) Phase separation and ordering coexisting in $In_xGa_{1-x}N$ grown by metal organic chemical vapor deposition. *Appl. Phys. Lett.*, **75**, 2202–2204.
234. Ruterana, P., Nouet, G., der Stricht, W.V. *et al.* (1998) Chemical ordering in wurtzite $In_xGa_{1-x}N$ layers grown on (0001) sapphire by metalorganic vapor phase epitaxy. *Appl. Phys. Lett.*, **72**, 1742–1745.
235. Yamaguchi, S., Kariya, M., Nitta, S. *et al.* (1998) Structural and optical properties of AlInN and AlGaInN on GaN grown by metalorganic vapor phase epitaxy. *J. Cryst. Growth*, **195**, 309–313.
236. Teles, L.K., Marques, M., Scolfaro, L.M.R. *et al.* (2002) Phase separation suppression in InGaN epitaxial layers due to biaxial strain. *Appl. Phys. Lett.*, **80**, 769–771.
237. Silveira, E., Tabata, A., Leite, J.R. *et al.* (1999) Evidence of phase separation in cubic $In_xGa_{1-x}N$ epitaxial layers by resonant Raman scattering. *Appl. Phys. Lett.*, **75**, 3602–3604.
238. Teles, L.K., Scolfaro, L.M., Leite, J.R. *et al.* (2002) Phase diagram, chemical bond and gap bowing in cubic $In_xAl_{1-x}N$ alloys: ab initio calculations. *J. Appl. Phys.*, **92**, 7109–7113.
239. Teles, L.K., Marques, M., Scolfaro, L.M.R. *et al.* (2004) Phase separation and ordering in group-III nitride alloys. *Braz. J. Phys.*, **34**, 593–597.
240. Gan, C.K., Feng, Y.P. and Srolovitz, D.J. (2006) First principle calculations of the thermodynamics of In_xGa_{1-x} N alloys: effect of lattice vibrations. *Phys. Rev. B*, **73**, 235214.
241. Zhong Zhang, J. (2009) *Optical Properties and Spectroscopy of Nanomaterials*, World Scientific, Hackensack, NJ, pp. 127–133.
242. Wise, F.W. (2000) Lead salt quantum dots: the limit of strong quantum confinement. *Acc. Chem. Res.*, **33**, 773–780.

243. Stucky, G.D. and McDougall, J.E. (1990) Quantum confinement and host/guest chemistry: probing a new dimension. *Science New Ser.*, **247**, 669–678.
244. Zhang, L.Z., Sun, W. and Chen, P. (2003) Spectroscopic and theoretical studies of quantum and electronic confinement effects in nanostructured materials. *Molecules*, **8**, 207–222.
245. Schmidt, V., Wittemann, J.V. and Gösele, U. (2010) Growth, thermodynamics, and electrical properties of silicon nanowires. *Chem. Rev.*, **110**, 361–388.
246. Sun, J. and Simon, S.L. (2007) The melting behavior of aluminum nanoparticles. *Thermochim. Acta*, **463**, 32–40.
247. Zhao, M., Zhou, X.-H. and Jiang, Q. (2001) Comparing of different models for melting point changes of metallic nanocrystals. *J. Mater. Res.*, **16**, 3304–3308.
248. Jiang, Q., Li, J.C. and Chi, B.Q. (2002) Size-dependent cohesive energy of nanocrystals. *Chem. Phys. Lett.*, **366**, 551–554.
249. Liang, L.H., Liu, D. and Jang, Q. (2003) Size-dependent continuous binary solution phase diagram. *Nanotechnology*, **14**, 438–442.
250. Sun, C.Q., Tay, B.K., Lau, S.P. *et al.* (2001) Bond contraction and lone pair interaction at nitride surfaces. *J. Appl. Phys.*, **90**, 2615–2617.
251. Sheu, H.-S., Jeng, U.-S., Shih, W.-J. *et al.* (2008) Phase separation inside the CdTe-CdSe type II quantum dots revealed by synchrotron x-ray diffraction and scattering. *J. Phys. Chem. C*, **112**, 9617–9622.
252. Davydov, V.A., Rakhnìmanina, A.V., Rols, S. *et al.* (2007) Size dependent phase transition of diamond to graphite at high pressures. *J. Phys. Chem. C*, **111**, 12918–12925.
253. Tolbert, S., Herhold, A.B., Brus, L.E. and Alivisatos, A.P. (1996) Pressure-induced structural transformations in Si nanocrystals: surface and shape effects. *Phys. Rev. Lett.*, **76**, 4384–4387.
254. van Gool, W. (ed) (1973) *Fast Ion Transport in Solids*, North-Holland/American Elsevier.
255. Bruce, P. (ed) (1997) *Solid State Electrochemistry*, Cambridge University Press.
256. Maier, J. (2009) Fundamentals, applications, and perspectives of solid-state electrochemistry: a synopsis, in *Solid State Electrochemistry I* (ed V.V. Kharton), Wiley-VCH Verlag GmbH, Weinheim, pp. 1–13.
257. Mari, C.M., Pizzini, S., Manes, L. and Toci, F. (1977) A novel approach to the oxygen microdetermination of oxides by EMF measurements. *J. Electrochem. Soc.*, **124**, 1831–1835.
258. Aronson, S., Salzano, F.J. and Bellafiore, D. (1968) Thermodynamic properties of the potassium–graphite lamellar compounds from solid-state emf measurements. *J. Chem. Phys.*, **49**, 434.
259. Kobayashi, Y., Egawa, T., Tamura, S. *et al.* (1997) Trivalent Al^{3+} ion conduction in aluminum tungstate. *Solid Chem. Mater.*, **9**, 1649–1654, 1649.
260. Pizzini, S. and Morlotti, R. (1972) E.M.F. measurements with solid electrolyte galvanic cells on the calcium oxide + zirconia system: determination of the phase relationships. *J. Chem. Soc., Faraday Trans.*, **68**, 1601–1610.
261. Katayama, I., Tanaka, T. and Iida, T. (2003) Thermodynamic study of semiconducting related materials by use of EMF method with solid electrolyte. *J. Min. Metall.*, **39**, 453–464.

262. Leushina, A.P., Makhanova, E.V. and Zlomanov, V.P. (2010) Influence of the nature and density of defects on the thermodynamic and electrical properties of semiconductor materials. *Inorg. Mater.*, **46**, 269–275.
263. Babanly, M.B., Gasanov, Z.T., Mashadiev, L.F. *et al.* (2012) Thermodynamic study of the Cu–As–S system by EMF measurements with $Cu_4RbCl_3I_2$ as a solid electrolyte. *Inorg. Mater.*, **48**, 225–228.
264. Müller, G., Mühe, A., Backofen, R. *et al.* (1999) Study of oxygen transport in Czochralski growth of silicon. *Microelectron. Eng.*, **1**, 13–147.
265. *Phase Transformations in Metals and Alloys*, by D. A. Porter, K. E. Easterling and M. Y. Sherif, CRC Press, 3rd edn (2009) p. 309.